

UC Berkeley

UC Berkeley Electronic Theses and Dissertations

Title

Low Energy Helium Ion Implantation and Application of a High Energy Ion Implantation Tool to Comprehensively Investigate the High Helium Dose Effects

Permalink

<https://escholarship.org/uc/item/1bc7j96h>

Author

Stevenson, Sarah Rachelle

Publication Date

2022

Peer reviewed|Thesis/dissertation

Low Energy Helium Ion Implantation and Application of a High Energy Ion Implantation
Tool to Comprehensively Investigate High Helium Dose Effects

by

Sarah Rachelle Stevenson

A dissertation submitted in partial satisfaction of the

requirements for the degree of

Doctor of Philosophy

in

Engineering - Nuclear Engineering

in the

Graduate Division

of the

University of California, Berkeley

Committee in charge:

Professor Peter Hosemann, Chair

Professor Lee Bernstein

Professor Mary Scott

Fall 2022

Low Energy Helium Ion Implantation and Application of a High Energy Ion Implantation
Tool to Comprehensively Investigate High Helium Dose Effects

Copyright 2022
by
Sarah Rachelle Stevenson

Abstract

Low Energy Helium Ion Implantation and Application of a High Energy Ion Implantation Tool to Comprehensively Investigate High Helium Dose Effects

by

Sarah Rachelle Stevenson

Doctor of Philosophy in Engineering - Nuclear Engineering

University of California, Berkeley

Professor Peter Hosemann, Chair

Ion beam implantations are widely performed to understand the effects of radiation damage such as He bubbles on nuclear structural materials. This work investigates near-surface changes caused by low energy ion implantations, as well as deep ion implantations leading to bulk-property changes.

The near-surface interactions of low energy (25-60 keV) He ions with Ti and Cu targets were investigated by atomic force microscopy (AFM), nanoindentation, Transmission Electron Microscopy (TEM), and Positron Annihilation Spectroscopy (PAS). AFM showed a linear increase in swelling with respect to dose for all materials, and blistering onset doses of 5×10^{17} ions/cm², 8×10^{17} ions/cm², and 1×10^{18} ions/cm² for Ti(0001), Ti(10 $\bar{1}$ 0), and Cu(100), respectively. Cavities on the order of 287 nm diameter were observed in Cu, and surface blisters formed from the intersection of these large cavities. He bubbles observed in Ti were around 1 nm diameter, and surface blisters formed from inter-bubble fracture. PAS showed an increase in defect concentration with respect to depth and dose, agreeing well with AFM and TEM results. An additional PAS measurement determined that shock loading can lead to a decrease in vacancy concentration in a pre-implanted material.

To fill the gap between widely available low energy ion implantations and difficult-to-achieve bulk implantations, this work aimed to establish the use of the 88-Inch Cyclotron for nuclear materials studies. Four HT-9 SS-J-geometry tensile specimens were irradiated with high energy (19-25 MeV) deuterons at the 88-Inch Cyclotron to doses of approximately 0.2 dpa prior to small scale tensile testing. The results from this study showed irradiation hardening characterized by black dot irradiation defects, and the tensile test results were in agreement with the available data. To support future deep ion implantation campaigns, a novel ion beam degrader capable of uniformly implanting bulk-scale materials with He ions was designed.

In loving memory of Sadie Ann Stevenson and Donna Marie Bridgman.

Contents

Contents	ii
List of Figures	iv
List of Tables	xv
1 Introduction	1
2 Review of Helium Effects on Nuclear Materials	4
2.1 Radiation Damage	4
2.2 Helium in Nuclear Technologies	7
2.3 Helium Production Techniques for Laboratory Analysis	10
2.4 Athermal Helium Bubble Growth	12
2.5 Athermal Helium-Induced Surface Blistering	13
2.6 Helium Effects on Mechanical Properties	18
3 Low Energy Ion Implantation	24
3.1 Background and Motivation	24
3.2 Mechanical and Structural Transformation of He Implanted Ti(0001)	27
3.3 Comparative He Implantation and Characterization of Cu(100), Ti(0001), and Ti(10 $\bar{1}$ 0)	38
3.4 Positron Annihilation Spectroscopy and Shock Loading of Helium Ion Implanted cp-Ti	48
4 High Energy Ion Implantation	58
4.1 Background and Motivation	58
4.2 Preliminary Study at the 88-Inch Cyclotron	61
4.3 Properties of a Helium Ion Beam Degradar for the 88-Inch Cyclotron	76
5 Summary and Future Work	94
6 Appendix A	96

7 Appendix B	105
Bibliography	111

List of Figures

2.1	The interaction of high-energy particles with nuclei of a solid lattice can lead to displacement damage (vacancies and interstitials) and nuclear reactions (e.g. He created from (n,α) reactions). Vacancies, interstitials, and He atoms are mobile, and will undergo defect reactions, some of which are represented here. One important defect reaction which is missing from this image is vacancy-interstitial recombination, which results in no damage. This figure is adapted from [19] with permission by the IAEA. Copyright IAEA.	5
2.2	(n,α) reaction cross sections for a variety of metals and neutron energies, adapted with permission from [21]. There is a steep increase in reaction cross section with respect to increasing neutron energy, and thus the importance of He effects in a fusion spectrum due to the high portion of 14.1 MeV neutrons. Copyright 1984 Trans Tech Publications, Ltd.	8
2.3	TEM images showing nm-sized He bubbles in aged Pu. The same region is imaged with different focusing conditions (a) Underfocused image shows He bubbles as white contrast, indicated by arrows (b) Overfocused image shows He bubbles as dark contrast, indicated by arrows and (c) Focused image shows no contrast from the He bubbles. Reproduced with permission from [25] under the Creative Commons copyright license CC BY-NC-SA 4.0.	10
2.4	He production and displacement damage attainable in 1 year assuming a plant factor of 100% and austenitic stainless steel in the maximum flux position of various irradiation sources [21, 29, 30, 31].	11
2.5	Schematic of the inter-bubble fracture model, adapted from [38],[40]. At some depth below the surface, likely the maximum He concentration, He bubbles become overpressurized enough (P_F) to break through the material in-between the bubbles, thereby creating a crack. The red and blue arrows correspond to tensile and compressive stresses caused by the overpressurised bubbles, respectively. Due to the difference in crack pressure, P_C , and adjacent bubbles pressure, P_O , it is proposed adjacent bubbles break into the crack, eventually widening the crack to a penny-like shape which becomes domed-up due to He gas pressure.	13

- 2.6 Schematic of the lateral stress model, adapted from [41]. Stress concentrations are proposed to arise from the near-surface He bubbles, thereby creating a weakened interface region by shear yielding at stress concentration points S_{max} , which is proportional to the yield stress of the material. The plate buckles when the weakened interface has exceeded the value where elastic instability can occur. 14
- 2.7 Montage of TEM micrographs simulating the cross section of a He blister formed in Cu by 160 keV ion implantation at $\sim 0.2T_m$, adapted with permission from Johnson et al. [42]. The high magnification images reveal a bimodal bubble size distribution. Johnson et al. concluded that the blister formed when the nanobubbled column between the large cavities failed by cracking, and the blister shape was created by a combination of gas pressure and lateral stress. Copyright 1999 Elsevier. 15
- 2.8 TEM micrographs of Cu implanted with 25 keV He ions at room temperature to (left) 5×10^{17} ions/cm² and (right) 1×10^{18} ions/cm², adapted with permission from [43]. (Left) The bubble size distribution right before blistering was fairly uniform, while (right) the bubble distribution upon blistering was bimodal. (Right inset) Larger faceted cavities were also observed in the blistered sample. Copyright 2018 Elsevier. 16
- 2.9 STEM micrographs of W(100) implanted with 25 keV He ions at room temperature, adapted with permission from [44]. (a) Cross section of the entire blister profile annotated with the SRIM-calculated range of He ions; the blister crack was observed at the peak He concentration. (b) He bubble distribution shows a network of nm-size bubbles and (c) the linkage of these small bubbles to form nanocracks. Copyright 2020 Elsevier. 17
- 2.10 Summary of He bubble structures observed in Cu [42, 43] and W [44, 45]. (a) In Cu, He blisters formed due to bubble growth and coalescence, creating large cavities which bisect and dome up to cause significant plastic deformation (large blister cavities). (b) In W, He blisters formed due to crack formation resulting from the linkage of small bubbles, and less plastic deformation (smaller blister cavities) was observed compared to Cu. 18
- 2.11 Embrittlement observed in Cu into which He was introduced by ³H decay at 200 °C, reproduced with permission from [35, 48]. (a) Cavities formed along a grain boundary as a result of He bubble coalescence. (b) Tensile testing revealed a decrease in ductility of the He-containing specimens. (c) SEM micrographs of the fracture surface reveal intergranular fracture induced by the He accumulation. Copyright 1986 Elsevier. 19
- 2.12 TEM of He bubbles in Al-¹⁰B before (a) and after (b) shock loading, reproduced with permission from [50]. The TEM samples were made from a region near the spall plane. The impact caused the He bubble size to grow from approximately 5 nm to 200 nm. Copyright 2010 Springer Nature. 20

2.13	Swelling with respect to dose in Cu, W, and V, compiled from [43, 44, 46]. All samples were implanted at room temperature and with 25 keV He ions. For all cases, the relationship between dose and swelling is nearly-linear. Moreover, Cu and V follow a similar trend, while W exhibited less swelling at high doses. . . .	22
2.14	Hardness and elastic modulus with respect to dose in Cu (a),(b) and V (c),(d). Both samples were implanted at room temperature and with 25 keV He ions. The results reveal competition between hardening and softening at doses on the order of 10^{17} ions/cm ² . Additionally, the elastic modulus decreases with respect to dose for both materials. The Cu results are reproduced with permission from [43], Copyright 2018 Elsevier. The V results are reproduced with permission from [46], Copyright 2021 Springer Nature.	22
2.15	Compression testing of Cu nanopilars implanted with He at high temperatures, reproduced with permission from [35, 54]. The He bubbles appear to (a) enhance flow stress and (b) promote dislocation slip. Copyright 2016 American Chemical Society.	23
2.16	(a)-(c) In-situ bending test of small-volume Cu implanted with He at high temperatures, reproduced with permission from [35, 54]. (a),(b) reveal the emission of a partial dislocation from a He bubble, leaving behind a stacking fault as shown in (c). It is worth noting that the He bubbles in these micrographs appear fauceted, indicating they are not at equilibrium pressure. This could be due to the high-temperature used during irradiation, which promotes a low He/vac ratio. Atomistic calculations shown in (d)-(f) are also reproduced with permission from [35, 54]. (d),(e) show that bubbles are preferential dislocation nucleation sites compared to the corner of the nanopillar. (f) demonstrates that slip steps on the bubble surface also serve as dislocation nucleation sites. Copyright 2016 American Chemical Society.	23
3.1	HIM implantation dose and resulting SRIM-calculated defect densities and TEM-observed defect structures in Cu and Si, adapted with permission from Livengood et al [45, 59]. He bubbles and blisters were observed at doses above 1×10^{17} ions/cm ² . Copyright 2009 American Vacuum Society	25
3.2	The fate of a positron after implantation in a host material. When positrons enter a material, they thermalize, diffuse, and then annihilate with electrons in the material which can result in two 511 keV gamma rays. This process is sensitive to areas with lower electron densities, such as vacancies. The resulting gamma ray spectra can be used to extract information on vacancy size and concentration in materials. Reproduced from [65], copyright 2013 Dr. Maik Butterling.	27
3.3	(a) Map and (b) corresponding description of parameters for the 16 He implants in the initial Ti(0001) study. The He dose was varied for the first implant set, 1-12. The dose rate was varied for the second set of implants, 13-16.	28

3.4	He ion and vacancy distributions of 25 keV He in solid Ti calculated by SRIM, assuming constant bulk density of the target. The He concentration peaks around 165 nm, and the max implantation depth is about 329 nm.	29
3.5	Dpa calculated from SRIM simulation of solid Ti subjected to various fluences of 25 keV He ions, assuming constant bulk density of the target. The displacement damage peaks at a depth of about 122 nm. The dpa for the $10 \times 10 \mu\text{m}^2$ implants to various doses range from 78 to 2 dpa. The dpa for the $5 \times 5 \mu\text{m}^2$ implants to a dose of 1×10^{17} ions/cm ² was about 3 dpa.	30
3.6	FIB technique showing the process of TEM specimen preparation sequentially. (a) SEM image of 3 blisters from 25 keV He implantation in Ti. The implant area was $10 \times 10 \mu\text{m}^2$ and dose was 7.4×10^{17} ions/cm ² . (b) Pt deposition to protect the two blisters selected for cross-sectioning. (c) Trenches were milled on either side of the two blisters and and the U-cut to allow for removal from the bulk material. (d) The Omniprobe was welded to the Pt, and then the bridge of the U-cut was milled. The sample is shown being removed from the bulk. (e) The sample, welded to the Omniprobe, being positioned for welding on the Cu TEM grid. The edge of the Cu grid was milled to assist the welding. (f) After Pt welding the sample to the grid and cutting the Omniprobe from the sample. (g) After some thinning, the beginning of the 2 blister cavities were already visible. (h) SEM image of the two blisters in cross section after final thinning. (i) The final thickness of the TEM sample was around 70 nm.	31
3.7	Visual summary of the methods used in the initial Ti(0001) studies. (a) Local ion implantations were performed using the HIM, followed by (b) a series of post-implantation characterization techniques.	31
3.8	Ti(0001) swelling as a function of 25 keV He (a) dose and (b) dose rate, as measured by AFM.	32
3.9	Average (a) hardness and (b) storage modulus of implanted and nonimplanted Ti(0001). Both plots share the same legend. (a) The hardness results show a competition between radiation hardening and softening, with an increase in hardness at a dose of 2×10^{17} ions/cm ² and then decreasing with doses above 7×10^{17} ions/cm ² . (b) The storage modulus decreases with increasing He dose.	33
3.10	Loading and hardness curves from a single indent for (a) 7×10^{17} ions/cm ² (b) 4×10^{17} ions/cm ² (c) 2×10^{17} ions/cm ² and (d) nonirradiated regions of single crystal Ti(0001). For (a)-(c), pop-in behavior is indicated with circles and arrows. No pop-in behavior is observed in (d).	34

3.11	TEM results for a cross-section through blisters in the Ti(0001) sample formed by 25 keV He ion implantation to a dose of 7×10^{17} ions/cm ² . (a) TEM micrograph of the blisters showing a smaller (left) and larger (right) blister cavity. The boxes represent the micrographs shown in (b). (b) -500 nm defocus TEM micrographs of the large blister cavity cap (top) and base (bottom). In this defocus condition, the He bubbles appear as white contrast in the sample. (c) SRIM results of 25 keV He ions in Ti with constant theoretical density and with a reduced density of density of 3.5 g/cm ³ , to scale for comparison with (b). The arrows point to the peak He concentration for each respective simulation. Determination of the reduced density is described in the Analysis section. (d) Duplicate of (b), showing a region of the blister base and near the blister cavity, partially annotated to show nano-crack formation.	36
3.12	Bubble diameter and area ratio as a function of depth for the dose of 7.4×10^{17} ions/cm ² . As the depth into the samples increases, small bubbles linked to form nanocracks. An attempt was to count these bubbles individually versus quantifying the nanocrack size overall, which is why the average bubble size does not increase with respect to depth into the sample. Additionally, denuded zones appeared to surround the nanocrack, which is why the area ratio was not observed to increase with respect to depth either. It must be noted that significant errors exist with analyzing of small (nm-size) defects in TEM images. Errors were not quantified here, and the TEM resolution limited the ability to quantify all of the bubbles.	37
3.13	HIM implantations and parameters for (a) Cu(100), (b) Ti(0001) and (c) Ti(10 $\bar{1}$ 0).	39
3.14	He ion and vacancy distributions of 25 keV He in solid Cu calculated by SRIM, assuming constant bulk density of the target. The He concentration peaks around 110 nm, and the max implantation depth is about 255 nm.	40
3.15	Schematic of the placement of the nanoindenter on the blister (a) before, (b) during (assuming maximum displacement), and (b) after each indentation. For simplicity, indentation into the layer is not represented in this diagram, although this would occur at the same time.	40
3.16	Swelling versus dose for Cu(100), Ti(0001), and Ti(10 $\bar{1}$ 0) measured in this study, as well as the Ti(0001) result from Section 3.2 above polycrystalline Cu result from Yang et al. [43]. For all materials, the swelling increases linearly with respect to dose, and the slope of this relationship is fairly constant across these materials.	41

- 3.17 Displacement-controlled nanoindentation of a single blister from 1×10^{18} ions/cm² He ions in Cu(100). (a) Load-displacement curves for the series of indents. Up to 180 nm, the load-displacement curves followed the same path, and therefore the blister behaved elastically. Plastic deformation was observed at 180 nm displacement, and the Cu under the blister is presumably sampled. (b) AFM of the implant produced with the AFM on the nanoindenter. The red circle is showing the blister to be indented. (c) AFM of the blister after indentation, produced with the AFM on the nanoindenter. 43
- 3.18 Displacement-controlled nanoindentation of a single blister from 5×10^{17} ions/cm² He ions in Ti(0001). (a) Load-displacement curves for the series of indents. Plastic deformation was observed immediately, at 20 nm displacement. (b) AFM of the implant produced with the AFM on the nanoindenter. The red circle is showing the blister to be indented. There was significant noise in the AFM signal, and/or buildup on the indenter tip. (c) AFM of the blister after indentation, produced with the AFM on the nanoindenter. 44
- 3.19 Displacement-controlled nanoindentation of a single blister from 8×10^{17} ions/cm² He ions in Ti(10 $\bar{1}$ 0). (a) Load-displacement curves for the series of indents. Plastic deformation was observed immediately, at 20 nm displacement. (b) AFM of the implant produced with the AFM on the nanoindenter. The red circle is showing the blister to be indented. (c) AFM of the blister after indentation, produced with the AFM on the nanoindenter. 44
- 3.20 SEM images of two $10 \times 10 \mu\text{m}^2$ area and 1×10^{18} ions/cm² dose implants in Cu(100). Both implants had a single large He blister visible. One of the bubbles were indented in the nanoindentation experiment of Section 3.3.2.3 above. The indentation is clearly visible in the center of the blister. Both blisters were cross-sectioned for STEM investigation. 45
- 3.21 STEM micrographs of the not-indented Cu(100) blister, from a dose of 1×10^{18} ions/cm². (a)-(c) Low-magnification secondary electron (SE), high-angle annular dark-field (HAADF), and dark field (DF) images of the blister cavity and surrounding non-blistered implantation regions. (d)-(f) Higher-magnification SE, HAADF, and DF images of the blister cavity. (d)-(f) Higher-magnification SE, HAADF, and DF images of the blister cavity edge. 45
- 3.22 STEM micrographs of the indented Cu(100) blister, from a dose of 1×10^{18} ions/cm². (a)-(c) Low-magnification secondary electron (SE), high-angle annular dark-field (HAADF), and dark field (DF) images of the indented blister cavity and surrounding non-blistered implantation regions. (d)-(f) SE, HAADF, and DF images of the indented blister cavity. (d)-(f) Higher-magnification SE, HAADF, and DF images of an implanted region surrounding the indented blister. 46
- 3.23 SEM micrograph of a liftout of two blisters from an 8×10^{17} ions/cm² implant in Ti(10 $\bar{1}$ 0). The sample was top-mounted to a TEM grid to allow for in-situ picoindentation, and the sample was thinned to ~ 100 nm. 47

3.24	TEM micrographs of the 8×10^{17} ions/cm ² blisters in Ti(10 $\bar{1}$ 0), after indentation; (a) is in focus, while (b)-(e) are slightly underfocused. (a) Placement of the picointender during the experiment. (b) Close-up of the not-indenting blister, which still ruptured and a crack grew into the sample. (c)-(e) Stitched higher-magnification images of the blister shown in (b).	47
3.25	Sample dimension requirements for plate impact experiments. The smaller diameter side of the sample was polished, then implanted. For the shock loaded sample, the polished and implanted side was also the impact side.	49
3.26	(a) Non-polarized and corresponding (b) polarized optical micrographs of an example cp-Ti sample surface after polishing at UC Berkeley.	50
3.27	He ion and vacancy distributions of 60 keV He in solid Ti calculated by SRIM, assuming constant bulk density of the target. The He concentration peaks around 324 nm, and the max implantation depth is about 522 nm	51
3.28	DB-VEPAS results from the (a) LANL polished sample set and (b) UC Berkeley polished sample set. The results agree well, with the UC Berkeley set having slightly less surface defects. The S-parameter, and thus the vacancy concentration and/or size, increases with respect to dose. Additionally, this increase is observed at increasing depths into the samples with increasing dose, therefore confirming swelling results. The shocked 8×10^{16} ions/cm ² sample showed a decrease in vacancy defects compared to the not-shocked 8×10^{16} ions/cm ² sample.	53
3.29	VEPALS results for the LANL polished samples. (a) The average positron lifetime, τ_{av} , increases with respect to dose and corresponds well to the S-parameter results, indicating defect size is a dominating factor. (b) Defect sizes calculated from the lifetime components revealed small (3 and 4) vacancy agglomerations from the shorter lifetime τ_1 , and larger vacancy agglomerations (>50) from the longer lifetime τ_2 [84]. (c) The density (relative intensity) of the vacancy agglomerations increases with dose.	54
3.30	The DB-VEPAS results of the LANL-polished samples are in good agreement with our previous results. The inset image is to scale with the graph, and is a TEM micrograph of He bubbles in Ti(0001) from the study described in Section 3.2. The implantation energy for the TEM image was 25 keV He and dose was 7.4×10^{17} ions/cm ² . The TEM image is underfocused, so He bubbles are shown as white contrast. Additionally, the projected range of 60 keV He in Ti, 296 nm, is annotated. The PALS results are in good agreement with the TEM and SRIM results.	55
3.31	Schematic of the potential for a plane of He bubbles, which are lower density than bulk Ti, to create an impedance mismatch and therefore lead to shock reflection.	56
3.32	Shock loading of the He ion implanted sample led to a decrease in S-parameter. This shows shock loading caused a decrease in vacancy defects in He implanted cp-Ti.	57

4.1	Proposed size effects of irradiated and not-irradiated polycrystalline materials, adapted with permission from [47]. For not-irradiated materials, bulk-scale properties are captured when there are a significant number of grains. A dip in strength is observed when the sample geometry is such that surface grain relaxation dominates. At the smallest sample sizes, the strength approaches the theoretical strength. For irradiated materials, it is proposed that displacement damage creates a new internal length scale, therefore diminishing size effects, although the smallest samples will also approach the theoretical strength. The proposed curve for irradiated materials only considers displacement damage, while He effects may behave differently. Copyright 2018 Elsevier.	60
4.2	Standard dimensions for SS-J tensile samples. In the size effects studies described here, the sample thicknesses were varied. 100 μm was found to be the thickness of samples needed for reliable testing with the KW at UC Berkeley.	61
4.3	Range comparison of (a) 3 MeV and (b) 22 and 23 MeV He in HT-9 steel, assuming constant theoretical density of HT-9 and calculated using SRIM-2013. The 3 MeV He is stopped in the first few μm , while 22 MeV is stopped in 100 μm HT-9, and 23 MeV penetrates through 100 μm HT-9.	62
4.4	Experimental setup of the 5.3 day HT-9 SS-J deuteron irradiation at the 88-inch Cyclotron. (a) Exploded view of the target setup. The 33 MeV deuterons (^2H) were attenuated by the Be and HT-9 layers, and the deuteron breakup on the Be produced secondary neutrons which were monitored with Ni and Y foils. (b) GAFChromic film showing the spatial beam profile on the 202 and 91 μm sample stack. (c) GAFChromic film showing the spatial beam profile on the 40 μm samples. (d) GAFChromic film measurement result with an overlay of the SS-J geometry. As shown in (b)–(d), the beam spot was about 0.38 cm^2 and centred on the SS-J gauge region so the grippers were not irradiated.	63
4.5	Dpa as a function of depth into the HT-9 samples, calculated from SRIM-2013 code. The average dpa was 0.18, 0.2, and 0.22 for the 202 μm , 91 μm , and 40 μm samples, respectively.	64
4.6	Gamma spectrum from all four HT-9 SS-J samples measured 5 months following the 33 MeV deuteron irradiation. The samples were counted in a lead pig 2 m away from the front of the HPGe detector. The majority of the measured radioactivity was from ^{56}Co , whose photopeaks are indicated in red.	65
4.7	Effect of 0.18, 0.2, and 0.22 dpa deuteron irradiation on the stress strain curve production of 202 μm , 90 μm , and 40 μm thick HT-9 SS-J tensile samples, respectively. An increase in YS and reduction in ductility is observed, indicating radiation hardening. Corresponding SEM images of the failure surfaces for are shown on the right, showing an intermediate ductile/brittle failure mechanism.	69

4.8	TEM investigation of the 40 μm thick, 7 mR/hr sample. The TEM lamella was taken from the irradiated gauge section and far from the tensile fracture site. (a)-(b) A comparison of the same region without two beam and with two beam conditions, Black dot irradiation defects are revealed by the two beam condition. (c) Annotated version of (b), used in (d)-(f) to exemplify the method used to quantify the black dot defects. (d) Magnified area, annotated in (e),(f) as an example of a high and low estimate for the black dot radiation defect size and number.	70
4.9	Effects of 0.18–0.22 dpa deuteron irradiation on thickness dependence of YS, UTS, and UE in HT-9. Unirradiated data is adapted from Dong et al. [111]. A dip is observed below approximately 200 μm in all material properties for the unirradiated samples. The irradiated samples appear to show an increased YS and UTS and decreased UE compared to the unirradiated bulk ($>200 \mu\text{m}$) properties.	72
4.10	Change in high-Cr ($\geq 9\%$ Cr) F/M steel YS (ΔYS) and % decrease in UE with respect to dose after various low temperature ($\geq 300 \text{ }^\circ\text{C}$) irradiations. The data from this study is indicated by the arrows and fits well within the larger body of data obtained in previous works [89, 90, 91, 92, 125, 126].	74
4.11	Conceptual overview of the He ion beam (α -beam) degrader. The monoenergetic ion beam passes through the degrader system, which results in a range of beam energies. The energy range of ions after passing through the degrader allows them to be implanted throughout the sample volume. For uniform implantation, the Bragg peaks should overlap throughout the sample depth.	77
4.12	Details of size parameters influencing the degrader design. (a) The minimum beamspot size to implant the gauge lengths of 5 SS-J geometry tensile samples is $20 \times 5 \text{ mm}^2$. (b) The degrader is constrained to a $21.5 \times 28 \times 28 \text{ cm}^3$ Cyclotron beam box. Vacuum-sealed flanges may be coupled to the beam box to increase this space.	78
4.13	Conceptual overview of the stippled target degrader. (a) Represents the beam passing through the region of the stippled target with most material and with the least material. The beam passing through the most stippled target material will be stopped at the front of the sample and have more beam straggling. The beam passing through the least stippled target material will stopped at the back of the sample have the least beam straggling. The smallest beam straggling radius determined the spacing of the stippled target trenches. (b) Represents how the He beam profiles have some overlap throughout the sample depth. Yet, the stippled target design proposed would result in concentration bands of He. Additional design changes are necessary for uniform He implantation in the sample. (c) Description of stippled target paramaters described in Table 4.3.	80
4.14	Some of the possible degrader designs from literature that were considered, reproduced with permission from [129] under the Creative Commons copyright license CC BY-NC-SA 4.0.	81

- 4.15 The binary step-wedge degrader meets the size constraints. (a) Top-down view of a degrader wedge, which holds up to 4 filters. The filters are large enough for the $20 \times 5 \text{ mm}^2$ beam spot. (b) The degrader step-wedge assembly and motors have a footprint of $15 \times 11 \times 13 \text{ cm}^2$, which is small enough to fit in the standard LBNL beam-box. 82
- 4.16 The binary step-wedge degrader design provides 625 of discrete energy steps. For cost efficiency, the number of filter thicknesses was minimized. An optimization code was ran, determining that by stacking filters to create an overall thickness, as shown in (a), 38, 40, 46, and 53 μm thick filters can provide the most linear combinations for energy steps. (b) The number of combinations (energy steps) that can be made with the wedges show in (a). The most linear region is 1-2 μm steps. (c) From the degrader filter combinations shown in (b), the most linear region (starting at 150 μm overall Si thickness) is used. It was determined that 29 MeV He and a range of 150 to 413 μm Si is needed for implanting 100 μm HT-9. This region contains 206 combinations and therefore provides 206 energy steps. Of these 206 energy steps, the Bragg curves of only 6 (every $\sim 50 \mu\text{m}$) were calculated using SRIM and are plotted here. Since the actual steps are 1-2 μm , there would be a significant amount of overlap if all of the steps were plotted. 82
- 4.17 Overview of the complete degrader assembly. The degrader box is connected to the cyclotron beamline and the entire system is under vacuum. The α (He ion) beam is first incident on the collimator, where it is flattened and shaped. Then, the beam is degraded, resulting in a range of energies for implantation in the samples. The samples are held in the beam stop and sample holder assembly, which is connected to the degrader box with a flange. 86
- 4.18 Image of the collimator assembly on the front of the degrader box (not the beam box). The collimator is made out of OFHC Cu for effective heat transfer. A water cooling channel runs through the collimator, with an inlet and outlet connection. The collimator is instrumented with a thermocouple to monitor its temperature. Additionally, the collimator can easily be changed to adjust the beam geometry. 87
- 4.19 Time to achieve at% He in a single SS-J sample. The experimental configurations considered at (a) 1, (b) 2, (c) 3, (d) 4, and (b) 1 HT-9 SS-J sample(s), as well as incident beam currents of 5, 10, and 20 μA . These graphs show that when the number of samples, in the implantation decrease, we can decrease the beam spot size. This increases the beam current incident on each sample, and therefore decreases the time required to achieve a specific at% He. The interchangeability of the collimator can accommodate different beam spot sizes and thus different beam time requirements. Additionally, the graphs also show the time to achieve an at% He decreases with increasing cyclotron beam current. 88

- 4.20 Detail of the degrader step-wedge sub assembly. (a) One of the step wedges assembled with filters. The step-wedge is made out of OFHC Cu. The filters are loosely held to allow for thermal expansion. The filters are also easily interchangeable for experimental flexibility. The “worst-case” wedge, being the wedge with the thickest filters, is instrumented with two thermocouples to measure both the thickest filter and the wedge base temperature. (b) There is a cooling channel that runs through the entire wedge and barbed inlet/outlet connections. (c) Since the motors are used in vacuum, it is imperative that they are cooled. A motors water-cooling jacket was made out of OFHC Cu. The motor cooling jacket is thermocouple instrumented. (d) One of the degrader wedges and zero microswitches, along with the full motors and driving shafts and pinions. Also shown is a custom x-y stage to position this degrader box in line with the beam. 89
- 4.21 (a) Front and (b) back view of the beam stop assembly, which is made out of OFHC Cu. (a) 5 SS-J samples clamped in place. The clamping mechanism also performs as a mask. The opening is tapered to prevent shadowing. (b) The beamstop has water cooling channels throughout and is instrumented with thermocouples for monitoring the sample and water temperatures. 89

List of Tables

4.1	Summary of paramaters and proprieties for irradiated and not-irradiated SS-J geometry HT-9 tensile samples tested at UC Berkeley [111, 113]	67
4.2	Experimental parameters and references used for the construction of Figure 4.10. Irradiations took place at the 88-Inch Cyclotron, Fast Flux Test Reactor (FFTF), Los Alamos Neutron Science Center (LANSCE) spallation source, Proton Irradiation Experiment (PIREX) accelerator, and the Experimental Breeder Reactor II (EBR-II). All tensile testing was conducted at room temperature.	73
4.3	Stippled target design paramaters for a variety of target stacking configurations. The paramaters are described visually in Figure 4.13(c). The He ion beam energy and straggling radius was determined by SRIM-2013 simulation.	79
4.4	Mechanical design matrix for the wheel, wedge, step-wide, and cassette degrader designs. The following were taken into consideration: the ability to cool the degrader filters; the simplicity of the physical design and water system; the number of different thickness filters needed; the mechanical stresses on the filters due to how they would be held and thermal expansion; the mechanical mechanism for movement; and the filter production costs. The green/red indicates pros/cons that were heavily weighted. As a result, the step-wedge degrader design was pursued.	84
4.5	Design matrix for the filter material selection. *Radionuclide production data was found using JANIS [132]. Only nuclides with half-lives ($t_{1/2}$) longer than a couple of days are listed. Up to 85 MeV α 's were considered. The filter material should have a relatively low density (ρ), high thermal conductivity (k), and high melting temperature T_m . "Y" refers to yes, and "N" refers to no. It should be noted that these properties are for bulk and may not translate to thin film properties. Additional considerations include the ability to machine the material and the ability to find commercially available thin foils. Suppliers were identified and an initial cost comparison was conducted. Boxes highlighted in red indicated negative weighting factors. Graphite is in red because the carbon will diffuse into our samples, so this material cannot be used. As a result of this weighting matrix, Si and SiC were determined to bne the ideal filter materials.	85

4.6	Energy balance for the thinnest degrader filter (150 μm) configuration, assuming 29 MeV He and 20 μA current into the system. The majority of the thermal power is dissipated in the collimator and the beamstop.	90
4.7	Energy balance for the thickest degrader filter (413 μm) configuration, assuming 29 MeV He and 20 μA current into the system. The majority of the thermal power is dissipated in the collimator and the filter.	90
4.8	Complete list of inputs and outputs of the software, as well as corresponding limits warranting a warning alarm and/or emergency shutdown.	92
7.1	Ion beam degrader wedge position table. There are 165 combinations presented, which allow for 165 levels of degradation.	106

Acknowledgments

This work was made possible by the University of California, Berkeley Chancellor's Fellowship; Lawrence Berkeley National Laboratory Bridge Fellowship; U.S. Department of Energy (DOE) Office of Nuclear Energy Integrated University Program Fellowship; DOE National Nuclear Security Administration Nuclear Science and Security Consortium Fellowship, under Award Number DE-NA0003996; and the National Science Foundation Division of Materials Research.

To my advisor, Prof. Peter Hosemann, thank you for being a constant source of encouragement and knowledge throughout my graduate studies. I am grateful for your guidance, along with that of my committee members, Prof. Lee Bernstein and Prof. Mary Scott.

I am blessed to have friends and family, especially my parents, my brother, Eric, Angelica, Heather, and Priya, who support me in all I do. Thank you for keeping me motivated and always being there, even from thousands of miles away.

As my degree comes to an end, I am overwhelmed with gratitude for the opportunities I've had throughout my college career, and for the friends, colleagues, and mentors along the way, including: Dr. Melanie Derby, Dr. Jessica Dwyer, Minh Mac, Dr. Douglas McGregor, Dr. Michael Reichenberger, Dr. Jeff Geuther, Dr. Jeremy Roberts, Dr. Dan Nichols, Max Nager, Robert Seymour, Saqr Alshogeahri, Andres Coronado, Hai Vo, Gabrielle Dupree-Fogle, Troy Unruh, Dr. Jean-François Villard, Stephane Breaud, Dr. Grégoire de Izarra, Christelle Maitre, Dr. Collin Delker, Dr. Jeff Graham, Dr. James Bevins, Dr. Karl van Bibber, Dr. Yang Yang, Dr. Mehdi Balooch, Dr. Adi Ben-Artzy, Dr. Hi Vo, AJ Gubser, Jeff Bickel, Andrew Dong, Evan Still, Dr. Sally Benson, Dr. Costa Samaras, Dr. Rian Bahran, Rachel Reolfi, and many others. Thank you for your consideration, and helping shape the scientist and person I am today.

Chapter 1

Introduction

“America is at an inflection point — one of those moments that determine the shape of everything that’s to come after — and at the center of this is technology.”

— POTUS, *Remarks to the Fall 2022 White House Intern Class*

Recent legislation passed through the Bipartisan Infrastructure Law (BIL), the Inflation Reduction Act of 2022 (IRA), and the CHIPS & Science Act authorizes significant funding for science and technology research, development, and deployment. These investments position the U.S. to undergo a technological revolution reminiscent to that of the post-World War II era.

A major priority reflected in these policies is addressing the climate crisis. To meet emissions reductions goals, the nation’s energy system must be transformed. Taken together, the BIL, the IRA, and the CHIPS & Science Act provide about $1/2$ a trillion dollars to clean energy in the U.S. [1].

Clean firm power technologies such as nuclear is needed in the energy portfolio [2, 3]. Currently, nuclear energy provides over half of America’s carbon free electricity, and is the most reliable source of energy in the nation [4]. However, nuclear power has been projected to decrease in the U.S. energy mix, as more reactors retire than come online [5, 6].

Economic factors have led to premature closures of 13 reactors in the past decade [7]. The recently established Civil Nuclear Credit Program under the BIL provides \$6 billion to support the continued operation of existing reactors that are economically at risk. In addition to shifting energy markets and other economic factors, aging is a concern for the U.S. power reactor fleet. There are currently 92 power reactors operating in the U.S. and these plants are 40 years old on average [8]. 88 of these reactors have received approval for their first 20-year life extensions, the majority of which will expire in the 2030’s. So far, 20 reactors intend to or have applied for an additional 20 year extension, operating up to 80 years.

Advanced fission and fusion reactors may also join the future U.S. clean energy portfolio. Congress has taken part in supporting the advanced nuclear industry, passing legislation such as the 2019 Nuclear Energy Innovation and Modernization Act. This law requires the U.S. Nuclear Regulatory Commission (NRC) to develop the regulatory framework for advanced fission and fusion technologies by 2027. Additionally, the 2019 National Defense Authoriza-

tion Act included the requirement of the construction and operation of a microreactor at a Department of Defense (DoD) facility by 2027, leading to the 2022 Request for Proposals for a microreactor at Eielson Air Force Base. Moreover, the authorization of the National Reactor Innovation Center (NRIC) and appropriation of the Advanced Reactor Demonstration Program (ARDP) enables the testing of advanced reactor concepts beginning in the mid-to-late 2020's. The ARDP received an additional \$2.5 billion under the BIL, building on the initial \$160 million investment [9].

The successful commercialization and scale-up of advanced fission and fusion reactors will require robust public-private partnerships. There are currently 64 advanced nuclear projects or private companies in the U.S. and a total of 149 worldwide [10]. As part of cost shares under the ARDP, U.S.-based companies X-Energy, Kairos Power, and TerraPower have announced sites for their first units and demonstrations. Additionally, many advanced reactor developers are in the pre-application process with the NRC.

The commercialization of fusion energy has received significant support recently, including the White House release of a “Bold Decadal Vision for Commercial Fusion Energy” in 2022, and the over \$5 billion in private capital investment in U.S. fusion companies to date. The recent achievement of ignition at Lawrence Livermore National Laboratory’s National Ignition Facility, which has significant national security ramifications, has further piqued interest in fusion for the future of clean energy [11, 12].

Beyond its benefits to the climate, nuclear energy can help meet energy security and national security objectives. The ongoing war in Ukraine has underpinned the need for the U.S. to maintain a robust nuclear industrial base, and to regain and retain nuclear energy leadership worldwide. In particular, the U.S. is moving forward with plans to onshore the capability to supply high-assay low-enriched uranium (HALEU), as authorized by the Energy Act of 2020 [13]. U.S. engagement in the nuclear sector results in an increased ability to shape nonproliferation, safety, and security aspects of civil nuclear energy programs.

Recent legislation has made clear the need to maintain the U.S. nuclear fleet and to progress advanced fission and fusion reactor concepts. A number of materials challenges exist for these current and future nuclear technologies. The environments under which nuclear materials perform are often extreme, and may combine corrosion, high temperatures, high stresses, long operating periods, and radiation damage. While a number of materials developments have been made for the continued safety, reliability, and economic improvement of the current fleet, maintaining a robust understanding of materials performance is necessary to reduce uncertainties associated with extended operation [14, 15]. Advanced fission and fusion reactor materials will be subjected to even harsher environments than current reactors, including higher temperatures, more radiation damage, and more corrosive environments [15]. The development and validation of new high performance materials is necessary to take these technologies from concept to reality [16, 17].

One of the major types of radiation damage effects concerning nuclear materials performance is helium (He) accumulation [18]. He is an inert and insoluble gas, and can nucleate into bubbles. Additionally, He ions carry energy and create atomic displacement damage. Even a small concentration of He can lead to changes in microstructural and mechanical

properties. One of the widely recognized He effects is high temperature embrittlement, characterized by premature and catastrophic failure. He embrittlement may limit the materials and operating temperatures that can be used in reactors [18]. Additionally, He can cause surface blistering and exfoliation, which is a prominent concern for future fusion reactor technologies [15].

This thesis aims to address fundamental research questions regarding He and sample size effects on materials. The remainder of this thesis is divided into four chapters. He effects on nuclear materials are reviewed more thoroughly in Chapter 2. Chapters 3 and 4 are divided based on the ion implantation energies (and consequently the sample volume) investigated, with “Low Energy Ion Implantation” described in Chapter 3 being on the order of 100’s of nm, and “High Energy Ion Implantation” described in Chapter 4 being on the order of 100’s of μm . A summary of this thesis work is provided in Chapter 5.

Chapter 2

Review of Helium Effects on Nuclear Materials

This chapter describes radiation-induced He effects on nuclear technologies, starting at the radiation damage event. Sources of He generation in nuclear technologies are discussed, followed by an overview of laboratory techniques used to produce He for materials testing. Microstructural effects such as He bubbles and blisters are surveyed before a review of He effects on bulk- and small-volume mechanical properties.

2.1 Radiation Damage

It is well established that macroscopically observed radiation damage effects are a consequence of two elementary interactions between the radiation and the atoms of metallic materials: (1) atomic displacements and (2) nuclear reactions. A brief overview of these fundamental interactions is represented in Figure 2.1 and described below.

2.1.1 Displacement Damage

One of the most important physical quantities for this thesis is the depth distribution of implanted ions, which is often referred to as the range. This quantity is related to the stopping power, which is the energy lost by a moving particle per unit path length. The important thing to understand about stopping power is the mechanisms by which the ion loses energy or “slows down.” When an ion travels through the lattice, it may lose energy by (1) electron interactions and (2) nuclear collisions. Electronic stopping dominates at the beginning of the ion range. As a result, ions move in straight lines until they near the end of range, when nuclear stopping takes over. Near the end of range, the probability of an ion colliding with target nuclei increases. That is, this interaction cross-section increases with decreasing ion energy. The nuclear collisions result in many scatters and a lot of energy deposition. The ions move more slowly, meaning their average mean-free-path decreases. All of the

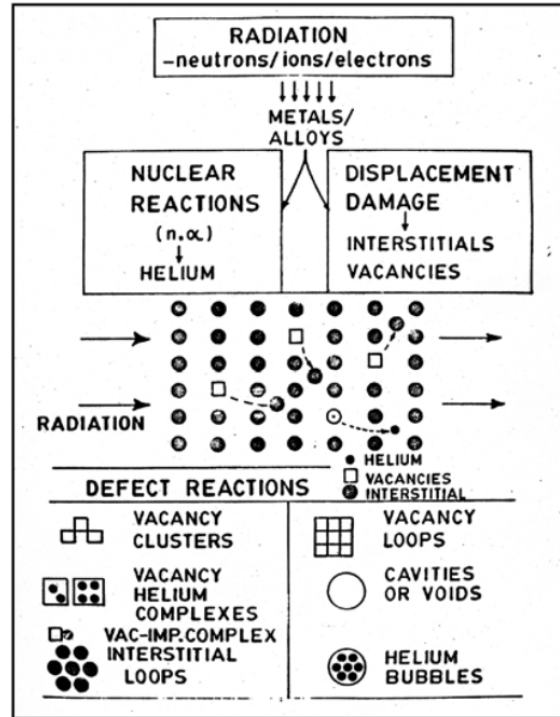


Figure 2.1: The interaction of high-energy particles with nuclei of a solid lattice can lead to displacement damage (vacancies and interstitials) and nuclear reactions (e.g. He created from (n,α) reactions). Vacancies, interstitials, and He atoms are mobile, and will undergo defect reactions, some of which are represented here. One important defect reaction which is missing from this image is vacancy-interstitial recombination, which results in no damage. This figure is adapted from [19] with permission by the IAEA. Copyright IAEA.

particle energy will be deposited within the range, and the energy-loss collisions result in displacement damage.

Displacement damage occurs when the incident particle (neutrons, ions, electrons) or residual nuclei (produced in nuclear reactions) elastically collides with a lattice atom and transfers sufficient kinetic energy to displace the atom from its lattice site. Charged particles can also displace atoms by Coulomb scattering. In general, 25-50 eV displacement energy is assumed for metals, which represents an average over all possible scattering directions. The displaced atom is referred to as the primary knock-on atom (PKA). The scattered PKA will move through the lattice and strike other atoms, known as secondary knock-on atoms (SKA), which can go on to cause further displacements, creating an atomic displacement cascade. The process will continue until the PKA cannot not transfer enough energy to cause further displacements and comes to rest as an interstitial. The magnitude of displacement damage is quantified by the number of displacements per atom (dpa), which is defined as the number of times each atom is displaced from its lattice site.

The number of displacements v created by a particle with energy E can be approximated using the Kinchin-Pease model [20]:

$$v(T) = \begin{cases} 0 & \text{for } T < E_d \\ 1 & \text{for } E_d < T < 2E_d \\ \frac{T}{2E_d} & \text{for } 2E_d < T < E_c \\ \frac{E_c}{2E_d} & \text{for } E_c < T \end{cases} \quad (2.1)$$

In Equation 2.1 above, T is the average energy transferred by the ion during a nuclear collision, E_d is the energy required to move an atom from a lattice position, and E_c is the ionization energy. For $T > E_c$, it is assumed that all energy lost is by electronic stopping. After this cutoff energy, it is assumed all energy loss is by collisions with atoms. Other important assumptions under this model are that all collisions are elastic and use the hard-sphere approximation, and the material crystal structure is ignored.

Stopping and Range of Ions in Matter (SRIM) is a Monte Carlo simulation-based software that builds upon simplistic models like Kinchin-Pease, and is widely used to compute a variety of parameters relevant to ion beam implantations. In this work, SRIM-2013 is used to compute the range, vacancy production, and dpa profiles of ions in materials. The ‘‘Detailed Calculation with full Damage Cascades’’ calculation is used, and a displacement energy of 40 keV is assumed. The ‘‘Ion Data,’’ ‘‘Target Data,’’ and ‘‘Total Number of Ions’’ inputs are dependent on the implantation parameters being simulated. The range and vacancy distributions are calculated from the range.txt and vacancy.txt SRIM output files, respectively. The dpa distribution is calculated from the vacancy.txt output file as follows:

$$dpa/depth = \frac{(SRIM\ result)(\phi)}{\rho\#} \quad (2.2)$$

$$SRIM\ Result = \frac{Knock-Ons + Vacancies}{depth} \quad (2.3)$$

$$\phi = \frac{(I)(t)}{(\#e^-/ion)(1.6 \times 10^{19} C/e^-)} \quad (2.4)$$

$$\rho\# = \frac{\rho N_a}{A} S \quad (2.5)$$

Where the *SRIM result* is calculated from the vacancy.txt output file by adding the *Knock-Ons* and *Vacancies* produced per ion at each *depth* into the target. ϕ is the number of ions, computed from the beam current I , irradiation time t , and the electron charge state of the ion ($\#e^-/ion$). ρ is the number density of the irradiated material, and can be calculated from the material density ρ , Avagadro’s number N_a , atomic mass A , and surface irradiated area S .

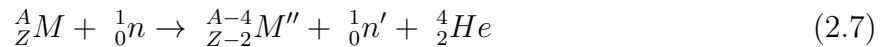
One limitation of SRIM is it assumes all targets are amorphous, so crystal structure is not taken into consideration. It is also important to note that SRIM results for He ion implantation, using constant bulk density value of the target, become increasingly inaccurate

as the dose increases, because the effective density of the target will reduce as He content increases during implantation.

The displacement cascade results in the creation of vacancy-interstitial pairs, known as Frenkel defects. Most of the vacancies and interstitials will recombine, resulting in no damage. However, defects can also cluster into loops, voids, and bubbles. These clustering reactions are controlled by the binding energies between the various species and their diffusion rates, and are strongly dependent on temperature and, in some cases, dose rate. This resulting change in microstructure leads to a change in mechanical properties.

2.1.2 Nuclear Reactions

In addition to elastic scattering, numerous other nuclear reactions can occur when the incident particle interacts with a lattice atom, and can result in considerable amounts of foreign elements in the material. The probability of a nuclear reaction occurring is quantified by the nuclear reaction cross section, which is dependent on the target element, reaction type, and incident particle energy. An important example is He generation from (n, α) transfer reactions:



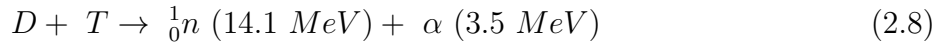
Where A and Z are the atomic weight and number, respectively, of nucleus M which interacts with a neutron n . The He produced is an inert and insoluble gas that can nucleate into bubbles and cause drastic changes in the mechanical properties of materials, even at very small concentrations. The He and new isotope also carry energy and create displacement damage. He accumulation and effects will be discussed in more detail below.

2.2 Helium in Nuclear Technologies

The (n, α) reactions mentioned above are important but not the only sources of He generation in nuclear technologies. This section reviews sources of He in fusion reactors, fission reactors, storage, and spallation sources.

2.2.1 Fusion Reactors

While (n, α) reaction cross sections vary considerably from element to element, they increase steeply with respect to neutron energy for all nuclei, as demonstrated in Figure 2.2 [21]. This makes He production especially relevant for fusion reactors. After achieving the production and confinement of a Deuterium-Tritium (D-T) plasma, the resulting 14.1 MeV neutrons will have a significant (n, α) reaction cross section for all metals:



In addition to He generated from 14.1 MeV neutron reactions, the fusion-produced 3.5 MeV alpha particles may cause significant surface modifications such as blistering. Estimates of first wall erosion at ITER, partially caused by He blistering and exfoliation, are on the order of 3 mm/burn year for low Z materials and 0.1 mm/burn year for W [22].

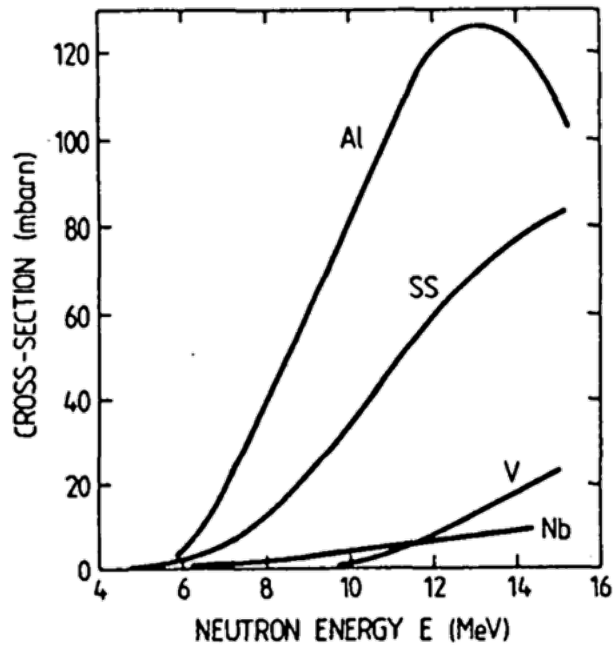


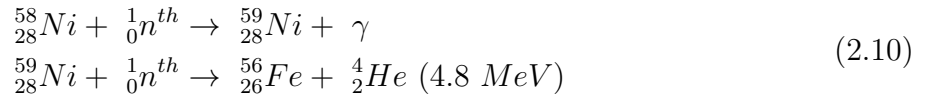
Figure 2.2: (n,α) reaction cross sections for a variety of metals and neutron energies, adapted with permission from [21]. There is a steep increase in reaction cross section with respect to increasing neutron energy, and thus the importance of He effects in a fusion spectrum due to the high portion of 14.1 MeV neutrons. Copyright 1984 Trans Tech Publications, Ltd.

2.2.2 Fission Reactors

The majority of nuclear reactors currently used worldwide are thermal neutron reactors, meaning their neutron flux spectrum is dominated by thermal (<1 eV) neutrons. For thermal neutrons, the (n,α) cross section is significant for ${}^{10}\text{B}$ containing materials:



While this ${}^{10}\text{B}$ source burns out around 1 dpa (10^{21} n/cm²) [17], there is a smaller but longer-sustained He source from Ni containing materials:



Thus, for ${}^{10}\text{B}$ or Ni containing materials in thermal reactors, especially high flux reactors, He production is significant. However, by selecting materials without ${}^{10}\text{B}$ or Ni inclusions, He generation in thermal neutron reactors can be avoided, and the majority of radiation damage in these technologies results from displacement damage.

Generation IV reactor designs are largely fast neutron reactors [23]. In these technologies, fast neutrons >1 MeV are the major source of He transmutation products, while fast neutrons ≥ 0.1 MeV mostly cause displacement damage [24].

2.2.3 Storage

Helium may also be introduced in nuclear technologies by self-irradiation, also known as alpha decay:



${}^4_2\text{He}$ is one of the most tightly bound nuclei, being a doubly magic number nuclei with a binding energy around 7 MeV. Thus, ${}^4_2\text{He}$ is emitted almost entirely by heavy nuclei, to keep these nuclei stable; instability comes from new nucleons being too far from some others to feel their short range nuclear force and Coulomb repulsion grows. Based on the conservation of energy in the alpha decay reaction, the alphas are typically emitted with a kinetic energy ~ 5 MeV.

One notable alpha decay chain is that of ${}^{239}\text{Pu}$:



Although ${}^{239}\text{Pu}$ has a half life of $>24,000$ years, the alpha decay rate is high enough to cause significant damage after a few decades [25]. Namely, the accumulation of nm-sized Helium bubbles as a result of alpha have been observed in aged Pu, as reproduced in Figure 2.3.

2.2.4 Spallation Sources

Spallation sources are often used to study the microscopic properties of materials by neutron scattering experiments [26]. Spallation neutrons are produced with a wide spectrum of energies (eV-GeV) by high energy protons (~ 1 GeV) which are accelerated into a target (typically high Z) [27]. In addition to neutrons, this reaction produces other particles, including high rates of He [28, 29]. In spallation reactions, the high energy protons produce the majority of ${}^3\text{He}$, and both protons and neutrons produce ${}^4\text{He}$.

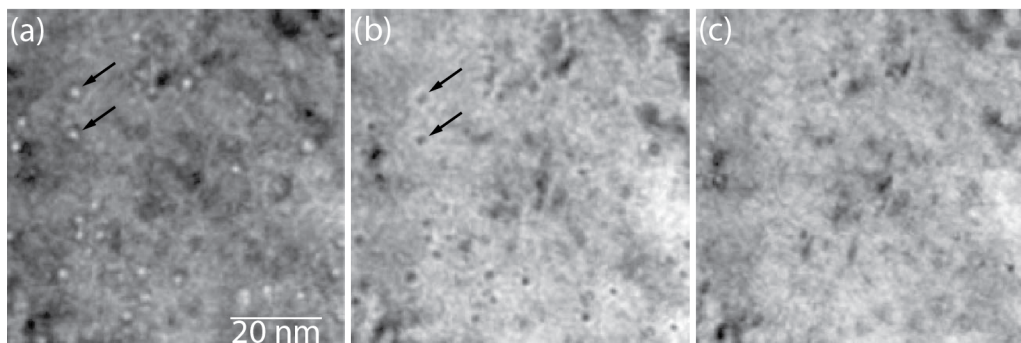


Figure 2.3: TEM images showing nm-sized He bubbles in aged Pu. The same region is imaged with different focusing conditions (a) Underfocused image shows He bubbles as white contrast, indicated by arrows (b) Overfocused image shows He bubbles as dark contrast, indicated by arrows and (c) Focused image shows no contrast from the He bubbles. Reproduced with permission from [25] under the Creative Commons copyright license CC BY-NC-SA 4.0.

2.3 Helium Production Techniques for Laboratory Analysis

Helium production techniques, such as neutron irradiation, ion implantation, and natural emitters, are used in laboratory environments to mimic operating conditions of nuclear technologies and for fundamental radiation effects studies. One important consideration when choosing an irradiation technique for nuclear technology applications is the He/dpa ratio. Figure 2.4 provides some appm/dpa ratios for fusion reactors, fission reactors, tritium storage, and spallation sources. Although the remainder of this section does not attempt to select the best He production technique for each of these devices, it is useful to consider whether irradiation sources provide combined He/dpa effects.

2.3.1 Neutron Irradiation

One method of helium production for laboratory analysis is doping materials with a nuclei that has a high (n,α) reaction cross section before irradiation in a fission reactor; oftentimes, ^{10}B is used as the dopant. This method is important for reactor materials research, due to the accompanying displacement damage created by neutrons. Additionally, it allows for He production in bulk samples, and the ^{10}B content is completely transmuted into He in short time periods, even in small reactors [17]. However, the amount of He is restricted by a doping threshold. That is, significant doping will change the properties of the material under investigation. Moreover, it is near impossible to avoid ^{10}B segregation to grain boundaries, resulting in non-uniform He production. Reactor irradiation programs can also be difficult, expensive, and time consuming, and samples are often very radioactive, requiring special precautions such as hot-cells for post-irradiation examination.

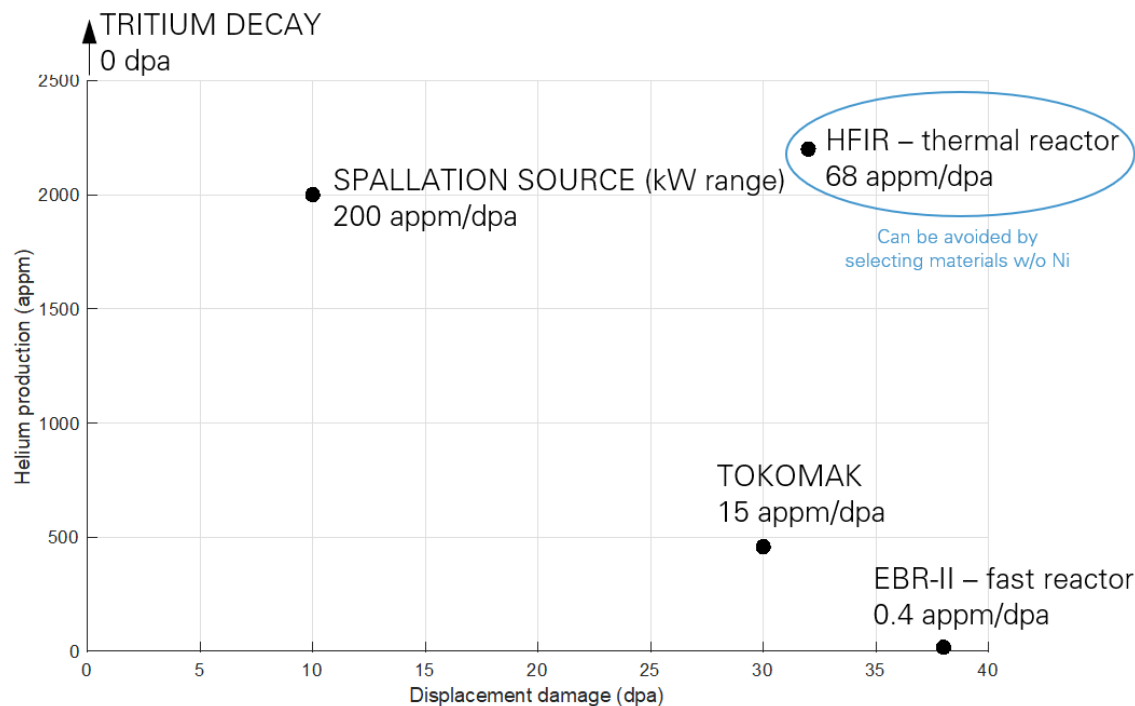


Figure 2.4: He production and displacement damage attainable in 1 year assuming a plant factor of 100% and austenitic stainless steel in the maximum flux position of various irradiation sources [21, 29, 30, 31].

2.3.2 He Ion Implantation

He ion (α -particle) implantation is another effective means for introducing He in materials. This method allows for high He production rates in all materials, and provides fine control of parameters such as temperature, fluence, dose, and implantation range. Additionally, the radioactivity induced by He ion implantation is small, so He accumulation investigations can be performed in a rapid-turnaround manner. In-situ TEM studies, which use ion beams in tandem with electron microscopes, allow for real-time observation of material transformation during He implantation [32, 33]. However, investigating combined effects of high displacement damage and He production rates and/or bulk material studies can be difficult with He ion implantation. Dual ion beams are required to investigate combined effects of high displacement damage and He production rates. High-energy He ion beams combined with ion beam degraders are required for uniform implantation in bulk-scale materials.

2.3.3 Natural He Emitters

Isotopes which naturally decay into He can also be used to generate He in materials. In particular, the “tritium trick” uses the high solubility and diffusivity of H isotopes in certain metals (Ti, V, Nb, Ta, Pd) and alloys and the H decay into ^3He with a half-life of 12.3 years

[21, 34]:



This method provides high He concentrations generated uniformly in bulk specimens and in reasonable periods of time. However, the recoil energy associated with this decay reaction is too low to create any atomic displacements. That is, neither the local defect environment of the He-atom nor the overall displacement damage of (n,α) produced He is simulated. Yet, this is a unique tool to investigate He accumulation in a defect-free lattice.

2.4 Athermal Helium Bubble Growth

During He production in materials, He and small He clusters are easily trapped by vacancies and form a sphere-like configuration of He-vac clusters with low mobility. Consequently, He-vacancy clusters deliver high binding energy, performing as sinks for He and small He-vac clusters, giving rise to He bubble nucleation and growth in metals.

The accumulation of He in materials during room temperature implantation is accompanied by displacement damage. One mode of athermal bubble growth is assumed to be by acquiring vacancies formed on the surface of He bubbles by displacement damage events. However, bubbles can also shrink as a result of the migration of mobile interstitials to the bubbles; the interstitials will be produced throughout the lattice by the displacement damage, but only a fraction will end up at the bubbles, with the remainder contributing to dislocation growth or being annihilated by vacancies.

When He bubbles are in equilibrium (eq) with the solid, the bubble pressure can be described by:

$$P_{eq} = \frac{2\gamma}{r_b} \quad (2.14)$$

Where P is the internal bubble pressure, γ is the surface tension, and r_b is the bubble radius.

During room temperature implantation, the resulting bubbles have high He/vac ratios, causing the bubbles to grow overpressurized. This leads to a second athermal bubble growth mechanism, where bubbles relieve pressure by punching out dislocation loops that have grown on the bubble surface [35, 36, 37].

$$P_{LP} = \frac{2\gamma + \mu b}{r_b} \quad (2.15)$$

Where P_{LP} is the bubble pressure for dislocation loop punching, μ is the shear modulus of the material, and b is the burgers vector of the dislocation loop.

These two athermal bubble growth regimes do not operate simultaneously [38]. Essentially, during room temperature He ion implantation, the bubbles will grow by acquiring He and vacancies until becoming overpressurized, at which point it grows and relieves pressure

by loop punching, then grows again by He/vacancy arrival, and so on. This is represented by the following equation [38]:

$$\frac{2\gamma}{r_b} \leq P \leq \frac{2\gamma + \mu b}{r_b} \quad (2.16)$$

Athermal bubble growth will continue until bubbles reach a critical radius for surface flaking or blistering, which is described in the sections below. At elevated temperatures, bubble growth via coarsening mechanisms must be considered [39].

2.5 Athermal Helium-Induced Surface Blistering

Athermal surface blistering has been observed in materials subjected to high doses of He. Historically, there are two competing theories of the underlying mechanism leading to blistering: (1) gas-driven and (2) lateral-stress driven. These models, summarized below, were largely developed before direct experimental observations like TEM of blister cross sections were available. An overview of the later experimental evidence of He bubble structures associated with blistering is also provided, followed by a summary reconciling the theories and experimental observations.

2.5.1 Inter-Bubble (Gas-Driven) He Blistering Model

One of the most prominent gas-pressure driven models for blister formation is the inter-bubble fracture model proposed by Evans [38, 40]. An overview of this model is shown in Figure 2.5.

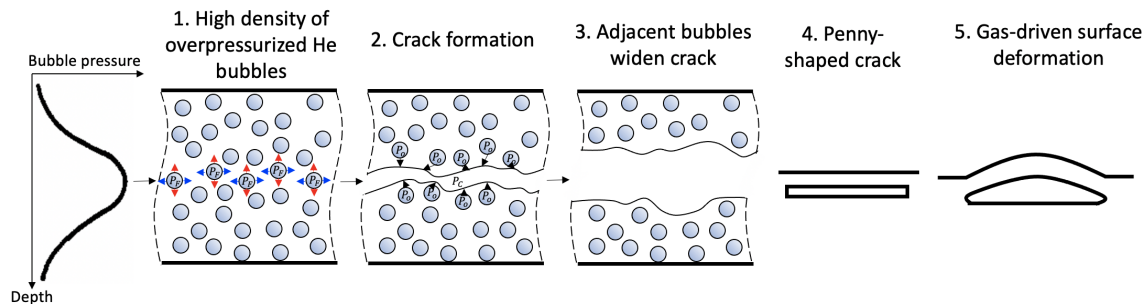


Figure 2.5: Schematic of the inter-bubble fracture model, adapted from [38],[40]. At some depth below the surface, likely the maximum He concentration, He bubbles become overpressurized enough (P_F) to break through the material in-between the bubbles, thereby creating a crack. The red and blue arrows correspond to tensile and compressive stresses caused by the overpressurised bubbles, respectively. Due to the difference in crack pressure, P_C , and adjacent bubbles pressure, P_O , it is proposed adjacent bubbles break into the crack, eventually widening the crack to a penny-like shape which becomes domed-up due to He gas pressure.

The premise of the inter-bubble fracture model is that He bubbles, likely at the max He concentration, are over-pressurized. Therefore, at some critical He dose and depth from the

incident surface, a layer of bubbles may have sufficient pressure to coalesce by “inter-bubble fracture,” creating an internal crack. If the excess pressure in the bubbles adjacent to the crack is high enough, it is possible that these individual bubbles may break into the crack, thereby causing the crack to widen; this process would stop when the pressure difference between the gas in the crack and the gas in adjacent bubbles is insufficient. The result is a penny-shaped crack which either extends to cause flaking, or forms a blister by gas-driven surface deformation.

2.5.2 Lateral Stress He Blistering Model

In the lateral stress model proposed by EerNisse and Picraux [41], the blister mechanism is idealized as a 2-D stress buckling problem. This competing model was developed when experimental results showed blister lid thickness values being appreciably larger than that of the peak He concentration, which contradicted most of the gas-driven models at the time.

As demonstrated in Figure 2.6, in the lateral stress model, the volumetric swelling associated with high He doses is proposed to cause large lateral stresses, and thus the creation of a weakened interface region by shear yielding at stress concentration points. Eventually, the material buckles, with the fracture plane under the blister being toward the end of the He range rather than the peak. One of the early criticisms of this model is the absence of blistering in analogous ion beam studies involving void swelling, where the stress-systems should be similar [38].

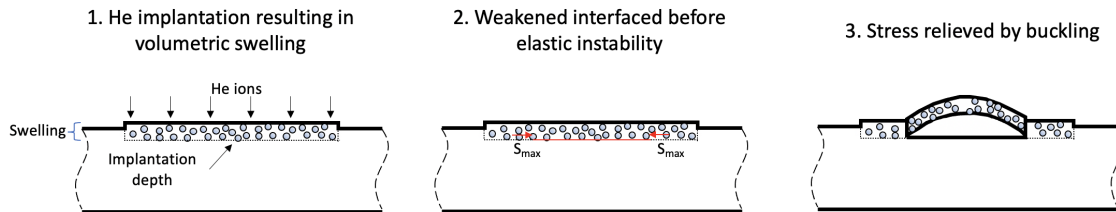


Figure 2.6: Schematic of the lateral stress model, adapted from [41]. Stress concentrations are proposed to arise from the near-surface He bubbles, thereby creating a weakened interface region by shear yielding at stress concentration points S_{max} , which is proportional to the yield stress of the material. The plate buckles when the weakened interface has exceeded the value where elastic instability can occur.

2.5.3 Observed He Bubble Structures Associated with Blistering

During the development of the aforementioned blistering models, experimental analyses of the bubble structures associated with blistering was not available. This section reviews some of the later observations of bubble structures directly associated with blistering.

2.5.3.1 He Blistering in Cu

In 1999, Johnson et al. reported the first-known TEM observation of He bubble structures associated with blistering [42]. They implanted Cu foil with 160 keV He at a temperature $\sim 0.2T_m$, and observed a critical dose for blistering of 1×10^{18} ions/cm². The TEM results reproduced in Figure 2.7 show large (30-80 nm) He bubble structures centered around the max He concentration depth. The metal columns between the large bubbles contained high concentrations of smaller bubbles. The conclusion was that a blister forms when the columns between the large bubbles fail by cracking to allow the blister cap to be domed up by some combination of gas pressure and lateral stress.

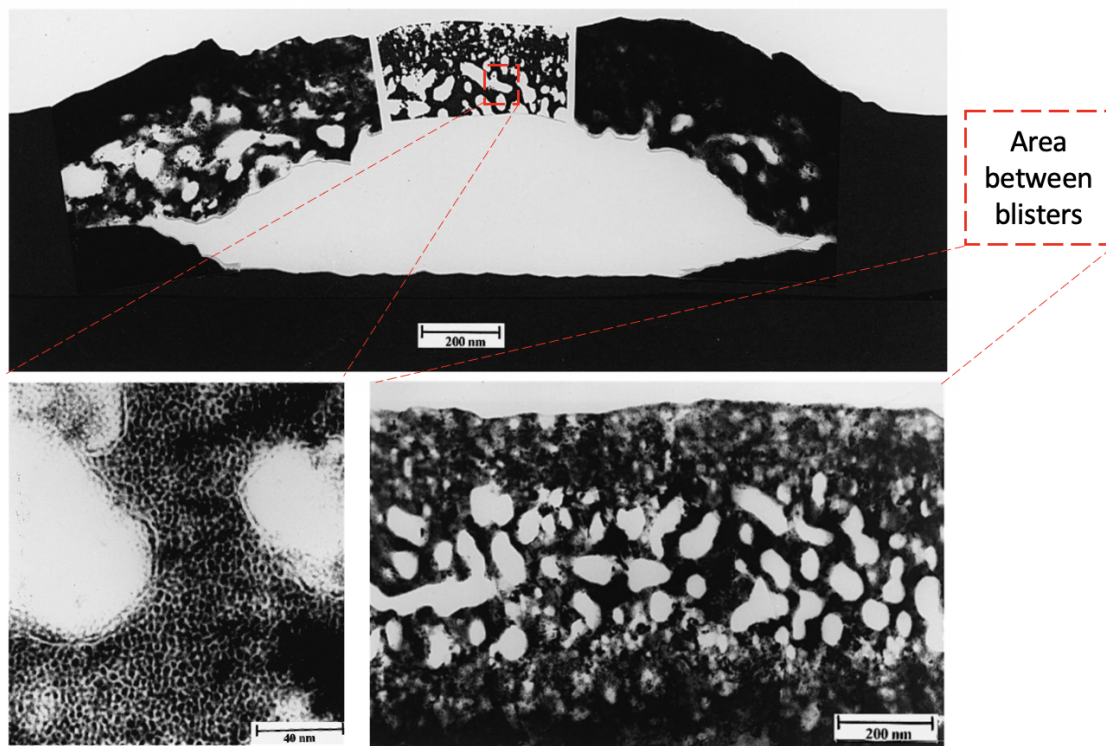


Figure 2.7: Montage of TEM micrographs simulating the cross section of a He blister formed in Cu by 160 keV ion implantation at $\sim 0.2T_m$, adapted with permission from Johnson et al. [42]. The high magnification images reveal a bimodal bubble size distribution. Johnson et al. concluded that the blister formed when the nano-bubbled column between the large cavities failed by cracking, and the blister shape was created by a combination of gas pressure and lateral stress. Copyright 1999 Elsevier.

He bubble structures associated with He implantation in Cu has also been of interest in more recent investigations. Yang et al. analyzed He bubble distributions by TEM. A Helium Ion Microscope (HIM) was used to implant 25 keV He in polycrystalline Cu [43]. The onset of blistering was observed between doses of 7×10^{17} to 1×10^{18} ions/cm². From the TEM images reproduced in Figure 2.8, it is apparent that at 5×10^{17} ions/cm², before blistering, the He bubble size distribution is fairly homogeneous, around 2.5 nm in diameter. For the

1×10^{18} ions/cm² sample with blistering, a bimodal size distribution was observed; bubbles close to the surface and bubbles near the end of the max He implantation depth were around 2 nm in diameter, while larger cavities near the peak He concentration depth were up to 17 nm in diameter. Additionally, the larger cavities were faceted and therefore below the equilibrium He bubble pressure.

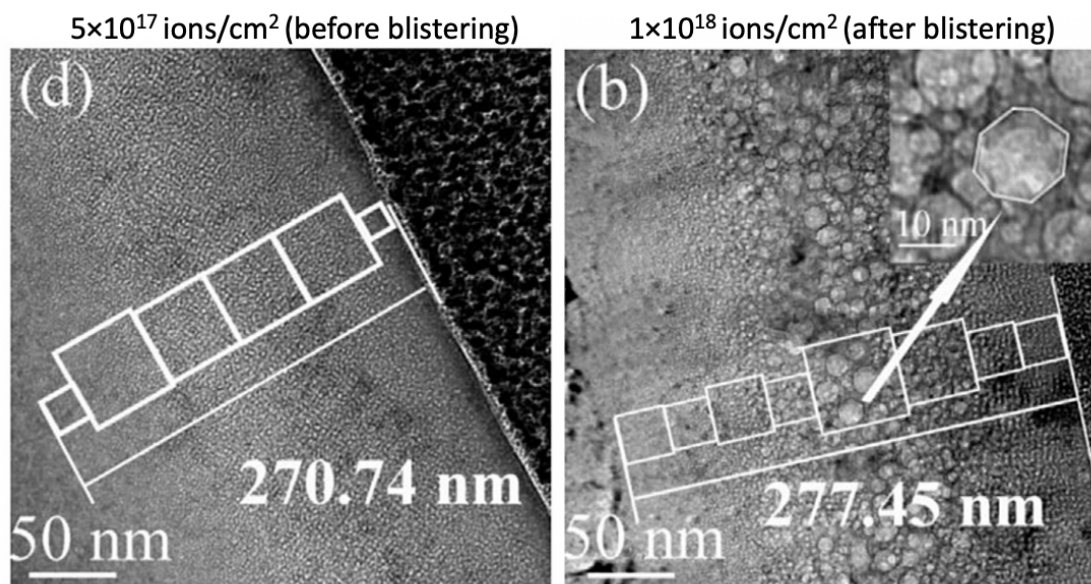


Figure 2.8: TEM micrographs of Cu implanted with 25 keV He ions at room temperature to (left) 5×10^{17} ions/cm² and (right) 1×10^{18} ions/cm², adapted with permission from [43]. (Left) The bubble size distribution right before blistering was fairly uniform, while (right) the bubble distribution upon blistering was bimodal. (Right inset) Larger faceted cavities were also observed in the blistered sample. Copyright 2018 Elsevier.

2.5.3.2 He blistering in W

Allen et al. observed He blistering in high-purity single crystal W(100) [44, 45]. Samples were made using HIM implantation with beam energy set to 25 keV. The threshold dose for blistering was $\sim 5 \times 10^{17}$ ions/cm², and the blister location was observed at the SRIM-simulated peak concentration of He ions. Scanning Transmission Electron Microscopy (STEM) images from Allen et al. are reproduced in Figure 2.9. A high concentration of small bubbles was observed, as well as the linkage of small bubbles to form nanocracks. Allen et al. concluded these nanocracks caused the eventual blister formation, thereby providing a direct observation of the aforementioned inter-bubble fracture model proposed by Evans [40, 38].

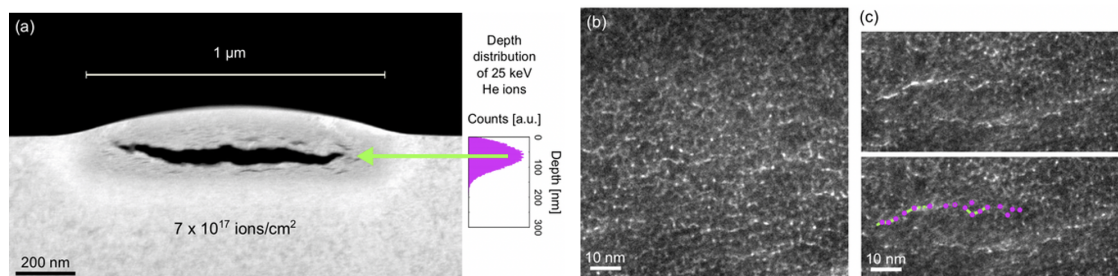


Figure 2.9: STEM micrographs of W(100) implanted with 25 keV He ions at room temperature, adapted with permission from [44]. (a) Cross section of the entire blister profile annotated with the SRIM-calculated range of He ions; the blister crack was observed at the peak He concentration. (b) He bubble distribution shows a network of nm-size bubbles and (c) the linkage of these small bubbles to form nanocracks. Copyright 2020 Elsevier.

2.5.3.3 He blistering in V

Hosemann et al. used a ring-core drilling method to measure the surface stress caused by room temperature He implantation in V [46]. The implantations were performed using a HIM with beam energy set to 25 keV, and blisters were observed around 4.6×10^{17} ions/cm².

Up to 5×10^{16} ions/cm² (before blistering), no measurable residual stress was found, even though surface swelling of up to 6 nm was measured. However, at doses of 1×10^{17} ions/cm² and 4.6×10^{17} ions/cm², leading to 8.5 nm and 38 nm swelling respectively, significant compressive stresses around 300 MPa and 507 MPa were observed. In comparison to bulk V properties (fracture and buckling stress), the residual stress was high enough to allow for material fracture, but orders of magnitude below the stress required for material buckling. This study suggested that He gas pressure is the main driving force of the final blister shape rather than lateral stresses.

2.5.4 Summary of He surface Blistering

The He bubble structures associated with blistering of Cu and W is presented schematically in Figure 2.10 [42, 43, 44, 45]. In both Cu observations from Johnson et al. and Yang et al., He bubbles appear to coalesce randomly as they grow with increasing He dose at some depth from the surface, and eventually bisect to create a large cavity. In the W observation from Allen et al., bubble growth appears to be hindered, and adjacent bubbles link to form microcracks. Presumably, the W blister results from a sufficiently large microcrack, as described in the inter-bubble fracture model from Evans [38, 40]. Lateral stress measurements performed by Hosemann et al. gave insight into the final shape of the blister, showing the lateral stress associated with He-induced swelling is not great enough to cause surface bucking [46]. Moreover, blistering in Cu was observed at 1×10^{18} ions/cm², compared to a lower blister onset dose of 5×10^{17} ions/cm² in W and 4.6×10^{17} ions/cm² in V.

The literature indicates differences in the blister formation mechanism for different metals. TEM and STEM results showed that, depending on the material, bubbles either continue

to grow, or their size is limited by inter-bubble fracture. Evans et al. anticipated there may be conditions where inter-bubble fracture cannot occur. Specifically, at elevated implantation temperatures, the presence of thermal vacancies would keep growing bubbles in equilibrium, and there would be no possibility of interbubble fracture. Instead, Evans et al. predicted the bubbles would coalesce randomly as they grow and either bisect or migrate to the surface. The observations show that even at room-temperature implantations, the conditions for inter-bubble fracture are not satisfied for some materials such as Cu. The experimental results reveal shortcomings of the blistering models, as the measured lateral stress was too small to satisfy the lateral stress model, and the inter-bubble fracture model appeared to apply for W but not Cu. This discrepancy between the blistering appearances is found in this thesis. In addition to identifying this discrepancy, this thesis presents further investigations into material properties relating to the blistering mechanism in Chapter 3.

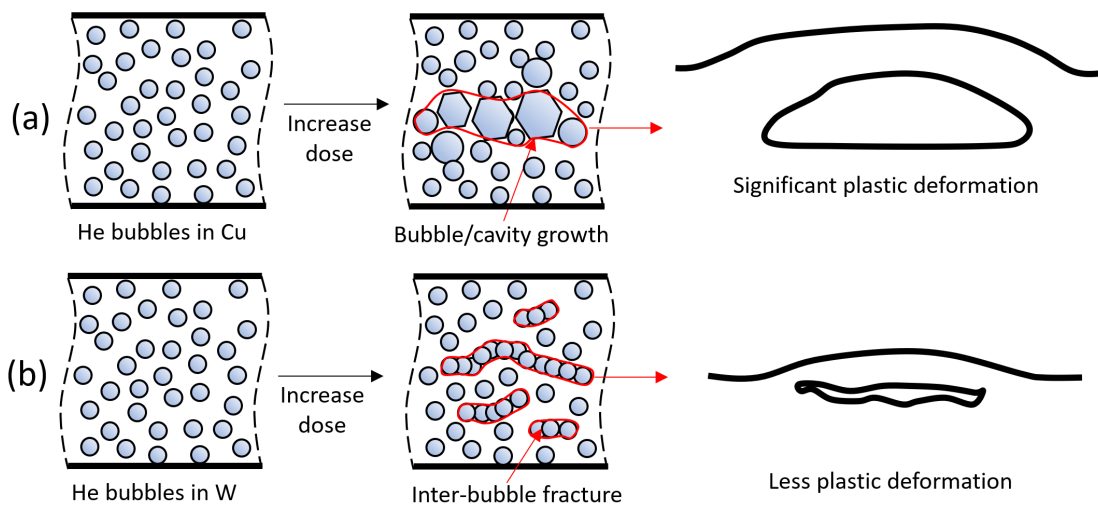


Figure 2.10: Summary of He bubble structures observed in Cu [42, 43] and W [44, 45]. (a) In Cu, He blisters formed due to bubble growth and coalescence, creating large cavities which bisect and dome up to cause significant plastic deformation (large blister cavities). (b) In W, He blisters formed due to crack formation resulting from the linkage of small bubbles, and less plastic deformation (smaller blister cavities) was observed compared to Cu.

2.6 Helium Effects on Mechanical Properties

The introduction of He in metals leads to a change in microstructure and therefore a change in mechanical properties. Numerous investigations of the influence of He on mechanical properties have been carried out over a variety of different materials, test conditions, and length scales. While this section does not provide a comprehensive review of all of these

studies to date, it serves as a discussion of studies relevant to this thesis, especially regarding size effects of mechanical properties.

2.6.1 Bulk materials

Bulk materials refers to test geometry sizes with a sufficient number of grains to reproduce bulk-scale material properties [47]. He embrittlement is a significant concern for bulk material irradiations. A small concentration of He is known to cause significant degradation of material properties, potentially leading to catastrophic failure. This is especially true when considering high temperature irradiations such as those in future advanced reactor environments.

He bubble growth along grain boundaries is widely considered to be the cause of He embrittlement in bulk materials. Due to the high He-grain boundary binding energy, grain boundaries act as sinks for He bubble nucleation, growth, and coalescence [34, 39]. Tensile studies have shown these He bubbles evolve under tensile stress, leading to large cavities along the grain boundaries. This causes inter-granular failure at lower stresses than pure materials. Goods et al. showed that even a small concentration of He in Cu, 2 ppm, can have a profound effect on microstructure and tensile properties [35, 48]. In their study, the Cu was aged in ^3H at 200 °C. As shown in Figure 2.11(a), He bubble coalescence resulted in a series of intergranular cavities along a grain boundary. Corresponding tensile results in Figure 2.11(b) reveal the He exposed Cu had a decrease in ductility, which is indicative of He embrittlement. Cross sections of the fracture area, Figure 2.11(c), show intergranular fracture was the failure mechanism. Embrittlement has also been observed in stainless steel aged in ^3H at ambient temperatures [49]. Since these experiments utilized the “tritium trick,” described in Section 2.3.3. above, i.e. introducing He without doping or displacement damage, He is the main cause of embrittlement.

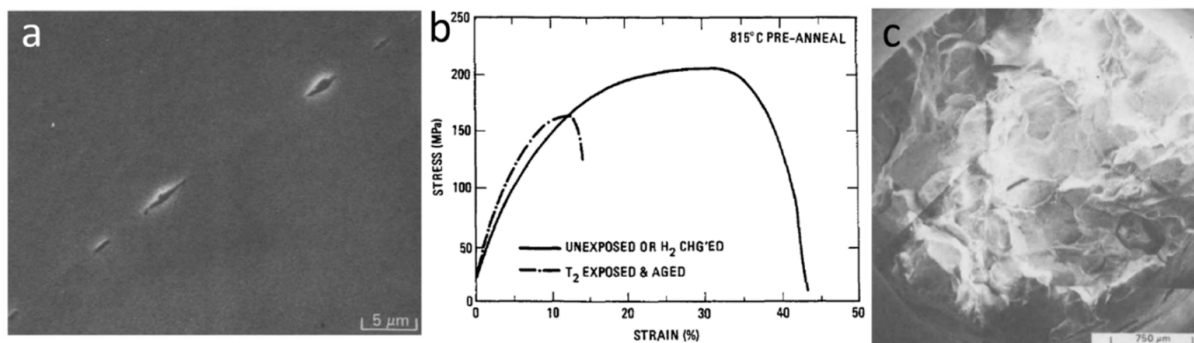


Figure 2.11: Embrittlement observed in Cu into which He was introduced by ^3H decay at 200 °C, reproduced with permission from [35, 48]. (a) Cavities formed along a grain boundary as a result of He bubble coalescence. (b) Tensile testing revealed a decrease in ductility of the He-containing specimens. (c) SEM micrographs of the fracture surface reveal intergranular fracture induced by the He accumulation. Copyright 1986 Elsevier.

In addition to low strain rate ($\sim 10^{-3}$ /sec) tensile testing, He effects on high strain rate ($\sim 10^7$ /sec) deformation has been of recent interest. Combined experimental and molecular-dynamics (MD) studies show that He bubble structures can rearrange within the sample bulk and influence dynamic material properties. Glam et al. experimentally investigated the influence of He bubbles on spall strength [50]. They introduced He in the targets by doping Al with ^{10}B , then irradiating the Al- ^{10}B in a reactor, and finally heating the irradiated Al- ^{10}B to grow He bubbles. Then, shock-wave experiments were conducted by accelerating an Al impactor into different targets: pure Al, Al- ^{10}B , and Al- ^{10}B with He bubbles. They found the Al- ^{10}B had a lower spall strength compared to pure Al. Additionally, the Al- ^{10}B with He bubbles had a higher spall strength compared to not-irradiated Al- ^{10}B . TEM investigations of regions near the spall plane, Figure 2.12, showed the He bubble size increased significantly after shock loading. Additionally, MD investigations of He bubbles in pure Al demonstrated that the presence of He bubbles reduces the spall strength of pure Al [51].

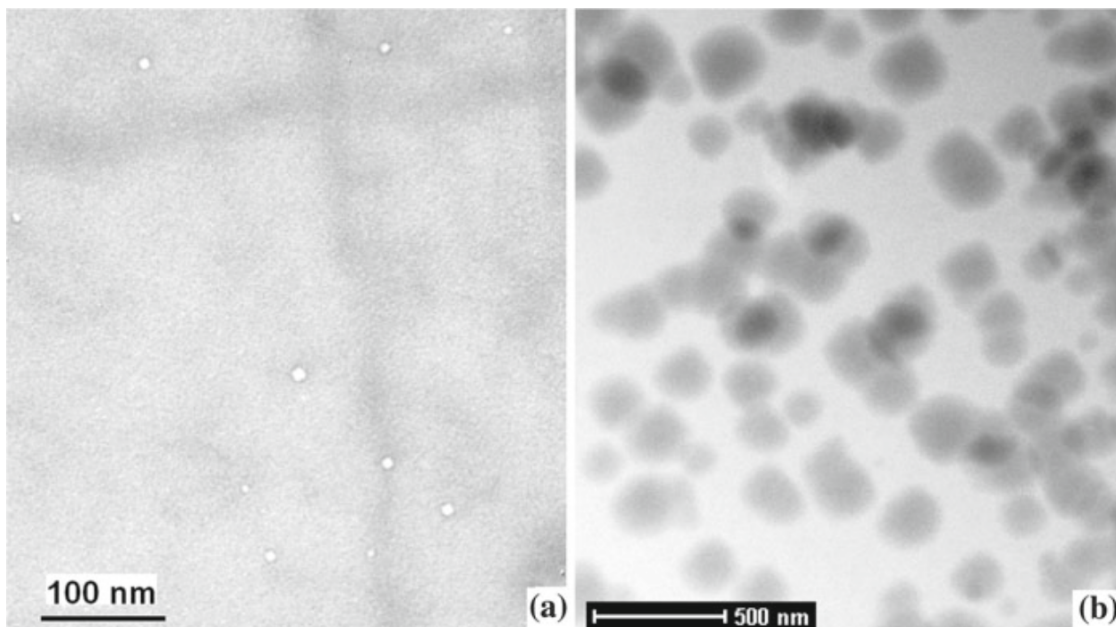


Figure 2.12: TEM of He bubbles in Al- ^{10}B before (a) and after (b) shock loading, reproduced with permission from [50]. The TEM samples were made from a region near the spall plane. The impact caused the He bubble size to grow from approximately 5 nm to 200 nm. Copyright 2010 Springer Nature.

2.6.2 Surface and small-volume materials

Many studies of He effects on mechanical properties are done at surface or small-volume length scales. This is due to the effectiveness of ion implantation in introducing He in materials, making it a widely used technique. In these studies, the maximum penetration depth of He is often 100's of nm to several μm , limited by the ion beam energies available.

As a result, atomic force microscopy (AFM), nanoindentation, and micro-mechanical testing techniques are often used to study property changes in He implanted materials.

AFM has been used to investigate surface swelling in Cu, W, and V [43, 44, 46]. All samples were implanted at room temperature using HIM with a beam energy of 25 keV. As shown in Figure 2.13, swelling increased near-linear with respect to dose in all of these studies; this expected due to cavity (voids, bubbles) formation. The swelling trend for Cu and V appear similar, while W exhibits less swelling at high doses. Additionally, nanoindentation of the He implanted Cu and V revealed the influence of He dose on the hardness and elastic modulus (Figure 2.14). Hardening was observed at doses up to 1×10^{17} ions/cm² in Cu, and the competition of softening occurred at higher doses. In V, hardening was observed up to doses of 2×10^{17} ions/cm², and softening also occurred at higher doses. For both Cu and V, the elastic modulus was observed to decrease with respect to dose.

Ding et al. investigated the compressive and tensile behavior of high-temperature He-implanted single crystal Cu pillars [52]. Micro-compression test results reproduced in Figure 2.15 show the He bubbles enhance slip and plastic flow. During micro-tensile testing, Ding et al. reported He bubble migration, coarsening, elongation, and cleavage under loading. In-situ bending tests coupled with atomistic simulations are shown in Figure 2.16. Both these experiments and simulations showed He bubbles promote dislocation nucleation. Additionally, the He bubbles acted like shearable objects, thereby impeding dislocation motion and reducing the dislocation mean free path, which promotes dislocation storage and leads to strain-hardening, high flow stress, and stable deformation in the small-volume Cu [35, 53, 54]. Thus, in-situ micromechanical testing of high-temperature He implanted Cu nanostructures indicated He bubbles enhance ductility in small volume metals. This is in direct contrast to the decrease in ductility observed in bulk-scale studies, underpinning the need to bridge length scale gaps in nuclear materials testing.

Near-surface He implantation techniques have also been used in shock loading investigations. MD simulations showed near-surface bubbles enhance surface ejecta during shock loading [55]. A corresponding experimental study conducted by Fensin et al. revealed He bubbles in Cu resulted in an increase in the production of finer ejecta traveling at higher velocities and for longer times, suggesting an increase in ejected mass as a function of He concentration [56]. These studies further demonstrate that He bubbles alter important dynamic properties in materials.

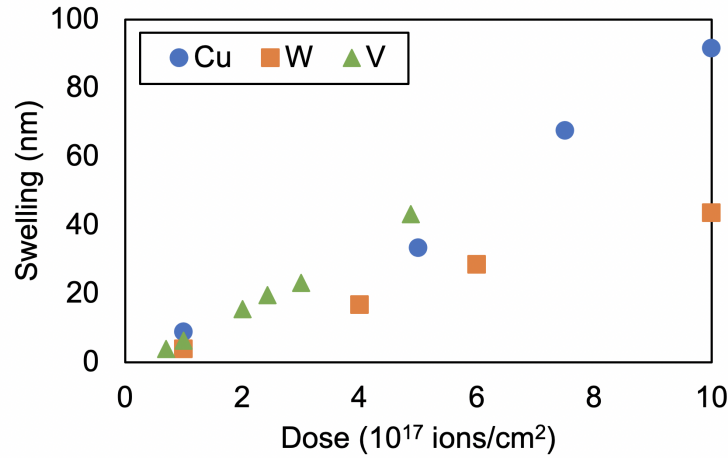


Figure 2.13: Swelling with respect to dose in Cu, W, and V, compiled from [43, 44, 46]. All samples were implanted at room temperature and with 25 keV He ions. For all cases, the relationship between dose and swelling is nearly-linear. Moreover, Cu and V follow a similar trend, while W exhibited less swelling at high doses.

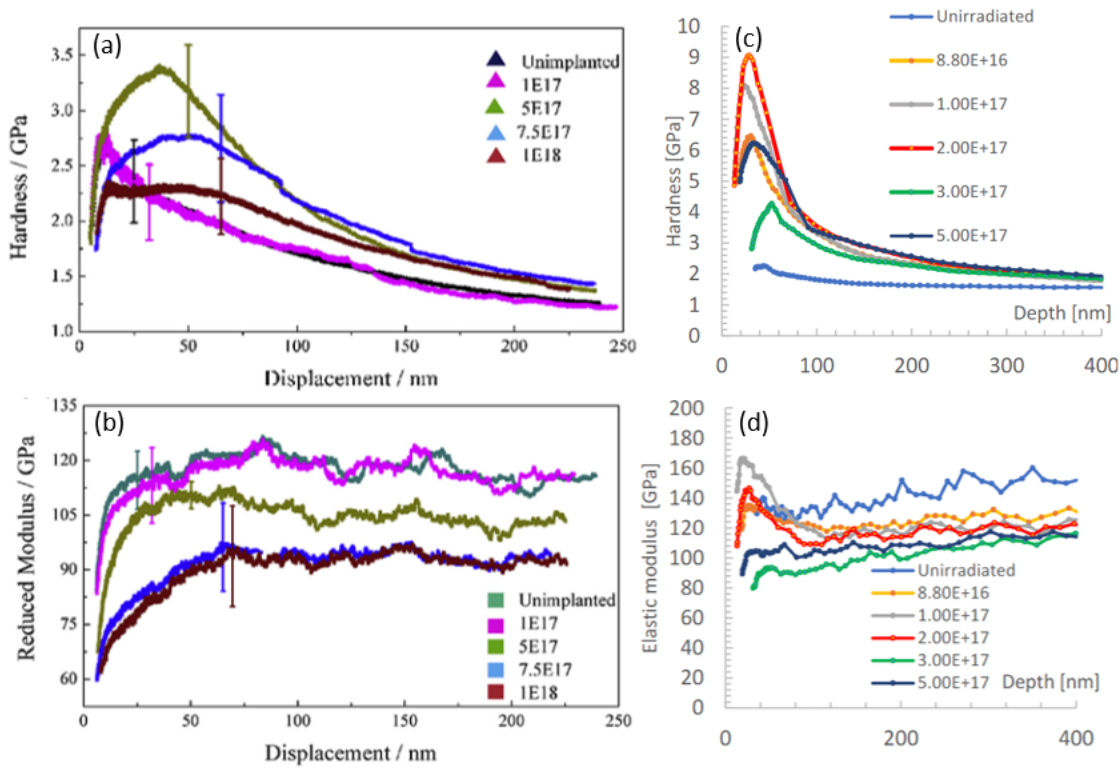


Figure 2.14: Hardness and elastic modulus with respect to dose in Cu (a),(b) and V (c),(d). Both samples were implanted at room temperature and with 25 keV He ions. The results reveal competition between hardening and softening at doses on the order of 10^{17} ions/cm². Additionally, the elastic modulus decreases with respect to dose for both materials. The Cu results are reproduced with permission from [43], Copyright 2018 Elsevier. The V results are reproduced with permission from [46], Copyright 2021 Springer Nature.

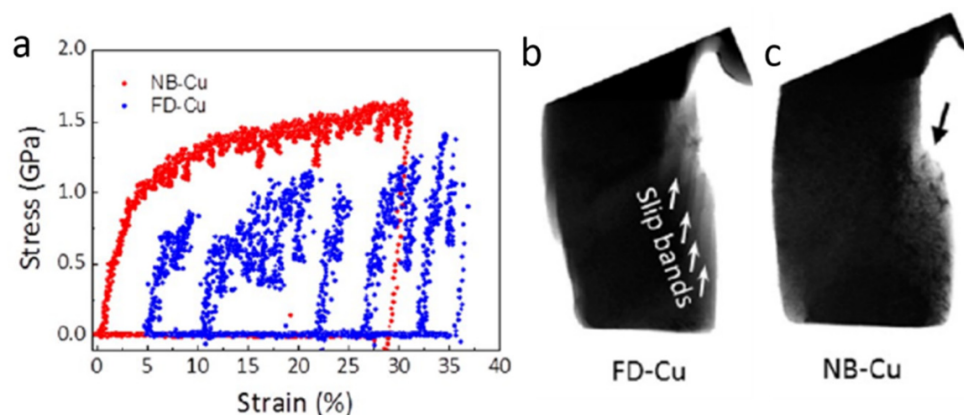


Figure 2.15: Compression testing of Cu nanopillars implanted with He at high temperatures, reproduced with permission from [35, 54]. The He bubbles appear to (a) enhance flow stress and (b) promote dislocation slip. Copyright 2016 American Chemical Society.

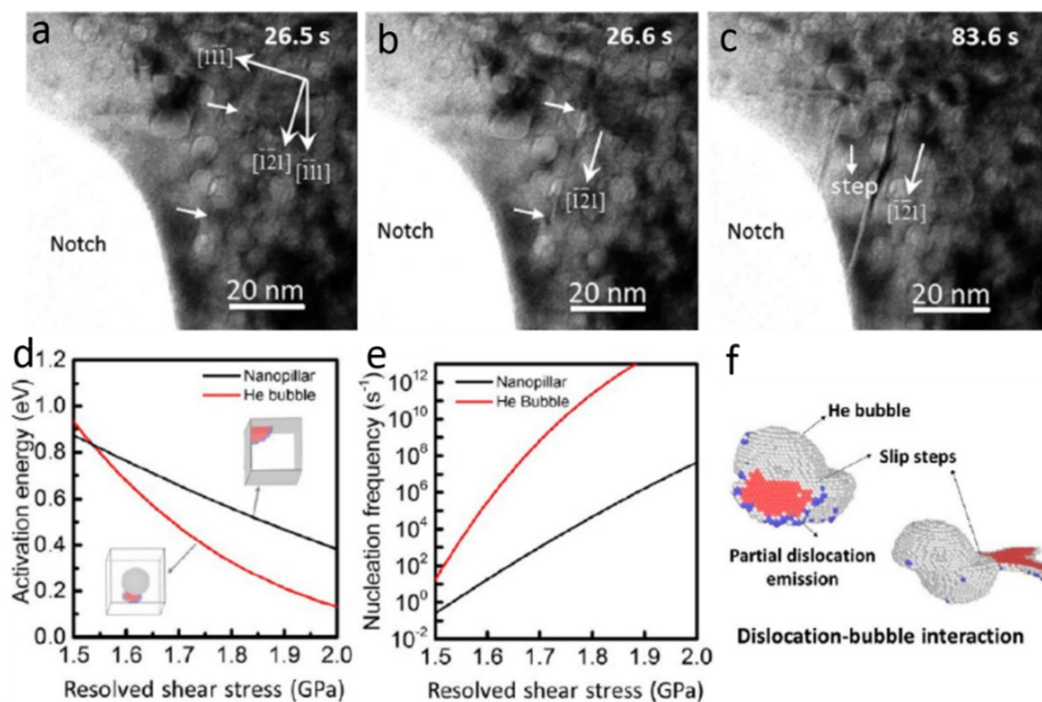


Figure 2.16: (a)-(c) In-situ bending test of small-volume Cu implanted with He at high temperatures, reproduced with permission from [35, 54]. (a),(b) reveal the emission of a partial dislocation from a He bubble, leaving behind a stacking fault as shown in (c). It is worth noting that the He bubbles in these micrographs appear faceted, indicating they are not at equilibrium pressure. This could be due to the high-temperature used during irradiation, which promotes a low He/vac ratio. Atomistic calculations shown in (d)-(f) are also reproduced with permission from [35, 54]. (d),(e) show that bubbles are preferential dislocation nucleation sites compared to the corner of the nanopillar. (f) demonstrates that slip steps on the bubble surface also serve as dislocation nucleation sites. Copyright 2016 American Chemical Society.

Chapter 3

Low Energy Ion Implantation

In this chapter, near-surface structural changes of Ti and Cu upon exposure to He ions are investigated. A combination of implantation and high-resolution imaging and probing techniques are used to gain further insight into the interactions between He ions in the 10's of keV energy range and samples with various material properties. This chapter highlights a novel site-specific implantation technique, Helium Ion Microscopy (HIM), and a novel characterization technique, Positron Annihilation Spectroscopy (PAS).

First, additional background and motivation is provided for these low energy implantation studies. Then, He implantation effects on swelling, hardness, and microstructure is investigated in Ti(0001), followed by comparative studies in Cu(100), Ti(0001), and Ti(101 $\bar{0}$). Lastly, PAS characterization of He implanted and shock loaded commercially pure (cp) Ti is detailed.

3.1 Background and Motivation

The effects of He accumulation in materials are of great interest to the nuclear community since He is produced from (n, α) reactions and radionuclide transmutation (α -decay), and its presence is known to cause microstructural changes and mechanical property degradation. Proper treatment of He-induced property changes requires modelling of all essential processes controlling the microstructural evolution, such as bubble nucleation and growth, as well as the relationship between the evolving microstructure and changes in mechanical properties [39]. Ideas on how to model radiation damage from He accumulation in metals and its effects on mechanical properties originate from experimental evidence. Systematic and highly advanced experiments are required to support the ability to describe these effects analytically.

Most He ion implantations for materials research are conducted at accelerators and plasma devices. Although these machines provide flexibility in the material and sample size to be implanted, experiments can be time consuming and lack control of experimental parameters [44]. He Ion Microscopy (HIM) is a relatively new method of implanting He. The HIM was commercialized in 2007 and is widely used for imaging and nanofabrication

[45, 57]. The HIM functions similar to a Scanning Electron Microscope (SEM), but uses a focused beam of He ions instead of electrons. The He ions are extracted from an atomically sharp needle of three atoms. The needle is held at a high voltage, the He gas flowing over the tip is ionized, and then the ions are extracted to the sample. The incident He ions produce 3-9 secondary electrons per ion, allowing for better contrast and resolution in comparison to SEM, which typically produces one secondary electron per incoming electron [58]. Although the HIM can provide enhanced imaging capabilities, the introduction of high He concentrations in materials can cause unwanted sample modification. Early HIM studies by Livengood et al. in Si and Cu correlated SRIM defect density calculations with Transmission Electron Microscopy (TEM) investigations, revealing the thresholds for various defect structures [59]. As shown in Figure 3.1, He bubbles and larger subsurface voids were observed at doses above 1×10^{17} ions/cm² in Cu and Si.

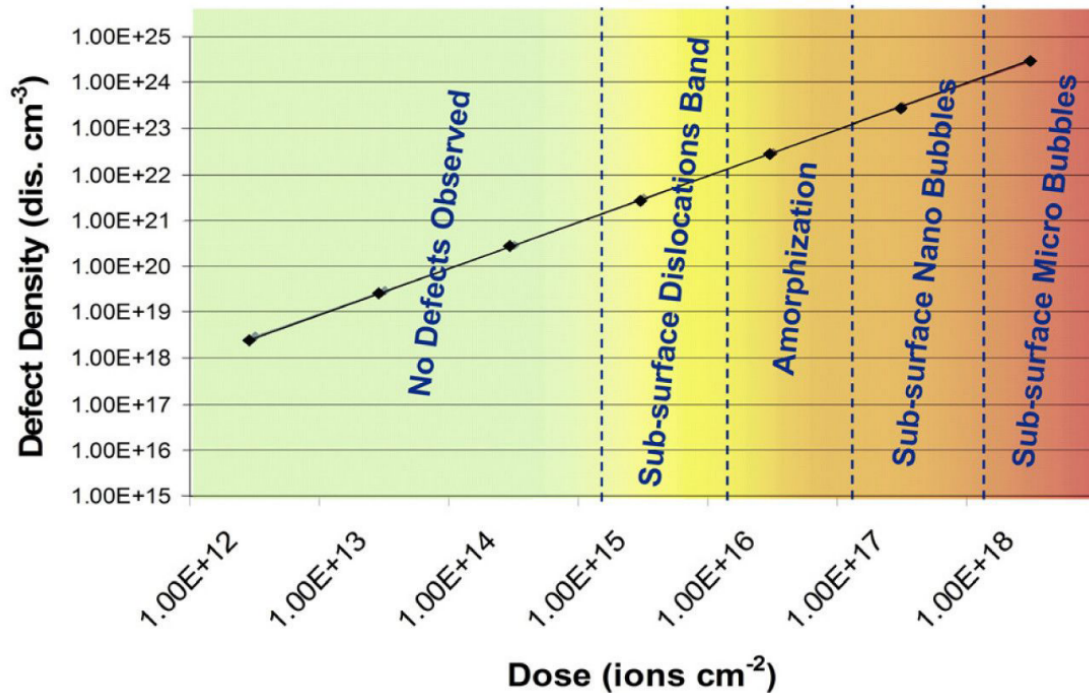


Figure 3.1: HIM implantation dose and resulting SRIM-calculated defect densities and TEM-observed defect structures in Cu and Si, adapted with permission from Livengood et al [45, 59]. He bubbles and blisters were observed at doses above 1×10^{17} ions/cm². Copyright 2009 American Vacuum Society

Recently, the HIM at the California Institute for Quantitative Biosciences at UC Berkeley (QB3-Berkeley) has been used to intentionally produce near-surface He damage and implant He ions in the first 100–300 nm at different doses and dose rates in single crystal and polycrystalline materials [43, 44, 45, 60, 61, 62, 63]. The HIM provides higher throughput and precision in implant dose and location than typical implantation devices, which is conducive for producing systematic He effects experiments.

This chapter focuses on HIM implantation and He blistering studies in Ti (HCP) and Cu (FCC) to investigate the influence of material properties on the development of He bubble structures, especially those relating to blistering. This was largely motivated by the differences in bubble structures observed in Cu and W described in Section 2.5 above [42, 43, 44, 45]. Additionally, the mechanical response of bubble structures and blisters is investigated, largely motivated by the various observations of bubble restructuring under different strain-rate conditions described in Section 2.6 [35, 53, 54, 50, 64]. In this chapter, low strain rate (nanoindentation) studies were conducted on blisters in Ti and Cu, and a preliminary high strain rate (shock loading) experiment was performed on He-implanted Ti.

In addition to using a novel implantation technique of HIM, Positron Annihilation Spectroscopy (PAS), was applied to investigate the evolution of defects as a function of dose and after shock loading. PAS is a powerful technique for the studying small submicroscopic vacancy-type clusters. An overview of how PAS works is presented in Figure 3.2 [65]. Positrons entering a material will thermalize by scattering with electrons, then diffuse through the system until they find a local electron to annihilate with. When a positron annihilates with an electron, it releases two 511 keV gamma photons which can be detected.

Doppler broadening (DB) PAS uses the principle of conservation of momentum. That is, the energy of each annihilation photon should be equal to the rest mass energy of the electron/positron (which is 511 keV) plus or minus an energy, ΔE (the Doppler shift). The gamma photons should be emitted in opposite directions plus or minus an angle, $\Delta\theta$. The energy distribution of the annihilation gammas, i.e. the Doppler shift of the 511 keV annihilation peaks, corresponds to the local defect density.

Another type of positron annihilation spectroscopy is Positron Annihilation Lifetime Spectroscopy (PALS). The thermalization, diffusion, and annihilation of positrons can be inhibited if the positron becomes trapped in a region with less electrons, such as a vacancy, therefore increasing the overall “lifetime” of the positron. That is, the bigger the vacancy, the longer the delay between positron implantation and annihilation. Additionally, the larger the concentration of vacancies, the more 511 keV gammas that will be emitted.

Positrons are sensitive enough to differentiate between 2 single vacancies and 1 divacancy, and can see down to individual monovacancies. This technique has been widely used for the size determination of microvoids and for the study of impurity-void interactions in metals and alloys. The effect of He decoration of voids on positron annihilation characteristics have been studied theoretically and experimentally in metals [66, 67]. In the small cluster regime ($<5 \text{ \AA}$), the positron lifetime is found to be sensitive to the size as well as the He-to-vacancy ratio in the cluster. The development of He bubbles and He bubble structures is tied to the He/vacancy and He/extended defect ratio. The nucleation of He bubbles is tied to availability to vacancies. Thus, the defect specificity of PALS, combined with its sensitivity to He, could be used for a qualitative and quantitative understanding of properties of He bubbles structures and at higher resolution than can be achieved by TEM alone.

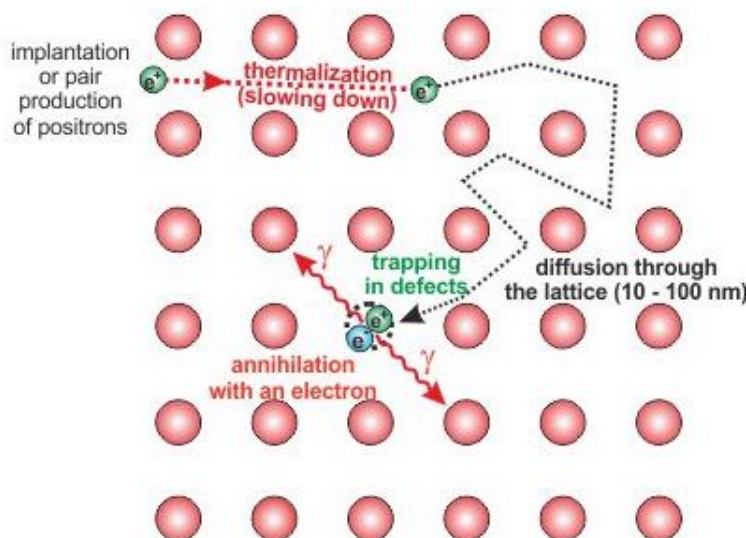


Figure 3.2: The fate of a positron after implantation in a host material. When positrons enter a material, they thermalize, diffuse, and then annihilate with electrons in the material which can result in two 511 keV gamma rays. This process is sensitive to areas with lower electron densities, such as vacancies. The resulting gamma ray spectra can be used to extract information on vacancy size and concentration in materials. Reproduced from [65], copyright 2013 Dr. Maik Butterling.

3.2 Mechanical and Structural Transformation of He Implanted Ti(0001)

This initial study was conducted on Ti(0001), which is the basal plane orientation of an HCP crystal structure. The technique of HIM implantation, followed by AFM, nanoindentation, and microscopy has been previously demonstrated at the University of California, Berkeley on polycrystalline Cu (FCC) and W (BCC) [43, 44, 45]. In general, this study further demonstrates the rapid turnaround capability and repeatability of these experimental techniques, while investigating He effects on a different crystal structure. HCP materials have limited slip systems, and are generally considered brittle at room temperature. These properties may particularly impact He blistering and bubble structures observed at high He doses. More specifically, Ti and Ti-alloys have been considered as structural materials for long-term nuclear waste storage, fusion and gas-cooled fast reactors, and the beam dump at the Facility for Rare Isotope Beams (FRIB) at Michigan State University.

3.2.1 Methods for He Ion Implanted Ti(0001)

Single crystal Ti(0001) with purity of 99.9999%, diameter of 6 mm, and thickness of 1 mm was purchased from Princeton Scientific (Easton, PA). One side of the disk was polished to

roughness $<0.01 \mu\text{m}$. No further treatment was performed before use. The He implantation experiments were carried out at room temperature with a Zeiss ORION NanoFab HIM, capable of imaging with a He source. Implantations were made at 25 keV with varying doses and dose rates. An implant map and description of implant parameters is presented in Figure 3.3.

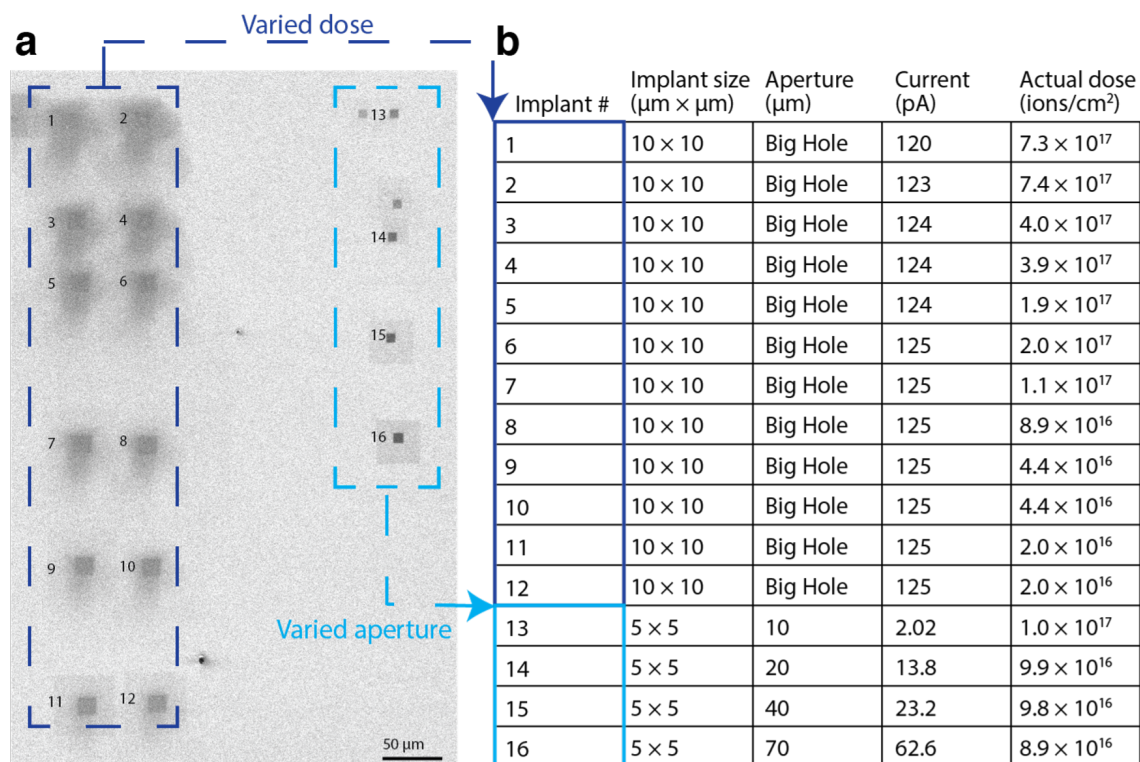


Figure 3.3: (a) Map and (b) corresponding description of parameters for the 16 He implants in the initial Ti(0001) study. The He dose was varied for the first implant set, 1-12. The dose rate was varied for the second set of implants, 13-16.

The SRIM-2013 code was used to simulate the 25 keV He range and damage profiles in Ti, using the method described in Section 2.1. As shown in Figure 3.4, the He concentration peaks around 165 nm with a maximum implantation depth of 329 nm. Figure 3.5 shows the displacement damage peaks around a depth of 122 nm. The peak displacement damage for the $10 \times 10 \mu\text{m}^2$ implants to doses of 7×10^{17} ions/cm², 6×10^{17} ions/cm², 2×10^{17} ions/cm², 1×10^{17} ions/cm², 5×10^{16} ions/cm², and 2×10^{16} ions/cm² was 78 dpa, 44 dpa, 22 dpa, 11 dpa, 5 dpa, and 2 dpa, respectively. For the $5 \times 5 \mu\text{m}^2$ implants to a dose of about 1×10^{17} ions/cm², the peak damage was approximately 3 dpa. It is important to note that the SRIM results, which assume constant bulk density value of the target, become increasingly inaccurate as the dose increases, because the effective density of the target will reduce as He content increases.

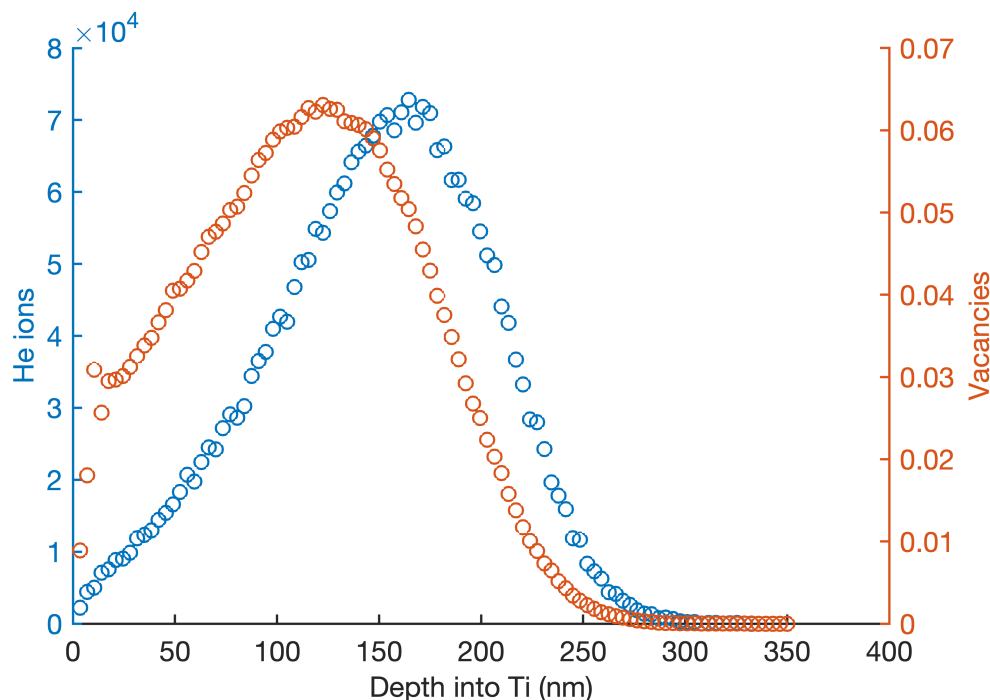


Figure 3.4: He ion and vacancy distributions of 25 keV He in solid Ti calculated by SRIM, assuming constant bulk density of the target. The He concentration peaks around 165 nm, and the max implantation depth is about 329 nm.

Immediately after He implantation, the samples were characterized using a Nano-scope IIIa AFM with sub-nm height resolution to image the topography of implanted surface. Then, hardness measurements of implanted and nonimplanted regions were produced with a Hysitron Triboindenter 950 nanoindenter. Indentations were performed with a Berkovich tip nominal with 40 nm tip radius of curvature. The tip was calibrated using a fused silica as a standard before performing the experiments. The NanoDMA III mode was used to perform Continuous Stiffness Measurements (CSM). The CSM indentation allows for constant hardness and storage modulus evaluation as the indenter is driven into the sample, as opposed to typical quasistatic measurements which measures the hardness and storage modulus at the max indent depth. It is worth noting the storage modulus is an indicator of elasticity taken from the in-phase component of the nanoDMA signal, and is not the same as the Young's modulus which also describes elasticity but comes from the slope of the beginning of a stress-strain curve [68]. Lastly, A TEM foil of a sample cross section was produced using a FEI Helios G4 Focused Ion Beam (FIB) liftout technique.

Figure 3.6 presents the steps of the FIB lift-out technique sequentially. An area with two He blisters was chosen for cross-sectioning, shown in Figure 3.6(a). In Figure 3.6(b), Pt was deposited on this chosen area in order to protect it from the Ga^+ beam during milling. Then, the Ga^+ beam was used to mill trenches on both sides of the sample, followed by a U-shaped volume milled so that only a thin bridge of material kept the sample attached to

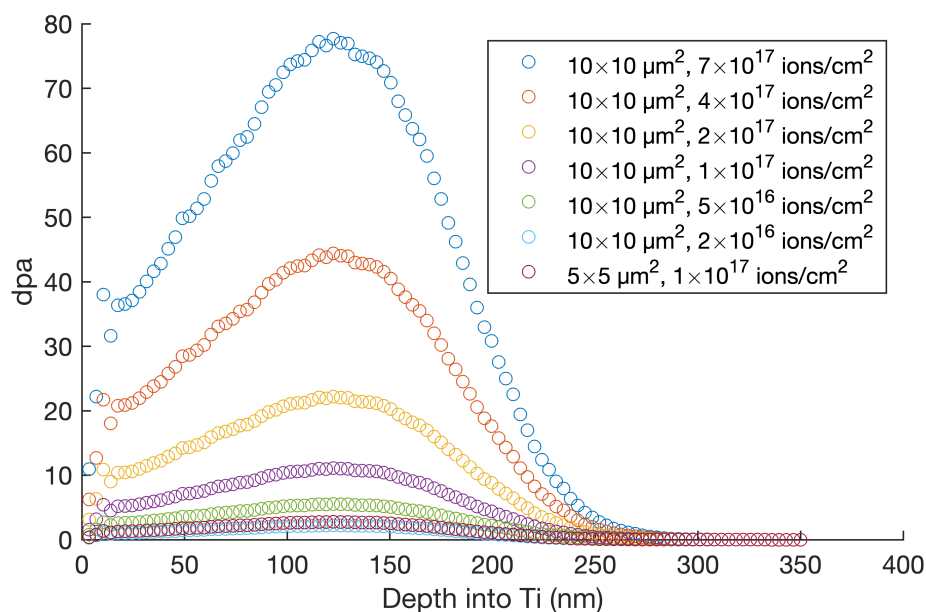


Figure 3.5: Dpa calculated from SRIM simulation of solid Ti subjected to various fluences of 25 keV He ions, assuming constant bulk density of the target. The displacement damage peaks at a depth of about 122 nm. The dpa for the $10 \times 10 \mu\text{m}^2$ implants to various doses range from 78 to 2 dpa. The dpa for the $5 \times 5 \mu\text{m}^2$ implants to a dose of 1×10^{17} ions/cm² was about 3 dpa.

the bulk. The result of these steps is shown in Figure 3.6(c).

After welding the W Omniprobe to the sample with Pt, the small volume keeping the sample attached was milled away. Figure 3.6(d) shows the TEM specimen attached to the Omniprobe as it is pulled away from the bulk. Oxidation on the Cu grid was milled away prior to welding the TEM sample in order to allow for a stronger weld. In Figure 3.6(e), the top right corner of the TEM grid is free of oxidation and the TEM specimen is being lowered to the grid.

Figure 3.6(f) shows the TEM sample welded to the Cu grid with Pt, and in Figure 3.6(g) the Omniprobe was detached from the sample with milling. The edges of the two blisters are visible in Figure 3.6(g), and were opened up as the sample was thinned. The thinning was done so that the maximum size of the blister domes were in cross section and to obtain electron transparency, as shown in Figure 3.6(h). The final TEM specimen thickness, demonstrated by 3.6(i), was about 70 nm. He nanobubbles were observed using the standard Fresnel microscopy method and Joel 3100 and FEI Themis TEMs at the National Center for Electron Microscopy (NCEM) [69].

A summary of the methods is presented visually in Figure 3.7. The nm-size HIM beam enables rapid turnaround He implantation in the keV range with controlled doses and/or dose rates on the same sample. The implants are analyzed by AFM for swelling analyses, indentation for hardness measurements, and TEM for bubble distribution observations.

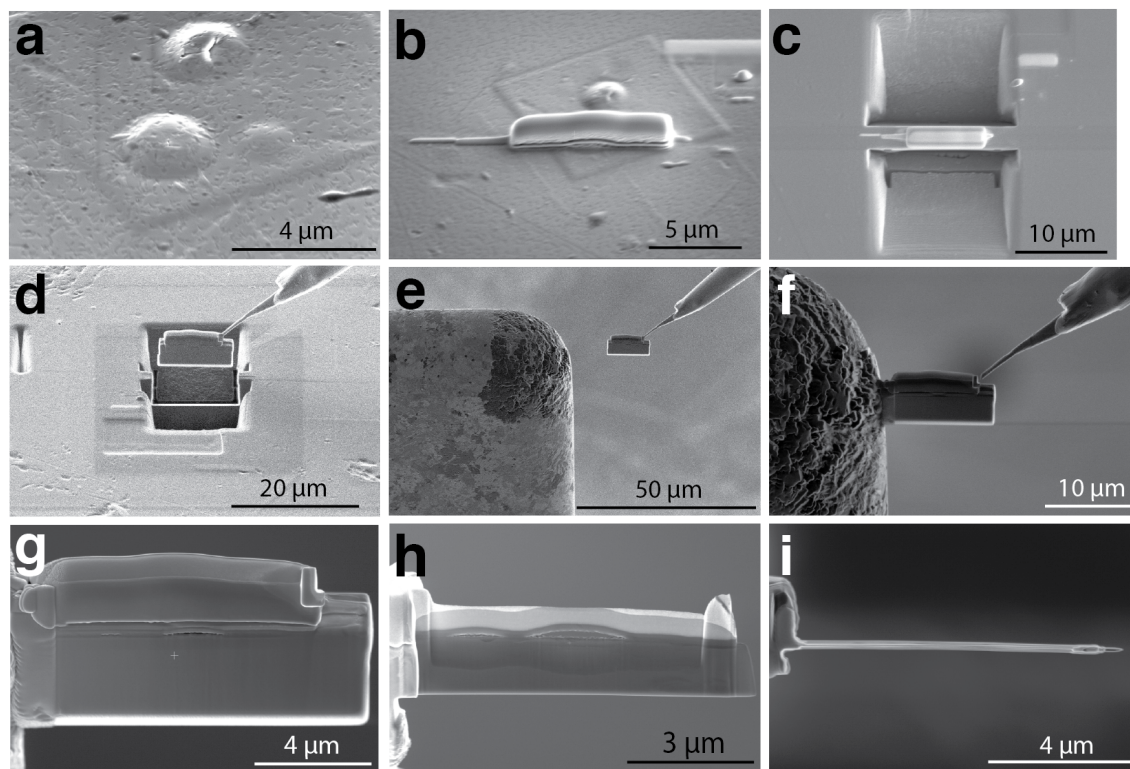


Figure 3.6: FIB technique showing the process of TEM specimen preparation sequentially. (a) SEM image of 3 blisters from 25 keV He implantation in Ti. The implant area was $10 \times 10 \mu\text{m}^2$ and dose was 7.4×10^{17} ions/cm². (b) Pt deposition to protect the two blisters selected for cross-sectioning. (c) Trenches were milled on either side of the two blisters and the U-cut to allow for removal from the bulk material. (d) The Omniprobe was welded to the Pt, and then the bridge of the U-cut was milled. The sample is shown being removed from the bulk. (e) The sample, welded to the Omniprobe, being positioned for welding on the Cu TEM grid. The edge of the Cu grid was milled to assist the welding. (f) After Pt welding the sample to the grid and cutting the Omniprobe from the sample. (g) After some thinning, the beginning of the 2 blister cavities were already visible. (h) SEM image of the two blisters in cross section after final thinning. (i) The final thinness of the TEM sample was around 70 nm.

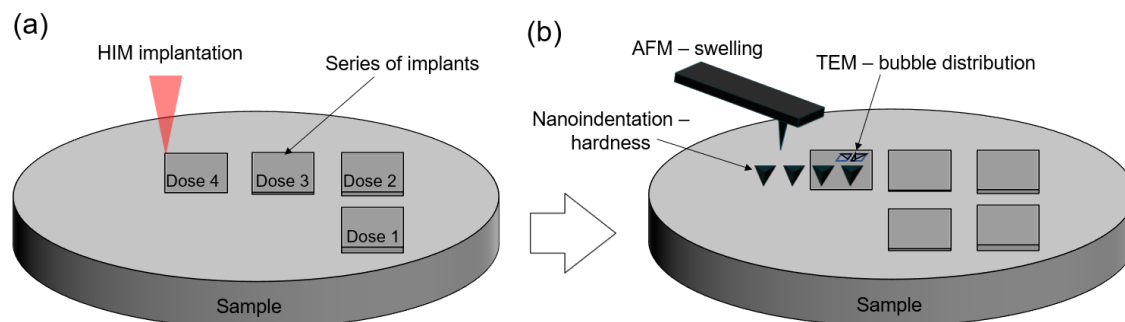


Figure 3.7: Visual summary of the methods used in the initial Ti(0001) studies. (a) Local ion implantations were performed using the HIM, followed by (b) a series of post-implantation characterization techniques.

3.2.2 Results on He Implanted Ti(0001)

For the dose-dependent studies, the cut-off He ion dose was selected by observing the HIM image until two blisters were apparent. For implant 1 described in Figure 3.3, two visible blisters were observed around 6×10^{17} ions/cm². For implant 2 in Figure 3.3, the first visible blister was observed at approximately 5×10^{17} ions/cm², and the second visible blister was observed around 6×10^{17} ions/cm². For the dose rate dependent studies, the target He ion dose was 1×10^{17} ions/cm².

3.2.2.1 Swelling Studies with AFM

The He implantation regions were optically visible and therefore could be located for AFM swelling measurement. The topographic features of each implanted and nearby nonimplanted region were observed by AFM to evaluate variation of swelling and roughness changes due to implantation. The dose and dose rate dependencies of average swelling are summarized in Figure 3.8. As shown in Figure 3.8(a), the dose dependence of swelling appears to be linear. The increase of swelling with increasing dose is expected due to cavities (voids, bubbles) formation. As dose increases, these cavities grow and eventually form larger cavities (blisters) in the material. As the dose rate increases, the sample is exposed to the He ion beam for a shorter period of time. Figure 3.8(b) shows that swelling may decrease with dose rate.

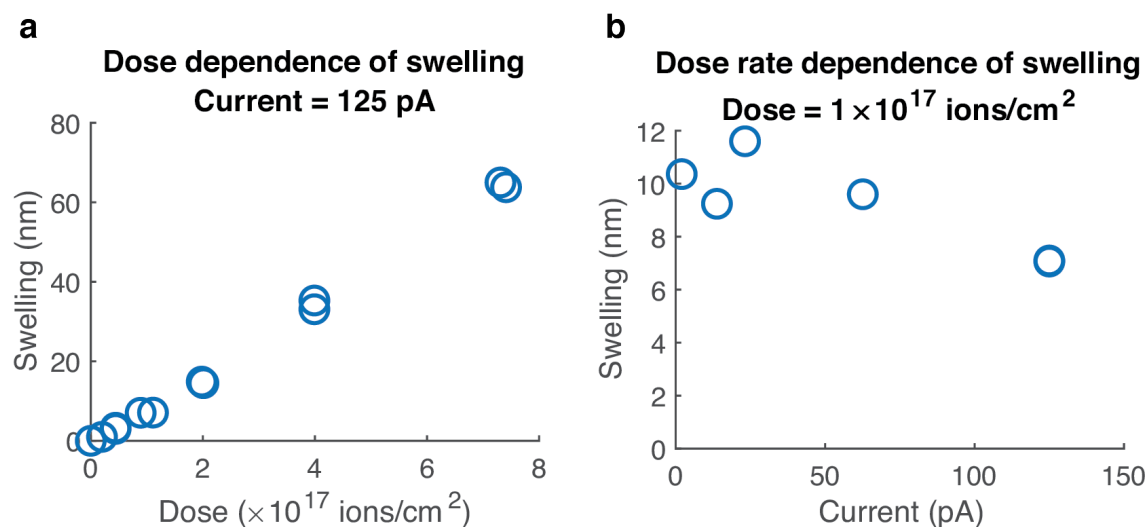


Figure 3.8: Ti(0001) swelling as a function of 25 keV He (a) dose and (b) dose rate, as measured by AFM.

3.2.2.2 Hardness studies with nanoindentation

The AFM on the nanoindenter made it possible to select indents on the implant region and surrounding the implant region. However, the nanoindenter's AFM resolution was not high

enough to be able to distinguish implant regions with <10 nm swelling, so only the $10 \times 10 \mu\text{m}^2$ implants with doses of 7×10^{17} ions/cm², 4×10^{17} ions/cm², and 2×10^{17} ions/cm² could be measured by nanoindentation. 5 indents were performed on each implant region. Additionally, a series of 4 indents were performed on an area far from the implant regions, in order to get a reference nonimplanted hardness value. The average hardness and storage modulus versus indent depth for varying doses is shown in Figure 3.9.

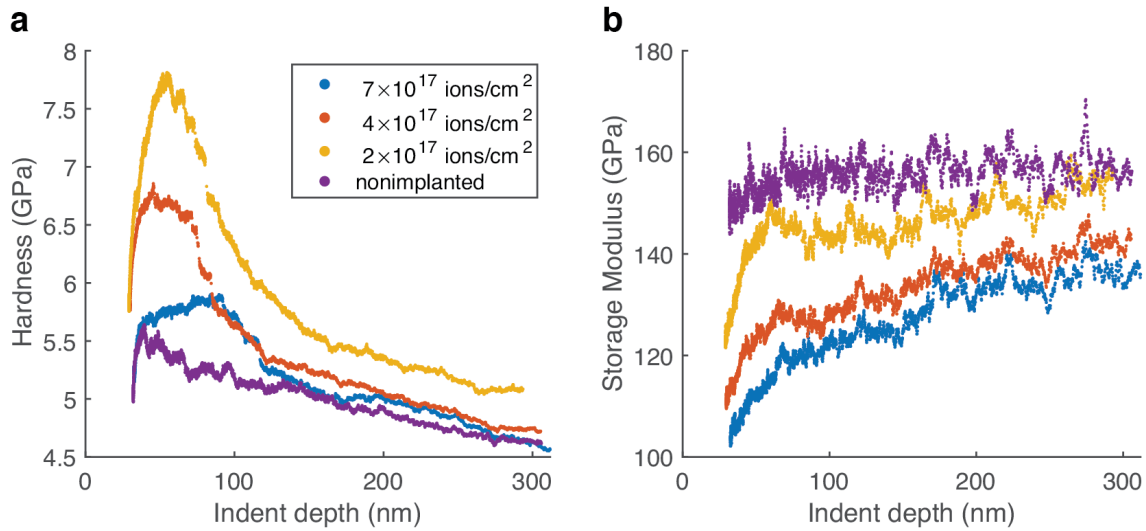


Figure 3.9: Average (a) hardness and (b) storage modulus of implanted and nonimplanted Ti(0001). Both plots share the same legend. (a) The hardness results show a competition between radiation hardening and softening, with an increase in hardness at a dose of 2×10^{17} ions/cm² and then decreasing with doses above 7×10^{17} ions/cm². (b) The storage modulus decreases with increasing He dose.

The curves in Figure 3.9 are an average of 5 indents for the implanted regions, and an average of 4 indents for the nonimplanted region. Figure 3.9(a) reveals that at a depth of 70 nm, the hardness of doses 7×10^{17} ions/cm², 4×10^{17} ions/cm², and 2×10^{17} ions/cm², are about 5.7 GPa, 6.5 GPa, and 7.3 GPa, respectively. These average implanted hardness values are higher than the average nonimplanted hardness, which is around 5.1 GPa at 70 nm depth and in good agreement with the literature [70]. These results show the competition between radiation hardening and density reduction softening. At a dose of 2×10^{17} ions/cm², the radiation defects pin dislocations caused by the mechanical deformation, thereby preventing plastic deformation and increasing the hardness. At 4×10^{17} ions/cm², radiation softening has occurred due to the formation of large cavities. This radiation softening effect is even more dramatic at the dose of 7×10^{17} ions/cm². Figure 3.9(b) shows the storage modulus at 70 nm for the nonimplanted Ti is 157.3 GPa. This is higher than that of the implanted regions, which have a storage modulus at 70 nm of 120 GPa, 127.3 GPa, and 143.7 GPa for the respective doses of 7×10^{17} ions/cm², 4×10^{17} ions/cm², and 2×10^{17} ions/cm².

For both the hardness and storage modulus results, deviations from the nonimplanted region is larger at shallow depths and asymptotically approaches the nonimplanted value as

the depth of indentation increases. This is expected because (1) the range of He in Ti is only 142 nm with a maximum penetration of 329 nm, so after 142 nm the radiation effects are expected to significantly diminish, and (2) shallower indent depth values suffer from surface effects [71].

Another unique deformation phenomena observed during the nanoindentation testing were sudden displacement bursts appearing as a plateau in the loading curve (so-called pop-in) [72]. According to the literature, pop-ins have been observed as a result of phase transformation, fracture with crack initiation and propagation, or homogeneous dislocation nucleation. Generally, the pop-in behavior will be diminished after irradiation because deformation is dominated by irradiation-induced defects hindering dislocation motion. However, the He ion implantation was found to enhance the pop-in behavior of the single crystal Ti(0001). Figure 3.10 shows example loading and hardness curves from each region. These curves are not the average of all indents, but the results from an example individual indent. The pop-in behavior is annotated for the 7×10^{17} , 4×10^{17} , and 2×10^{17} ions/cm² dose region indents, but was not present in the nonimplanted indents and has not been shown in literature of nanoindentation of pristine Ti(0001) [70, 73]. These results indicate that the existence of He bubbles promotes dislocation nucleation.

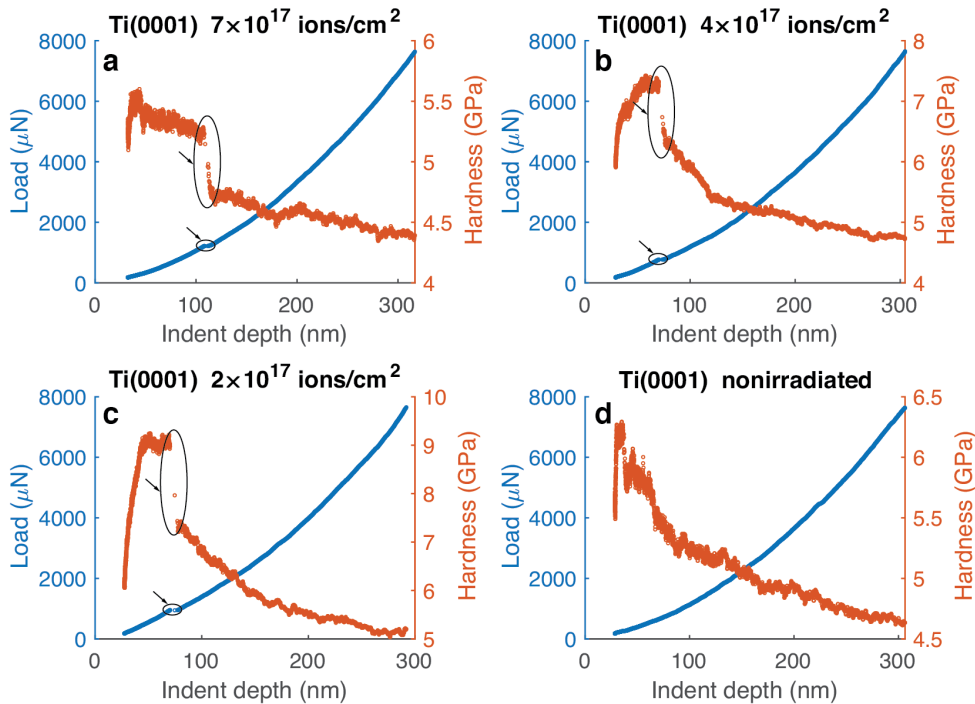


Figure 3.10: Loading and hardness curves from a single indent for (a) 7×10^{17} ions/cm² (b) 4×10^{17} ions/cm² (c) 2×10^{17} ions/cm² and (d) nonirradiated regions of single crystal Ti(0001). For (a)-(c), pop-in behavior is indicated with circles and arrows. No pop-in behavior is observed in (d).

3.2.2.3 Bubble distribution studies with TEM

A TEM sample was produced from implant 2 described in Figure 3.3, which was $10 \times 10 \mu\text{m}^2$ with a He dose of 7×10^{17} ions/cm². Two blisters were captured in cross section for the single foil, as shown in the TEM image in Figure 3.11. The boxes drawn in Figure 3.11(a) show the shell and base regions of the larger blister used to produce the images in Figure 3.11(b). Figure 3.11(b) shows the blister shell (top) and blister base (bottom). The blister cavity occurs around 250 nm, which is significantly deeper than the peak He concentration of 165 nm in bulk density Ti simulated by SRIM and shown to scale in Figure 3.11(c) with the peak depth indicated by an arrow. Qualitatively, it was observed that bubbles near the blister cavity had arranged into nano-crack formations. These nano-cracks were present in both the shell and base of the blister. An example of nano-cracks near the blister are annotated in Figure 3.11(d), which is a magnified section of the blister base in 3.11(b). Some of the bubbles in 3.11(d) are marked with red circles, and their lateral coalescence with green lines.

Figure 3.11(b) was sectioned for bubble counting. The bubble count results are presented in Figure 3.12, which shows the bubble size remains fairly constant throughout the depth of the Ti, ranging from about 1.7 nm to 2 nm. The bubble area ratio is also fairly constant, ranging from about 0.25 to 0.35. The aforementioned nano-crack formations, which appear as the depth into the sample approaches the cavity, were observed to have formed from many small bubbles and with denuded zones surrounding the nano-crack formations. An attempt was made to quantify the bubbles forming the nano-cracks individually versus the nano-crack cavity size in its entirety, which is why the quantified bubble size does not increase with respect to depth in this analysis. It must be noted that there are significant human errors in this type of manual quantification, and several efforts have been made to try to quantify and reduce errors in analyzing small defects in TEM images [74]. Qualitatively, the nano-cracks, and ultimately the blister cavity, were observed to form as a result of lateral coalescence of the nanobubbles, thereby providing direct evidence of the interbubble fracture model [75, 44].

3.2.3 Analysis on He Implanted Ti(0001)

The TEM results were used to calculate swelling based on the nanobubbles observed. To perform this calculation, several assumptions are made: (1) the bubbles are spherical, (2) the bubble size in each box is uniform, (3) The TEM foil thickness is uniform and (4) swelling takes place in one dimension. With these assumptions, the volume ratio, V_{ratio} , of He bubbles to Ti in each rectangle can be calculated as:

$$V_{ratio} = \frac{V_{b,tot}}{(A_r)t} \quad (3.1)$$

Where $V_{(b,tot)}$ is the total volume of bubbles in the rectangle, A_r is the area of the rectangle, and t is the assumed foil thickness of 70 nm. $V_{(b,tot)}$ is calculated for each rectangle

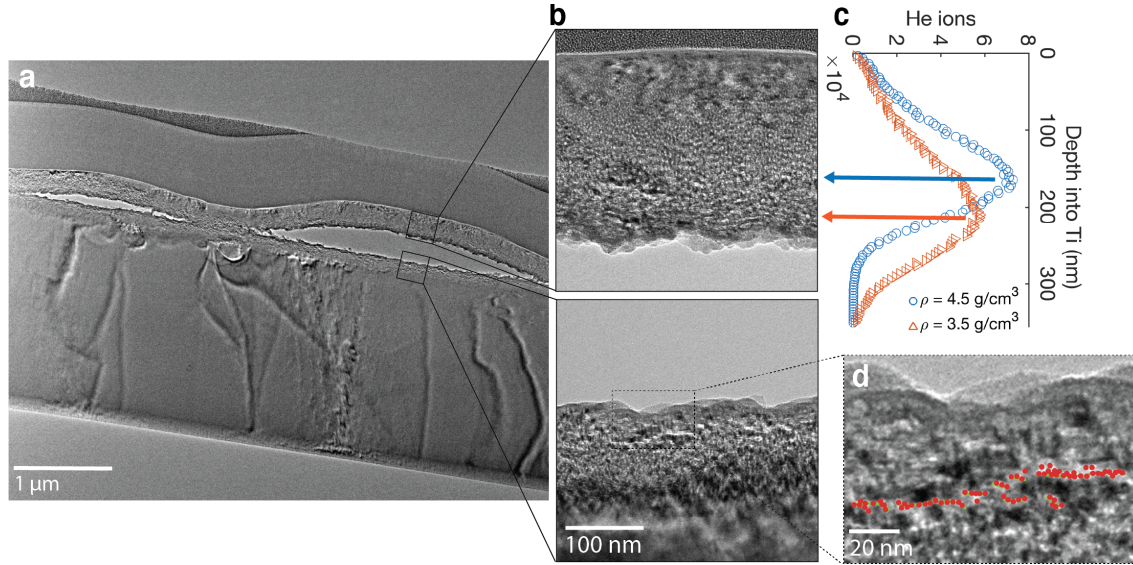


Figure 3.11: TEM results for a cross-section through blisters in the Ti(0001) sample formed by 25 keV He ion implantation to a dose of 7×10^{17} ions/cm². (a) TEM micrograph of the blisters showing a smaller (left) and larger (right) blister cavity. The boxes represent the micrographs shown in (b). (b) -500 nm defocus TEM micrographs of the large blister cavity cap (top) and base (bottom). In this defocus condition, the He bubbles appear as white contrast in the sample. (c) SRIM results of 25 keV He ions in Ti with constant theoretical density and with a reduced density of density of 3.5 g/cm^3 , to scale for comparison with (b). The arrows point to the peak He concentration for each respective simulation. Determination of the reduced density is described in the Analysis section. (d) Duplicate of (b), showing a region of the blister base and near the blister cavity, partially annotated to show nano-crack formation.

by multiplying the average bubble volume in each rectangle by the number of bubbles in each rectangle. The average relative porosity of each rectangle, P , can then be calculated as:

$$P = \frac{V_{ratio}}{1 - V_{ratio}} \quad (3.2)$$

Finally, given the abovementioned assumption that swelling takes place in one dimension, the total swelling can be calculated as the sum of the average relative porosities multiplied by the respective rectangle length (depth into sample), x

$$total\ swelling = \sum Px \quad (3.3)$$

From this calculation, the total average relative porosity was found to be 0.21, and the total swelling was estimated at 63.82 nm. As expected from a similar one dimensional swelling calculation by Yang e.t al, this approximation matched well with the AFM measured swelling, which was 63.8 nm [43].

It was also observed by TEM that the He blister cavity occurred much deeper than the peak He concentration simulated by SRIM. The accuracy of SRIM is expected to diminish as dose increases, because the sample density is changing relative to He content. For these

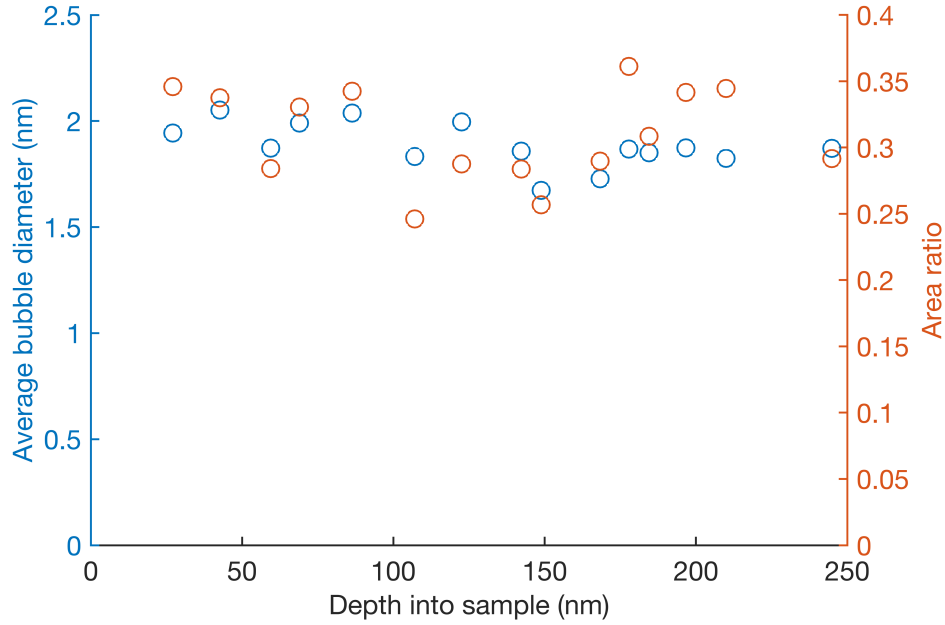


Figure 3.12: Bubble diameter and area ratio as a function of depth for the dose of 7.4×10^{17} ions/cm². As the depth into the samples increases, small bubbles linked to form nanocracks. An attempt was to count these bubbles individually versus quantifying the nanocrack size overall, which is why the average bubble size does not increase with respect to depth into the sample. Additionally, denuded zones appeared to surround the nanocrack, which is why the area ratio was not observed to increase with respect to depth either. It must be noted that significant errors exist with analyzing of small (nm-size) defects in TEM images. Errors were not quantified here, and the TEM resolution limited the ability to quantify all of the bubbles.

reasons, the porosity calculated in Equations 3.1-3.3 was used to calculate a density change as follows:

$$\rho_{new} = (1 - P)\rho_{solid} \quad (3.4)$$

Where ρ_{solid} is the density of Ti before He implantation, and ρ_{new} is the density of Ti after the dose of 7×10^{17} ions/cm². Using a relative porosity of 0.21, the density was estimated to change from 4.5 g/cm³ to 3.5 g/cm³. This density change was implemented in the SRIM simulation, and the result is shown in Figure 3.11(c), next to the blister cap. Figure 3.11(c) shows that even with the change in density, the blister does not occur at the simulated peak concentration of He as expected from previous studies, however it is a closer approximation than the theoretical bulk density [44]. It is worth noting that He channelling is not considered to contribute to the depth of the cavity because channelling is not expected to occur in the (0001) orientation.

3.2.4 Conclusions on He Implanted Ti(0001)

Mechanical and structural changes in Ti(0001) implanted using a HIM with 25 keV He ions were investigated by a series of characterization techniques. Swelling appeared to increase linearly with respect to increasing dose and slightly decrease with respect to increasing dose rate. Radiation hardening was observed at doses of 2×10^{17} ions/cm², and radiation softening was observed at doses of 4×10^{17} ions/cm² and higher. Additionally, He implantation appeared to enhance pop-in behavior of the single crystal Ti(0001), indicating that the existence of He bubbles may change the nucleation behavior of dislocations.

For a blistered implant with a dose of 7.4×10^{17} ions/cm², the He bubble size ranged from about 1.7-2 nm and the bubbles near the cavity coalesced into nanocrack formations. This local accumulation of bubbles is thought to have eventually caused the blister cavity formation. The relative porosity for the Ti implant was approximated to be 0.21, therefore causing the Ti(0001) density to decrease from approximately 4.5 g/cm³ to 3.5 g/cm³. The observed He blister shell was much thicker than the range of 25 keV He ions in Ti simulated by SRIM. This can be explained partially by the decreased density.

3.3 Comparative He Implantation and Characterization of Cu(100), Ti(0001), and Ti(10 $\bar{1}$ 0)

The initial study on Ti(0001) described in Section 3.2 demonstrated the rapid-turnaround and reproducibility of using HIM implantation, followed by AFM, nanoindentation, and microscopy characterization. In this study, Ti(0001), Ti(10 $\bar{1}$ 0), and Cu(100) samples were implanted during the same HIM session. Post-implantation AFM and nanoindentation tests were also completed for all samples in single instrument sessions. The aim of these studies were to investigate He bubble structures associated with blistering in a variety of materials, as well as the He blister response and potential bubble rearrangement or crack growth under mechanical loading.

3.3.1 Methods for the Cu-Ti Comparison Study

The single crystal Ti(0001) and Ti(10 $\bar{1}$ 0) samples were purchased from Princeton Scientific (Easton, PA) and each had a purity of 99.9999 with a diameter of 6 mm and thickness of 1 mm. One side of each Ti disk was polished to roughness <0.01 μm . Ti is HCP, with the (0001) orientation being the basal plane and (10 $\bar{1}$ 0) being the prismatic plane. The single crystal Cu(100) sample was purchased from MTI Corporation (Richmond, CA) with a purity $>99.99\%$ and size of $5 \times 5 \times 1$ mm³. One side of the Cu sample was polished <30 Å. Cu is FCC, with 100 being the surface plane orientation. No further treatment was performed on any of the samples before implantation.

25 keV He implantations were carried out at room temperature with a Zeiss ORION NanoFab HIM. All samples were implanted during the same microscope session and with the same beam energy and current. For all samples, a series of $10 \times 10 \mu\text{m}^2$ implants were produced with doses starting at 1×10^{17} ions/cm² and increasing in increments of 2×10^{17} ions/cm² until the onset of blistering was observed in the HIM image. The blistering onset dose was observed at 5×10^{17} ions/cm², 8×10^{17} ions/cm², and 1×10^{18} ions/cm² for Ti(0001), Ti(10 $\bar{1}$ 0), and Cu(100), respectively. Implant maps with dose parameters are provided in Figure 3.13. The range of 25 keV He and He-induced vacancies in Ti and Cu was calculated using SRIM-2013 and the method described in Section 2.1. Since SRIM does not take crystal orientation into account, the He range profile is assumed the same for both Ti samples, and is shown in Figure 3.4. The He range for Cu is shown in Figure 3.14 below. In Ti, the He concentration peaks around 165 nm, and the max implantation depth is about 329 nm. In Cu, the He concentration peaks around 110 nm, and the max implantation depth is about 255 nm

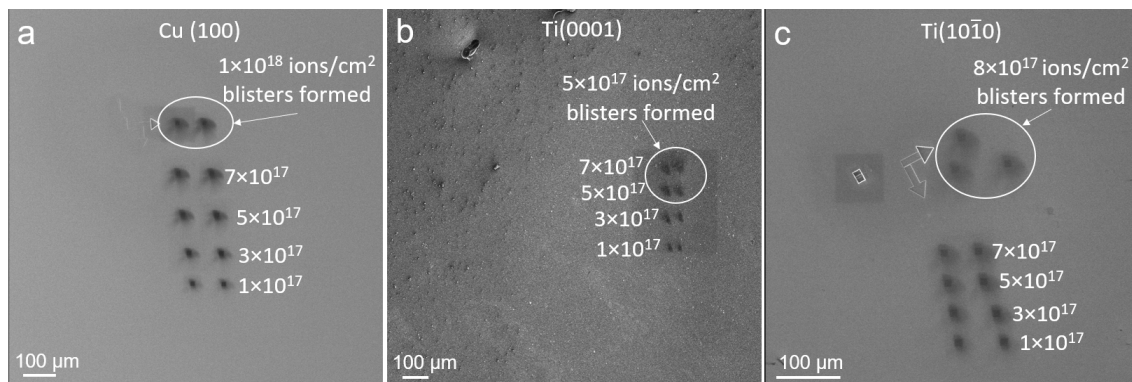


Figure 3.13: HIM implantations and parameters for (a) Cu(100), (b) Ti(0001) and (c) Ti(10 $\bar{1}$ 0).

For all samples, immediately following implantation, the surface topography of the implants were measured using a Nano-scope IIIa AFM with sub-nanometer height resolution. Then, blister indentation studies were performed using a Hysitron Triboindenter 950 nanoindenter with a Berkovich tip nominal with 40 nm tip radius of curvature. A fused silica standard was used to calibrate the tip before performing the experiments. The piezo mode on the nanoindenter was used to measure the surface topography of the implants before indentation. This enabled the selection of the indent directly on the blister. A schematic of the indenter placement is shown in Figure 3.15. Blister indentations were performed using quasi-static measurements with displacement control. A series of indents were conducted at the same position with the displacement increasing by 10 nm until an onset of plastic deformation was observed.

Blisters were cross-sectioned and lifted-out using a Thermo Scientific Scios 2 DualBeam FIB-SEM. For Cu(100), STEM samples were made from a pristine blister and the indented blister. The STEM images were produced using the Scios 2. The Ti cavities and bubbles

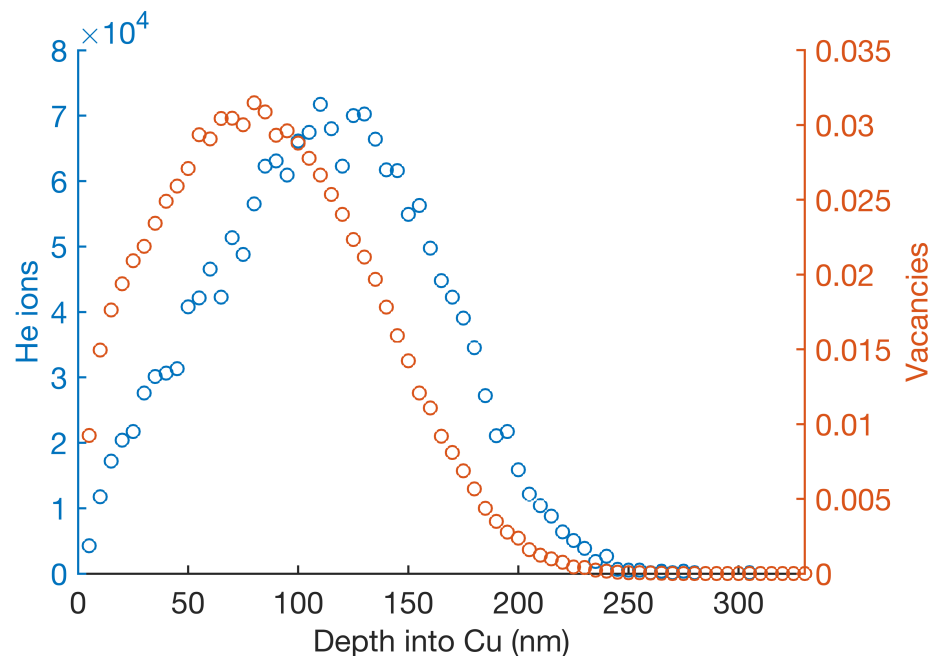


Figure 3.14: He ion and vacancy distributions of 25 keV He in solid Cu calculated by SRIM, assuming constant bulk density of the target. The He concentration peaks around 110 nm, and the max implantation depth is about 255 nm.

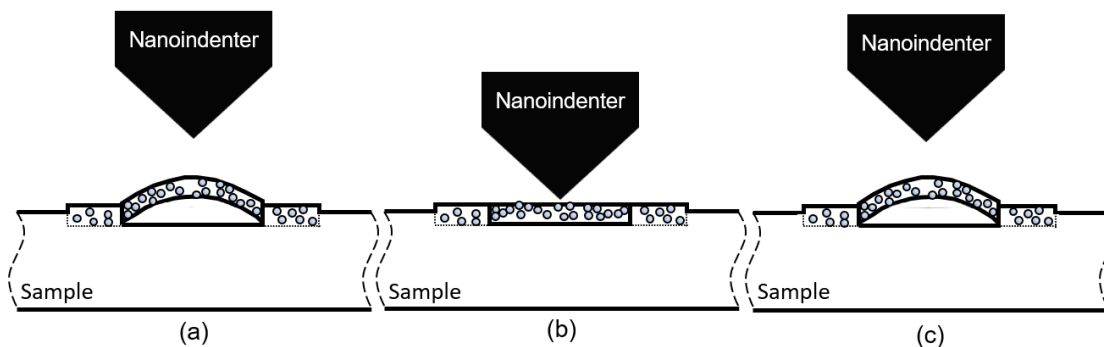


Figure 3.15: Schematic of the placement of the nanoindenter on the blister (a) before, (b) during (assuming maximum displacement), and (c) after each indentation. For simplicity, indentation into the layer is not represented in this diagram, although this would occur at the same time.

were much smaller than that of the Cu, and were not resolved by STEM. For $\text{Ti}(10\bar{1}0)$, a TEM sample was produced from 2 pristine blisters on the sample implant region, comparable to the $\text{Ti}(0001)$ TEM sample presented in Section 3.2. The $\text{Ti}(10\bar{1}0)$ blister sample was top-mounted (as opposed to flag mounted) on the TEM grid and indented in-situ with a Hysitron picoindentation PI95 holder and JEOL 3010. The indentation tip was a conical diamond

tip, with a front face of ~ 5 mm in size. The in-situ indentation was load controlled and concluded when plastic deformation was clearly visible, at 500 μN .

3.3.2 Results on the Cu-Ti Comparison Study

The HIM allowed for direct observation of blister onset, which was observed at 5×10^{17} ions/cm², 8×10^{17} ions/cm², and 1×10^{18} ions/cm² for Ti(0001), Ti(10 $\bar{1}0$), and Cu(100), respectively. All implants were measured by AFM to measure the surface swelling. Then, nanoindentation was performed directly on blisters, followed by microscopy of the associated bubble structures.

3.3.2.1 Swelling Studies with AFM

Swelling versus dose was assessed for the Cu(100), Ti(0001), and Ti(10 $\bar{1}0$) implants. The AFM measurements for these samples were performed immediately following implantation. Swelling results from this study are shown in Figure 3.16, alongside comparable Ti(0001) results from Section 3.2 above and polycrystalline Cu results from Yang et al. [43]. Swelling was observed to increase linearly with respect to dose for all samples. Additionally, there was little deviation in the dose-versus-swelling slope for the different materials.

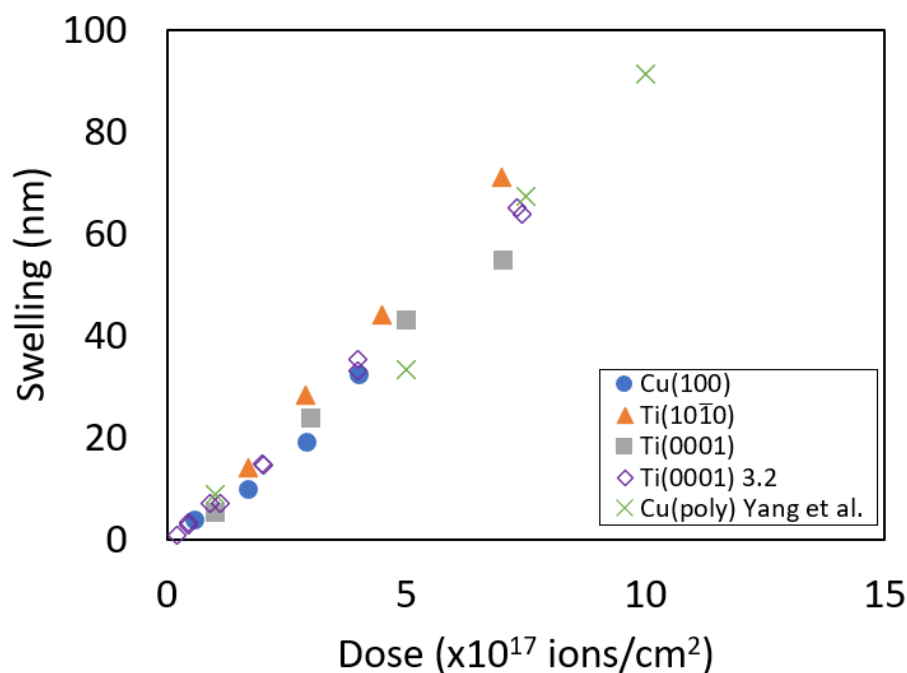


Figure 3.16: Swelling versus dose for Cu(100), Ti(0001), and Ti(10 $\bar{1}0$) measured in this study, as well as the Ti(0001) result from Section 3.2 above polycrystalline Cu result from Yang et al. [43]. For all materials, the swelling increases linearly with respect to dose, and the slope of this relationship is fairly constant across these materials.

3.3.2.2 Blister Nanoindentation Studies

The AFM on the nanoindenter allowed for the placement of the indenter the center of individual blisters. For Cu(100), a 1×10^{17} ions/cm² implant with a single blister was selected for nanoindentation. The indenter was used to push the blister for a series of indents. Each succeeding indent increased in displacement depth by 10 or 20 nm. After each indent, a new AFM image was produced using the nanoindenter, in order to ensure the subsequent indent would be selected on the same location. The load-displacement curves for a Cu(100) blister shown in Figure 3.17 follow the same path for displacement depths up to 160 nm, and therefore the blister behaves elastically. At a displacement depth of 180 nm, a plastic response is observed. This is presumably when the gap in the blister cavity is closed, i.e. when the shell is touching the base and thus the “bulk” is sampled.

The same experiment was performed on single blisters in Ti(0001) and Ti(10 $\bar{1}$ 0). The blister doses were 5×10^{17} ions/cm² and 8×10^{17} ions/cm², respectively. The results shown in Figure 3.18 for Ti(0001) and Figure 3.24 for Ti(10 $\bar{1}$ 0) are significantly different from the Cu(100) result. For both Ti samples, no elastic behavior was observed in the displacement controlled indentation. None of the load-displacement curves followed the same path, and therefore the onset of plastic deformation occurred at blister displacement depths as small as 20 nm. Ti is much more brittle than Cu, and it is possible that a crack may grow when indenting the blister, hence the early onset of plastic deformation. STEM/TEM investigations were conducted to investigate this further.

3.3.2.3 Blister Indentation Microscopy

As shown in Figure 3.13, at least two implants of each dose were produced on the samples. Thus, indented and non-indented blisters from different implants on the same sample were investigated. In Cu(100), the indented blister in the study in Section 3.3.2.1 above was cross-sectioned, as well as a non-indented blister. SEM images of these two blisters before cross-sectioning and lift-out is shown in Figure 3.20. The Cu was not significantly thinned, but since the cavities were so large, the Cu density in the implanted region was very low and thus bubble structures were clearly distinguishable. The STEM images for the not-indented blister is shown in Figure 3.21. The blister cavity is approximately 320 nm in height, and the shell is approximately 160 nm thick. For comparison, the larger blister in the Ti(0001) liftout from Section 3.2 had a blisters with cavity heights of about 52-250 nm and shell thicknesses around 182-238 nm. Additionally, the He bubble formations in Cu are on the order of 10's of nm, which is much larger compared to the ~ 1 nm size bubbles in Ti(0001).

The indented blister liftout is shown Figure 3.21. Like the other Cu(100) blister liftout, this sample was not significantly thinned. The location of the indent is clearly visible and shows the center of the blister was successfully selected during nanoindentation, agreeing well with the AFM result in Figure 3.17(c) and SEM result in Figure 3.20(b). Additionally, faceted cavities are distinguishable, and there are more large cavities and fewer small cavities as opposed to the not-indented Cu(100) blister. It appears there is more bubble coalescence

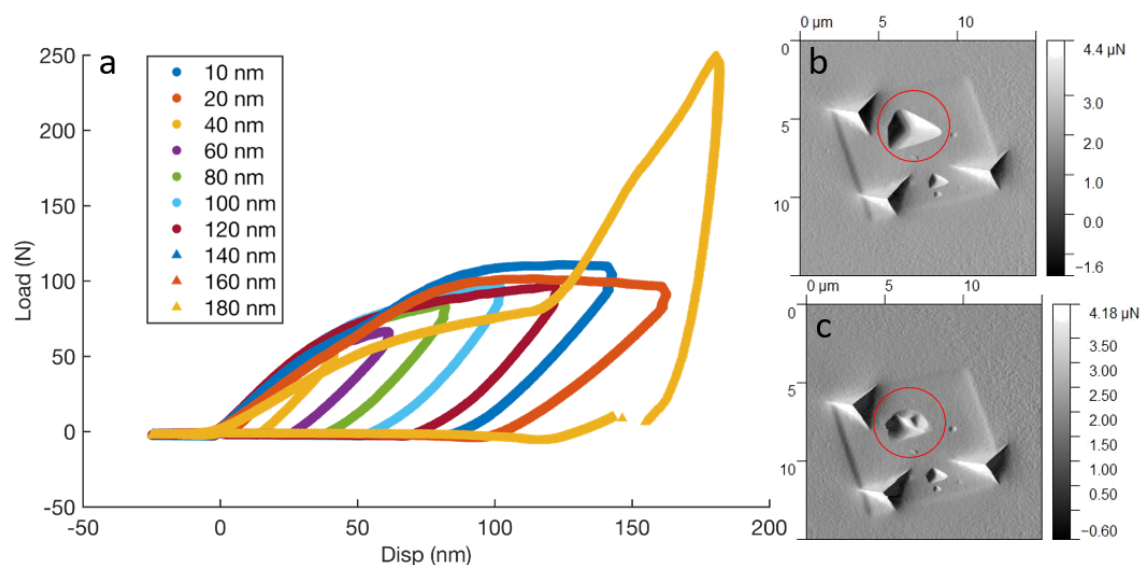


Figure 3.17: Displacement-controlled nanoindentation of a single blister from 1×10^{18} ions/cm² He ions in Cu(100). (a) Load-displacement curves for the series of indents. Up to 180 nm, the load-displacement curves followed the same path, and therefore the blister behaved elastically. Plastic deformation was observed at 180 nm displacement, and the Cu under the blister is presumably sampled. (b) AFM of the implant produced with the AFM on the nanoindenter. The red circle is showing the blister to be indented. (c) AFM of the blister after indentation, produced with the AFM on the nanoindenter.

and corresponding denuded zones in the indented blister as opposed to the not-indented blister, and thus the appearance that nanoindentation caused bubble bubble rearrangement. However, this may be an effect of the thick foils lacking an ability to clearly distinguish the bubble structures.

The He bubble structures in Ti(0001) and Ti(10 $\bar{1}$ 0) were much smaller than that of Cu, and thus thinner foils and TEM imaging was needed to resolve the He bubbles. The attempt to lift-out the indented Ti(10 $\bar{1}$ 0) blister was unsuccessful, so only the not-indented blister was investigated. The foil was top-mounted so the blister could be intended in-situ, in attempt to investigate potential crack growth from the blister cavity. Two blisters were cross-sectioned from an 8×10^{17} ions/cm² implant and thinned to ~ 100 nm. A SEM image of the thinned foil is shown in Figure 3.24. The Ti(10 $\bar{1}$ 0) maximum blister cavity heights were about 191-206 nm tall, and the blister shells were around 100-150 nm thick. The blister shape and bubble size/distribution appeared to be similar to Ti(0001) from Section 3.2, although the Ti(10 $\bar{1}$ 0) blisters were slightly smaller. Since Ti(0001) bubble structures for a non-indented blister were already observed by TEM in Section 3.2 above, no attempts to lift out Ti(0001) blisters were made here.

The picoindenter was centered over one of the blister cavities, as drawn in Figure 3.24(a). Load-controlled picoindentation was performed with a series of seven load conditions on the same location. The load parameter was increased until catastrophic failure was observed.

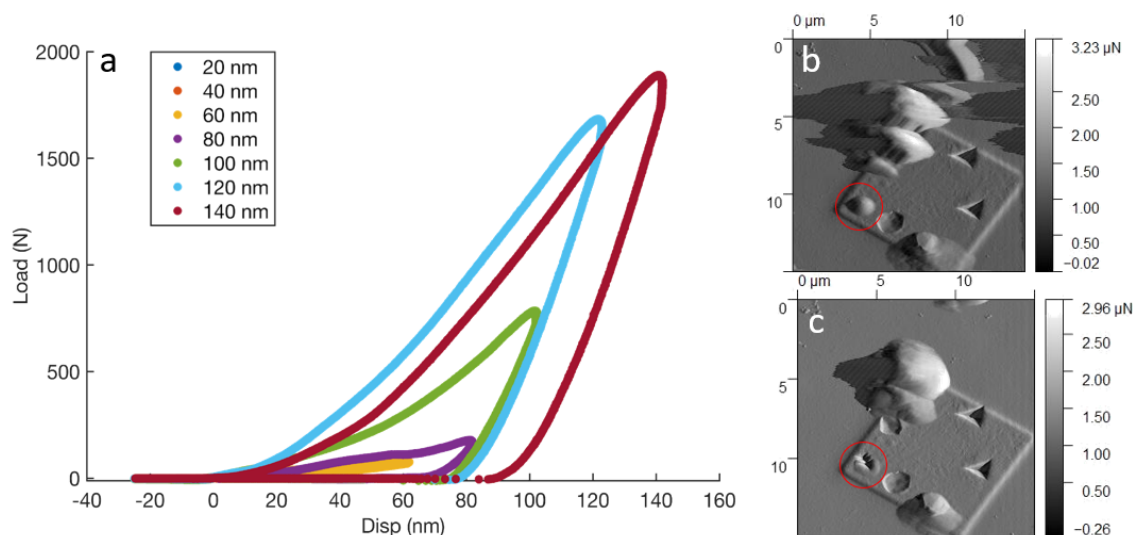


Figure 3.18: Displacement-controlled nanoindentation of a single blister from 5×10^{17} ions/cm² He ions in Ti(0001). (a) Load-displacement curves for the series of indents. Plastic deformation was observed immediately, at 20 nm displacement. (b) AFM of the implant produced with the AFM on the nanoindenter. The red circle is showing the blister to be indented. There was significant noise in the AFM signal, and/or buildup on the indenter tip. (c) AFM of the blister after indentation, produced with the AFM on the nanoindenter.

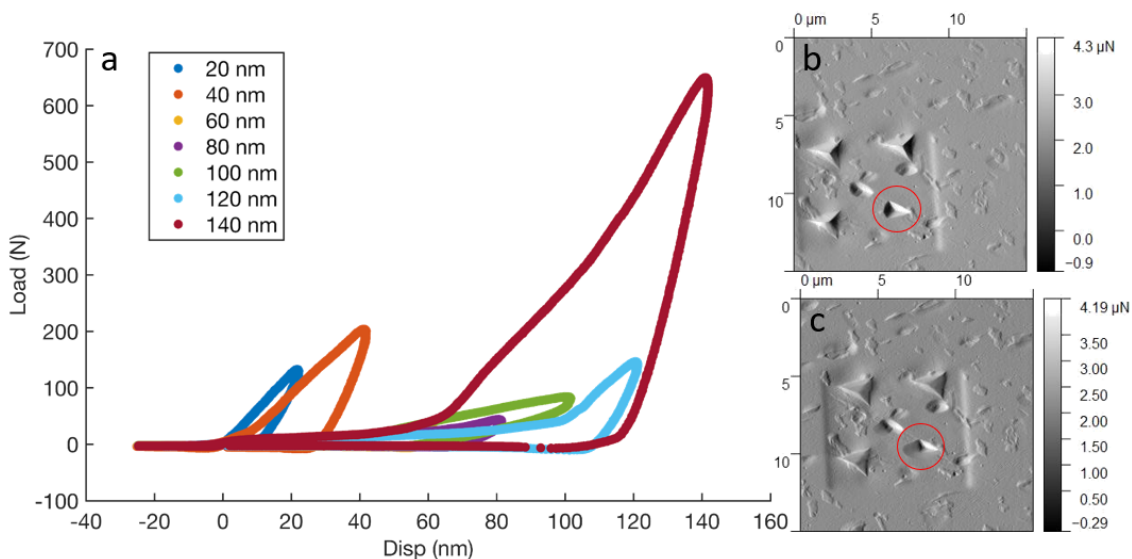


Figure 3.19: Displacement-controlled nanoindentation of a single blister from 8×10^{17} ions/cm² He ions in Ti($10\bar{1}0$). (a) Load-displacement curves for the series of indents. Plastic deformation was observed immediately, at 20 nm displacement. (b) AFM of the implant produced with the AFM on the nanoindenter. The red circle is showing the blister to be indented. (c) AFM of the blister after indentation, produced with the AFM on the nanoindenter.

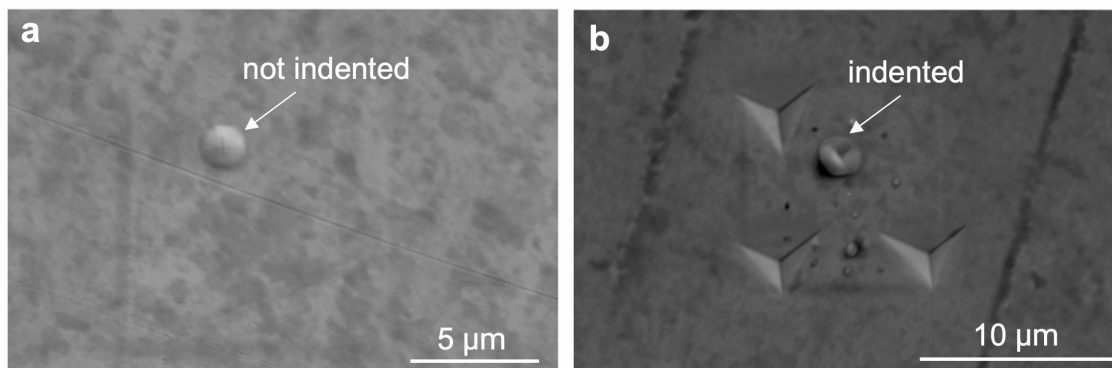


Figure 3.20: SEM images of two $10 \times 10 \mu\text{m}^2$ area and 1×10^{18} ions/cm² dose implants in Cu(100). Both implants had a single large He blister visible. One of the bubbles were indented in the nanoindentation experiment of Section 3.3.2.3 above. The indentation is clearly visible in the center of the blister. Both blisters were cross-sectioned for STEM investigation.

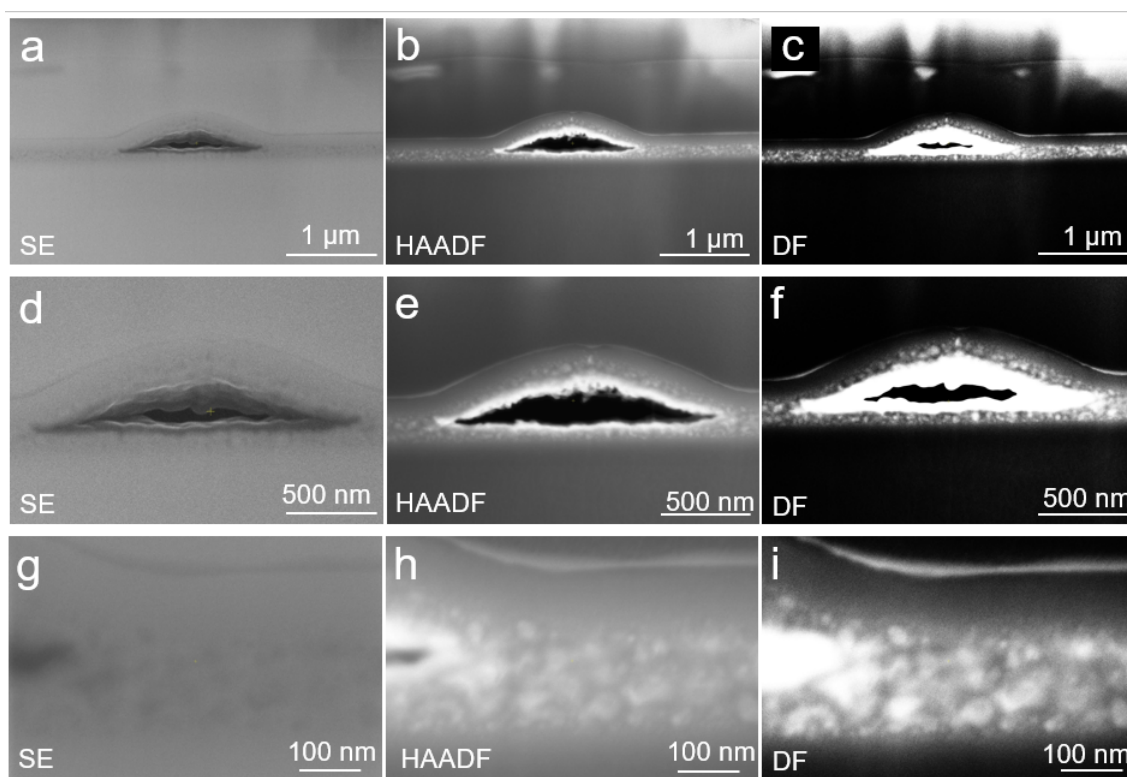


Figure 3.21: STEM micrographs of the not-indented Cu(100) blister, from a dose of 1×10^{18} ions/cm². (a)-(c) Low-magnification secondary electron (SE), high-angle annular dark-field (HAADF), and dark field (DF) images of the blister cavity and surrounding non-blistered implantation regions. (d)-(f) Higher-magnification SE, HAADF, and DF images of the blister cavity. (g)-(i) Higher-magnification SE, HAADF, and DF images of the blister cavity edge.

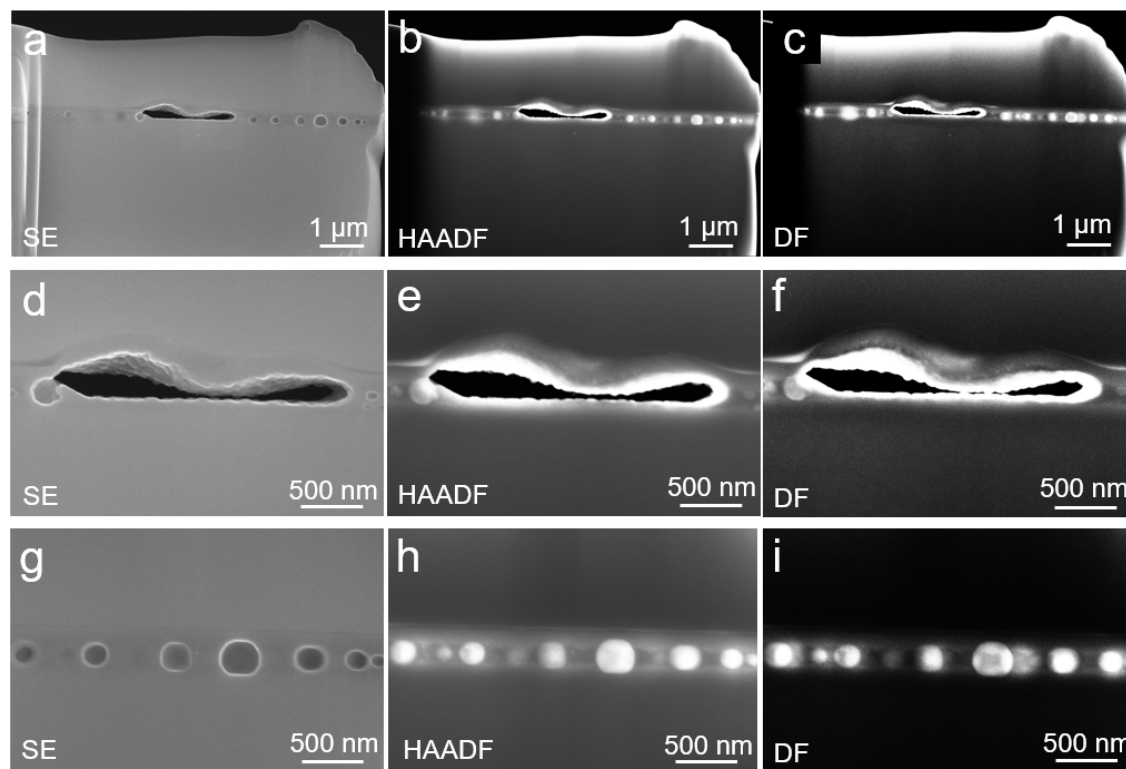


Figure 3.22: STEM micrographs of the indented Cu(100) blister, from a dose of 1×10^{18} ions/cm². (a)-(c) Low-magnification secondary electron (SE), high-angle annular dark-field (HAADF), and dark field (DF) images of the indented blister cavity and surrounding non-blistered implantation regions. (d)-(f) SE, HAADF, and DF images of the indented blister cavity. (d)-(f) Higher-magnification SE, HAADF, and DF images of an implanted region surrounding the indented blister.

The loading sequence was 20, 20, 20, 50, 100, 200, and then 500 μ N. Figure 3.24 shows TEM images of the two blisters after catastrophic failure. Although only one of the blisters was indented, the two blisters interacted and cracked. That is, the area between the blisters acted like a fulcrum, with the indented blister in compression and the adjacent blister in tension. Both blister caps ruptured, and for the adjacent (not-indented) blister, a crack grew from the blister cavity into the sample.

3.3.3 Discussion on the Cu-Ti Comparison Study

There are clear differences between the He bubble structures associated with blistering in Cu and Ti, as well as the response to blister cavities to mechanical loading. In Cu(100), the onset of blistering occurred at higher doses (1×10^{18} ions/cm²) than Ti(0001) (5×10^{17} ions/cm²) and Ti(10 $\bar{1}$ 0) (8×10^{17} ions/cm²). Moreover, the He blister cavity height was the largest for Cu(100) at 320 nm, compared to Ti(0001) at 52-250 nm and Ti(10 $\bar{1}$ 0) at 191-206. The Cu bubble sizes were significantly larger than the ~ 1 nm size bubbles found in the Ti

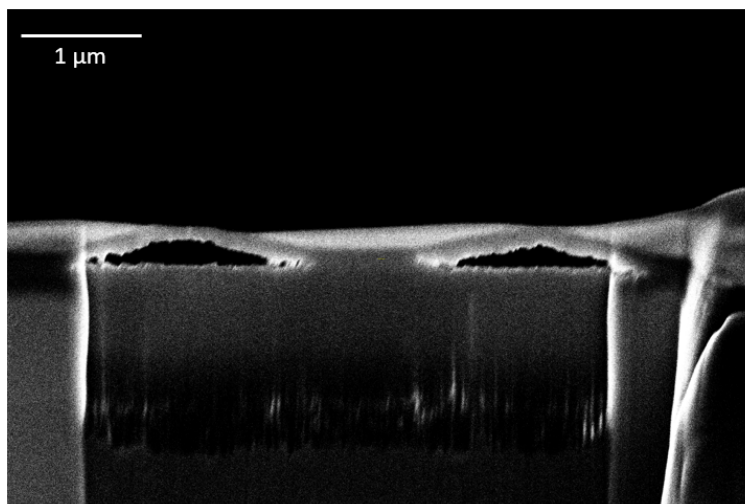


Figure 3.23: SEM micrograph of a liftout of two blisters from an 8×10^{17} ions/cm² implant in Ti(10 $\bar{1}$ 0). The sample was top-mounted to a TEM grid to allow for in-situ picoindentation, and the sample was thinned to ~ 100 nm.

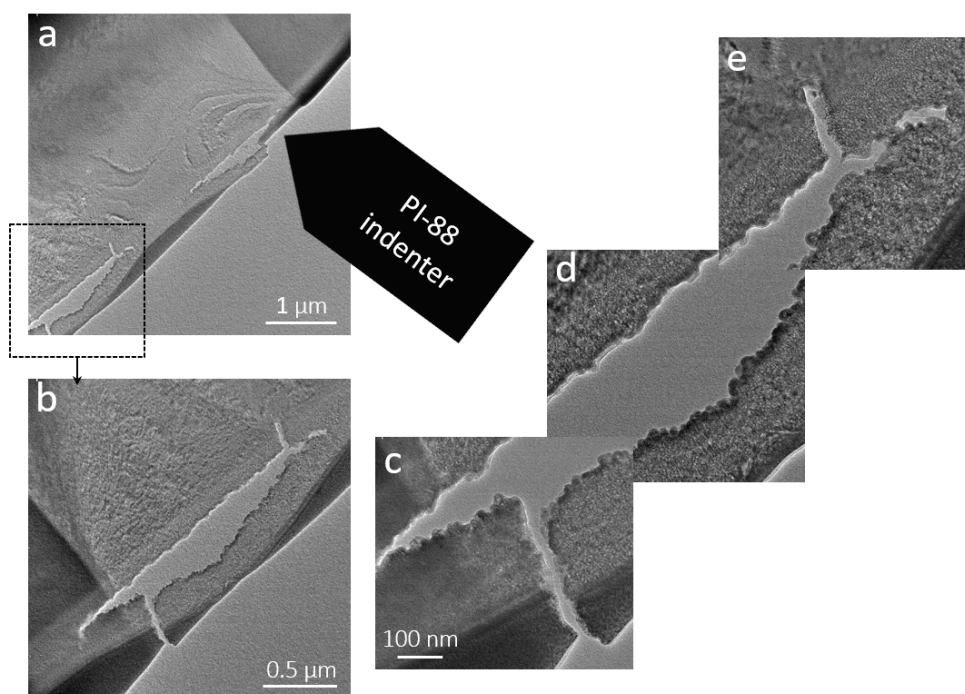


Figure 3.24: TEM micrographs of the 8×10^{17} ions/cm² blisters in Ti(10 $\bar{1}$ 0), after indentation; (a) is in focus, while (b)-(e) are slightly underfocused. (a) Placement of the picointender during the experiment. (b) Close-up of the not-indented blister, which still ruptured and a crack grew into the sample. (c)-(e) Stitched higher-magnification images of the blister shown in (b).

samples, with faceted cavities on the order of 287 nm being resolved in Cu(100). Not only were the bubble and blister structures in Cu and Ti strikingly different, but so was the blister response to mechanical loading. The Cu(100) blister behaved elastically under loading to a limit, while the Ti blisters underwent immediate plastic deformation and potentially cracked under loading.

Cu is FCC and relatively ductile, while Ti is HCP and thus has limited slip at room temperature and is relatively brittle. These properties may explain the differences in bubble structures observed. The ductile Cu can deform to accommodate the growth of large bubble structures during room temperature implantation, whereas the Ti bubble growth is inhibited by inter-bubble fracture and crack growth. Yet, the swelling results appeared to be similar for all materials, indicating that perhaps swelling is purely a function of the amount of He implanted into the samples, whereas the fate of the He is material dependent.

3.3.4 Conclusions on the Cu-Ti Comparison Study

The mechanical and structural changes in Ti(0001), Ti(10 $\bar{1}$ 0), and Cu(100) using a HIM with 25 keV He ions were investigated in a series of comparative studies. Swelling was found to increase linearly with respect to dose for all samples, and the results agreed well with prior HIM implantation and swelling results in Ti(0001) and polycrystalline Cu. The swelling appeared to be dose-dependent and not material-dependent, as the slopes of the dose-versus-swelling curves did not deviate much amongst samples. However, blister nanoindentation and microscopy investigations revealed clear differences between Cu(100) and the Ti samples. The blister indented in Cu(100) responded elastically at displacement depths up to about 160 nm, while the Ti blisters responded plastically almost immediately. STEM and TEM investigations revealed the bubble structures in Cu(100) formed large, faceted cavities and eventually a large blister in comparison to the blister structures in Ti(10 $\bar{1}$ 0) and Ti(0001). In-situ indentation of a Ti(10 $\bar{1}$ 0) blister revealed that two blisters next to each other can interact during picoindentation, and a crack grew from the blister into the sample during indentation.

3.4 Positron Annihilation Spectroscopy and Shock Loading of Helium Ion Implanted cp-Ti

The microscopy results from Section 3.2 and 3.3 above revealed difficulties in quantifying He bubbles by STEM and TEM, especially for small bubbles in Ti and expected from room temperature low-dose implantations. PAS is a powerful technique for the study of small submicroscopic vacancy-type clusters.

Shock loading creates a large number of defects in materials, and shock loading of He-containing materials can restructure the He bubbles in the material [50, 76]. PAS can be used to investigate coupled He surface implantation and shock loading effects. Both PAS and shock loading require broad beam implantation, so the HIM was not used in this study.

3.4.1 Methods for PAS and Shock Loading of He Implanted Ti

Commercially pure (cp-) Ti samples were cut from stock by wire EDM to the dimensions shown in Figure 3.25. This is the sample size required for plate impact experiments. One set of samples were lap-polished to a mirror finish at Los Alamos National Laboratory (LANL). The second sample set was polished at the University of California, Berkeley (UC Berkeley). For the UC Berkeley sample preparation, one side of the samples were polished using 1200 grit SiC abrasive sheet until plane, followed by 9 μm then 3 μm diamond polishing until scratches from previous steps were removed at each step, and lastly 45 min in 0.06 μm vibratory suspension. After polishing, samples were optically inspected to ensure a clean and defect-free surface. An example of the surface quality after polishing is shown in as Figure 3.26. The final thickness of each sample was measured using a micrometer with ± 1 μm tolerance. The thickness was measured 3 times at various points across the sample to ensure the polished face was plane.

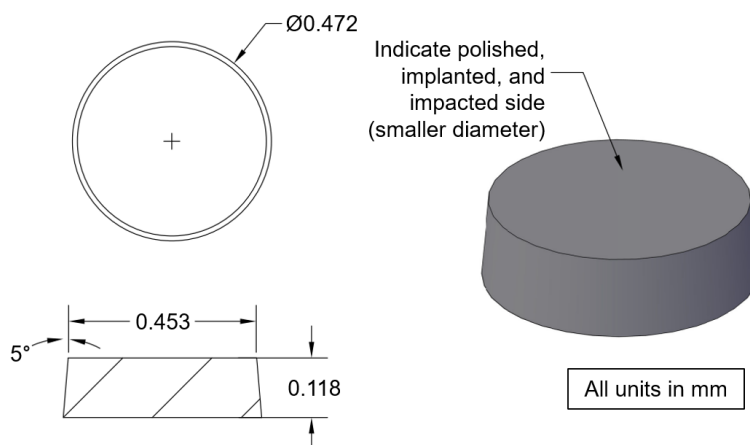


Figure 3.25: Sample dimension requirements for plate impact experiments. The smaller diameter side of the sample was polished, then implanted. For the shock loaded sample, the polished and implanted side was also the impact side.

The polished side of the samples were implanted with 60 keV He ions and active air cooling (< 35 $^{\circ}\text{C}$) using a Danfysik Ion Implanter at LANL's Ion Beam Materials Laboratory. SRIM 2013 was used to calculate the range and vacancy profiles of 60 keV He in Ti, using the method described in Section 2.1. From the SRIM result shown in Figure 3.27, the He concentration peaks around 324 nm with a maximum implantation depth of 522 nm. The set of samples polished by LANL were not masked during implantation. These samples were implanted to 5×10^{17} , 2×10^{17} , and 8×10^{16} ions/ cm^2 at 6h:10m, 2h:40m, and 1h:14m, respectively. One sample was not implanted as a control.

The samples polished at UC Berkeley were masked to implant a 6×6 mm^2 area in the center of the samples. For this set, samples were also implanted to 5×10^{17} , 2×10^{17} , and

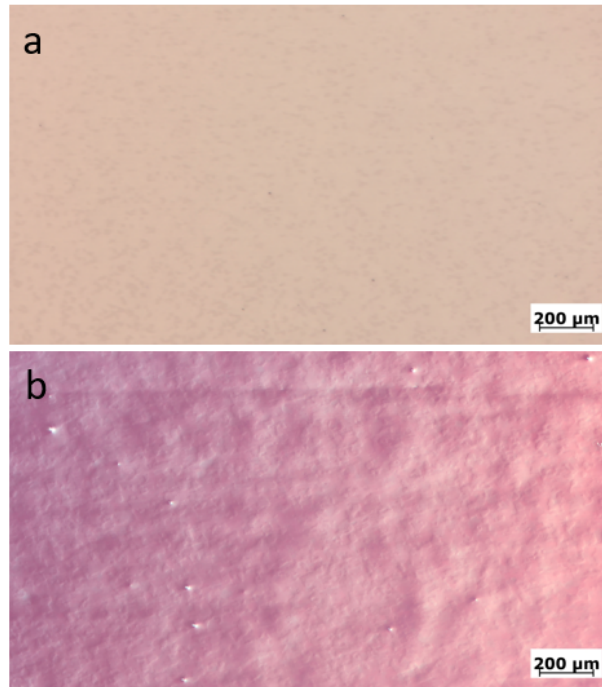


Figure 3.26: (a) Non-polarized and corresponding (b) polarized optical micrographs of an example cp-Ti sample surface after polishing at UC Berkeley.

8×10^{16} ions/cm², but at 7h:56m, 3h:34m, and 1h:55m, respectively. Thus, the current and dose rate for this set was slightly lower. One sample was not implanted for control purposes.

After implantation, the 8×10^{16} ions/cm² sample from the UC Berkeley polished set was shock loaded. The plate-impact experiment was performed using a 19.5 mm gas-gun at LANL. The impactor material was Ti-6Al-4V, and no momentum ring was used during impact. The peak stress was 5-6 GPa to generate early-stage damage. The sample was soft-recovered for post-mortem characterization.

After implantation and/or loading, the samples were sent to the Institute of Radiation Physics at Helmholtz-Zentrum Dresden-Rossendorf (HZDR) for positron annihilation spectroscopy (PAS) to characterize the defect type and density at different depths. The positron beam size is 5-6 mm in diameter, varying slightly depending on the positron implantation energy.

All of the samples were measured by doppler broadening variable energy positron annihilation spectroscopy (DB-VEPAS). The DB-VEPAS measurements were conducted at the apparatus for in-situ defect analysis (AIDA) of the slow positron beamline (SPONSOR) [77, 78]. Positrons were implanted into each sample with discrete kinetic energies in the range between $E_p = 0.05$ -20 keV, which allowed for depth profiling from the surface down to about 1 μ m. Gamma photons resulting from positron annihilation in the material were measured with high-purity Ge detectors with energy resolution of 1.09 ± 0.01 keV at 511 keV. The

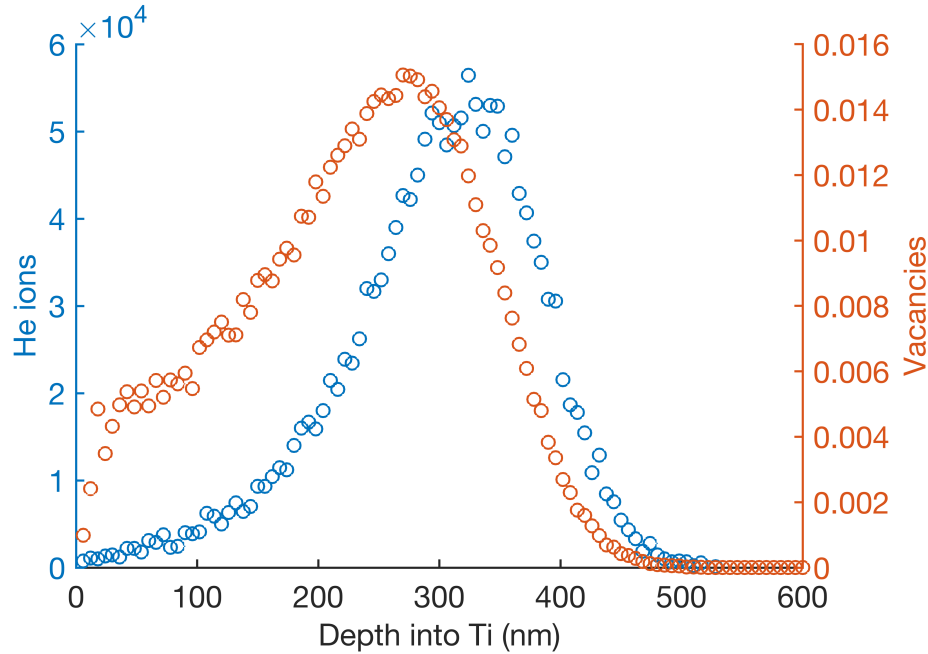


Figure 3.27: He ion and vacancy distributions of 60 keV He in solid Ti calculated by SRIM, assuming constant bulk density of the target. The He concentration peaks around 324 nm, and the max implantation depth is about 522 nm

S-parameter was defined as a fraction of the annihilation line in the middle (511 ± 0.93 keV) region. The S-parameter is a fraction of positrons annihilating with low momentum valence electrons and represents vacancy type defects and their concentration.

Broadening of the 511 keV line is characterized by the S-parameter and W-parameter, defined as a fraction of the annihilation line in the middle (511 ± 0.93 keV) and outer regions (508.33 ± 0.35 keV and 513.67 ± 0.35 keV), respectively. The S-parameter is a fraction of positrons annihilating with low momentum valence electrons and represents vacancy type defects and their concentration. The W-parameter approximates overlap of positron wavefunction with high momentum core electrons. Plotting calculated S as a function of positron implantation energy, $S(E)$, provides depth dependent information, whereas S-W plots are used to examine atomic surrounding of the defect site and its size (type) [79].

Additional variable energy positron annihilation lifetime spectroscopy (VEPALS) measurements were carried out on the LANL-polished sample set. Here, positron energies ranged from 0.5-11 keV, allowing for depth profiling from the surface down to about 350 nm. The VEPALS measurements were conducted at the Mono-energetic Positron Source (MePS) beamline at HZDR, Germany [80]. A digital lifetime CrBr_3 scintillator detector coupled to a Hamamatsu R13089-100 PMT was used for gamma quanta detection [81]. Signal processing was performed with a SPDevices ADQ14DC-2X with 14 bit vertical resolution, 2 GS/s horizontal resolution, and a time resolution function down to about 0.240 ns. The spectrum analysis resolution function uses two Gaussian function with distinct intensities

depending on the positron implantation energy, E_p . All spectra contained at least 10^7 counts. Typical lifetime spectrum $N(t)$ is described by:

$$N(t) = \sum \left(\frac{1}{\tau_i} \right) I_i \exp \left(-\frac{t}{\tau_i} \right) \quad (3.5)$$

where τ_i and I_i are the positron lifetime and intensity of the i -th component, respectively. The sum of the intensities, I_i , must equal one. Using the PALSfit fitting software, all the spectra were deconvoluted into 3 discrete lifetime components, which allow for the quantification of the defect type (size) and concentration [82].

3.4.2 Results on PAS and Shock Loading of He Implanted Ti

For both sample sets, DB-VEPAS measurements were conducted. Additional VEPALS investigations were performed for the LANL polished sample set.

3.4.2.1 DB-VEPAS

Figure 3.28(a) and 3.28(b) show the results from the DB-VEPAS experiment on the LANL polished and UC Berkeley polished sample sets, respectively. Plotting calculated S as a function of positron implantation energy, E_p , provides depth-dependent information. The S-parameter is a fraction of positrons annihilating with low momentum valence electrons and represents vacancy type defects and their concentration. More details on the definition and calculation of the S-parameter can be found in Selim (2021) [83].

For the LANL polished sample set shown in Figure 3.28(a), the pristine (prist) non-implanted sample is presented to give a baseline for the S-parameter of a nearly defect-free material. With increasing implantation dose, the defect concentration and/or size increases. A maximum emerges for 8×10^{16} ions/cm², which extends to a plateau-like region for larger He doses. The expected open volume is the largest for the maximum dose of 5×10^{17} ions/cm².

The pristine non-implanted sample from the UC Berkeley polished sample set shown in 3.28(b) contains less sub-surface defects than the LANL polished pristine sample, since the S parameter at $E_p < 5$ keV exhibits a lower slope. Otherwise, the pristine, 2×10^{17} ions/cm², and 5×10^{17} ions/cm² results look similar to the LANL polished samples. Thus, the shocked and not-shocked 8×10^{16} ions/cm² samples can be compared across sample sets. The shocked sample has a lower defect density compared to the pure 8×10^{16} ions/cm² sample.

3.4.2.2 VEPALS

VEPALS measurements were performed on the the LANL polished sample set to further characterize the defect size in detail. Additional VEPALS beamtime is scheduled at HZDR for the UC Berkeley polished samples, and results are expected in 2023.

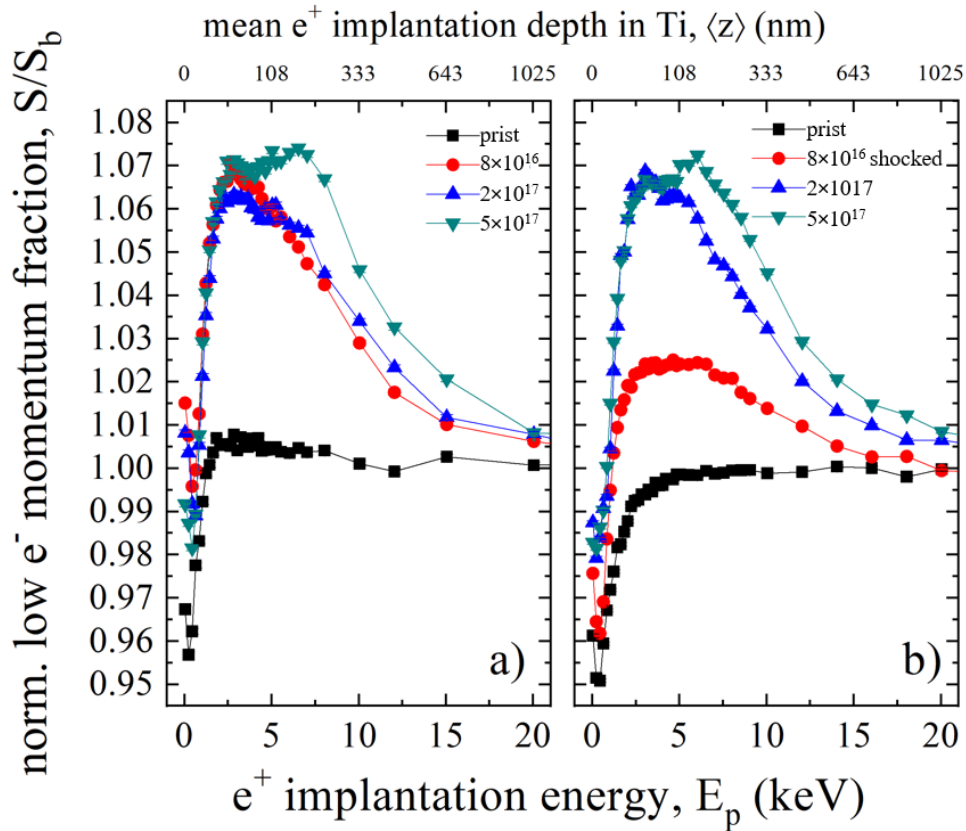


Figure 3.28: DB-VEPAS results from the (a) LANL polished sample set and (b) UC Berkeley polished sample set. The results agree well, with the UC Berkeley set having slightly less surface defects. The S-parameter, and thus the vacancy concentration and/or size, increases with respect to dose. Additionally, this increase is observed at increasing depths into the samples with increasing dose, therefore confirming swelling results. The shocked 8×10^{16} ions/cm² sample showed a decrease in vacancy defects compared to the not-shocked 8×10^{16} ions/cm² sample.

The VEPALS results for the LANL polished samples are shown in Figure 3.29. τ_{av} is the average lifetime, defined as:

$$\tau_{av} = \sum_i \tau_i I_i \quad (3.6)$$

τ_{av} has a high sensitivity to the defect size (type). The τ_{av} result in 3.29(a) illustrates the changes observed by the S-parameter in 3.28(a). That is, both are dominated by variation of defect size and less by defect density. For the maximum dose of 5×10^{17} ions/cm², both τ_{av} and S-parameter results show a maximum at $E_p \approx 7$ keV. Additionally, the weighted average defect size increases with respect to dose.

The lifetime components are shown in 3.29(b). The first lifetime component, τ_1 , for the pristine sample is in the range reported for monovacancy [84]. The second lifetime component, τ_2 , is residual ($I_2 < 1\%$) and likely originates from grain boundaries. The

irradiated samples exhibit the ion damage profile in case of both τ_i . The shorter lifetime τ_1 is in the range reported for a vacancy agglomeration consisting of 3 vacancies for 8×10^{16} ions/cm², and 4 vacancies for 5×10^{17} ions/cm² [84]. On the other hand, the longer lifetime τ_2 indicates generation of large vacancy agglomerations where >50 vacancies (within a spherical cluster) are expected for 8×10^{16} or even small spherical voids of about 0.28 nm in diameter for 2×10^{17} (calculated using [85]). For the maximum dose, the vacancy agglomerations shrink, but their size is still >50 vacancies within a cluster. The absolute number of vacancies within a cluster depends on the correlation method. Additional analysis is needed for the spectra shown.

The relative intensity, I_1 of the defect cluster lifetime τ_1 is shown in 3.29(c). This shows that the density of the vacancy agglomeration increases with the ion dose. The damage profile is visible in the intensity as well.

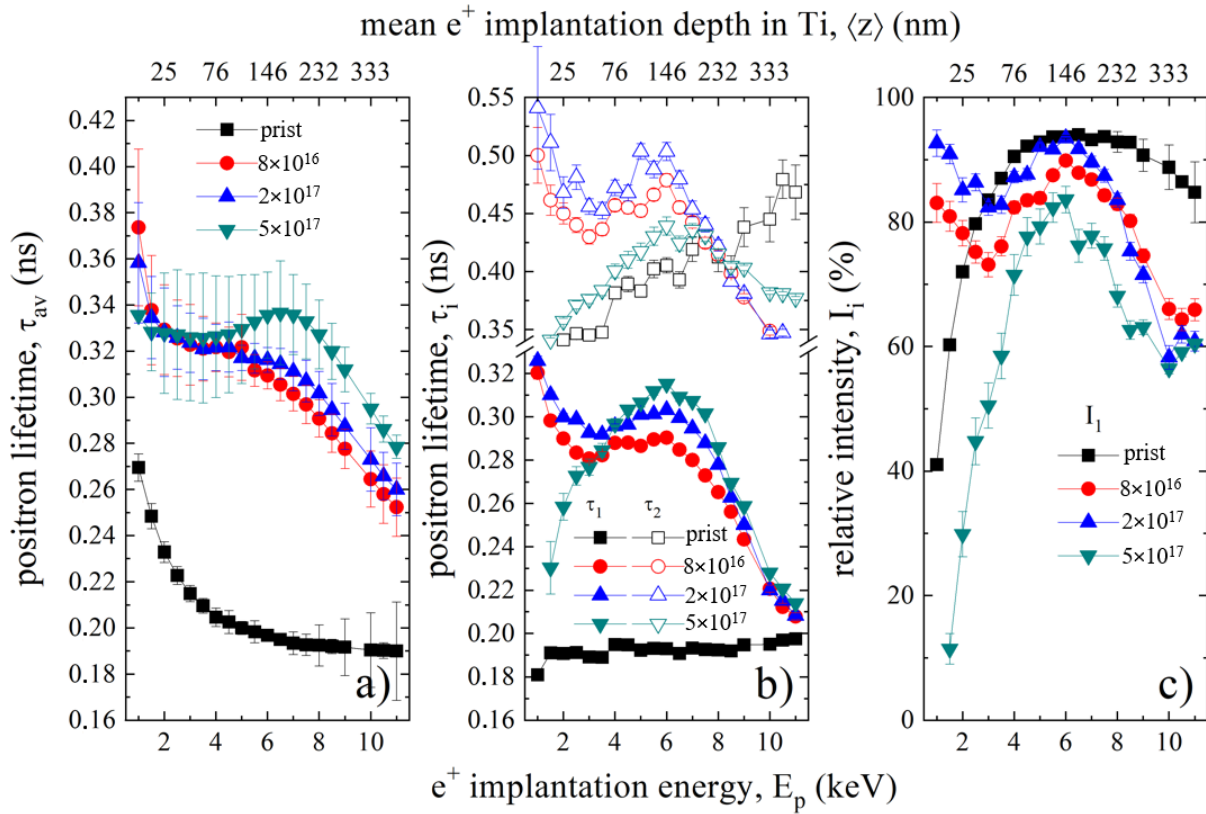


Figure 3.29: VEPALS results for the LANL polished samples. (a) The average positron lifetime, τ_{av} , increases with respect to dose and corresponds well to the S-parameter results, indicating defect size is a dominating factor. (b) Defect sizes calculated from the lifetime components revealed small (3 and 4) vacancy agglomerations from the shorter lifetime τ_1 , and larger vacancy agglomerations (>50) from the longer lifetime τ_2 [84]. (c) The density (relative intensity) of the vacancy agglomerations increases with dose.

3.4.3 Discussion on PAS and Shock Loading of He Implanted Ti

The trends obtained from the DB-VEPAS and VEPALS results correspond well to the AFM and TEM investigations of various dose He ion implantations in Ti described in Sections 3.2 and 3.3, as well as the He profile calculated by SRIM. Figure 3.30 shows the LANL-implanted S-parameter result with an overlay of TEM of He bubbles for 7×10^{17} ions/cm² 25 keV He ions in Ti as well as the projected range of 60 keV He in Ti, which is about 296 nm (assuming constant theoretical bulk density). With increasing dose, the peak damage (S-parameter) shifts deeper to the right. This confirms the increase in swelling with respect to dose.

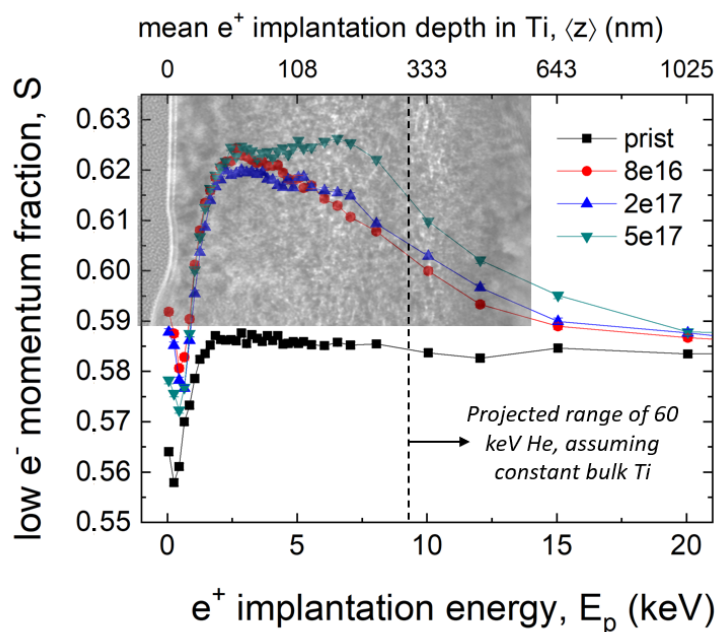


Figure 3.30: The DB-VEPAS results of the LANL-polished samples are in good agreement with our previous results. The inset image is to scale with the graph, and is a TEM micrograph of He bubbles in Ti(0001) from the study described in Section 3.2. The implantation energy for the TEM image was 25 keV He and dose was 7.4×10^{17} ions/cm². The TEM image is underfocused, so He bubbles are shown as white contrast. Additionally, the projected range of 60 keV He in Ti, 296 nm, is annotated. The PALS results are in good agreement with the TEM and SRIM results.

The positrons also detected an increase in bubble density, therefore adding corroborating evidence that TEM analysis alone can be difficult for quantifying small bubbles, since the TEM analysis in Figure 3.12 did not quantitatively reflect the increase in nanocrack sizes with respect to depth into the sample, which was observed qualitatively. This is especially important because the He bubbles implanted at room temperature in Ti are very small, on the order of 1 nm, as described in Sections 3.2 and 3.3 above. The small size of these bubbles makes it extremely difficult to effectively quantify the bubble size distribution in

these samples, although qualitatively we see the formation of nanocracks at increasing depths. Recent attempts to use machine learning and round-robin analysis demonstrate the difficulty to definitively quantify small defects such as He bubbles from TEM micrographs [74]. PAS successfully quantified the vacancy distribution to the order monovacancies. This non-destructive and technique provides additional information about the smaller vacancy-type defects present and difficult to resolve by TEM.

The preliminary condition of combined He bubbles and shock loading was also investigated. Shock loading deformation is known to lead to a very high density of defects in materials, and $\sim 80\%$ of these defects are vacancy-type [76]. There are questions within the community about whether the strain rates during shock loading would be too high for the shock-loading introduced defects to interact with the He bubbles. However, MD simulations have shown that the bubble structures can rearrange within the bulk and near-surface bubbles can eject from the surface [51, 55]. Moreover, the He bubbles decrease the material density. As shown schematically in Figure 3.31, in a surface implantation such as the one here, a plane of bubbles near the surface of the sample may create an impedance mismatch or a surface-roughness effect. This has been shown to effect the surface ejecta during loading [56, 55]. It may also be possible that this impedance mismatch from the He bubbles to the material is enough to cause reflection and thus discrete regions of tension within the bubbled layer.

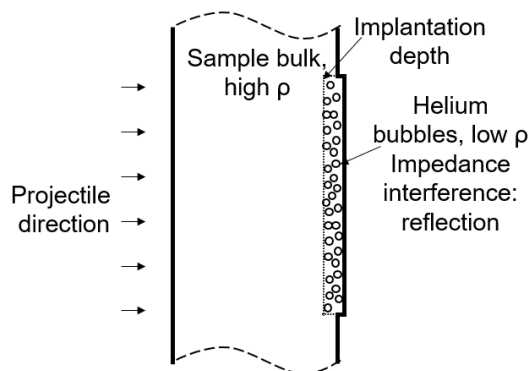


Figure 3.31: Schematic of the potential for a plane of He bubbles, which are lower density than bulk Ti, to create an impedance mismatch and therefore lead to shock reflection.

The 8×10^{16} ions/cm² implant with and without shock loading, as well as a non-implanted and not-shocked (pristine) baseline, is compared directly in Figure 3.32. Shock loading is a high-strain rate deformation mechanism. For context, the strain rates in these experiments are on the order of 1×10^7 /sec, whereas the tensile testing described in Chapter 4 below is on the order of 3×10^{-3} /sec. The strain rate affects the flow stress. That is, at low strain rates, dislocations have time to move and interact during plastic deformation. Thus, different deformation mechanisms may be observed at different strain rates.

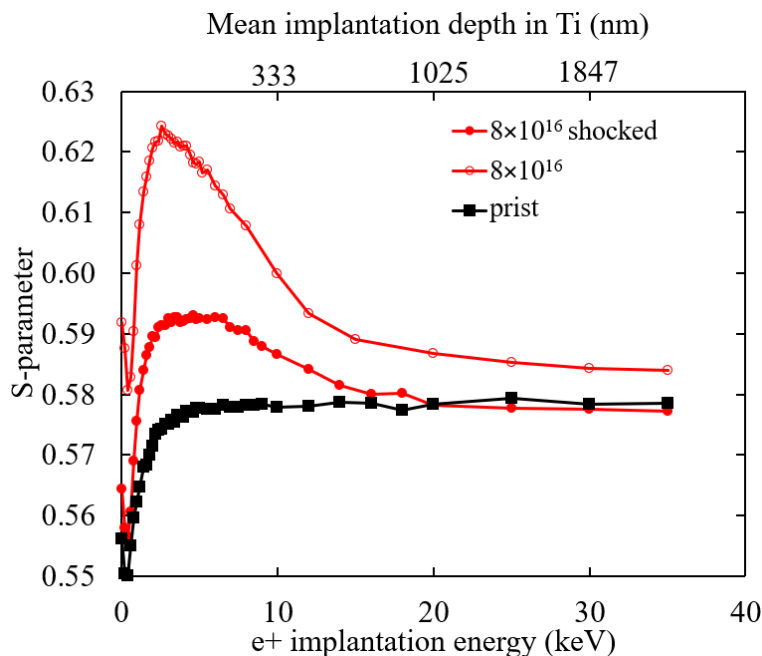


Figure 3.32: Shock loading of the He ion implanted sample led to a decrease in S-parameter. This shows shock loading caused a decrease in vacancy defects in He implanted cp-Ti.

What's most interesting in Figure 3.32 is that the S-parameter, or vacancy-type defect concentration, significantly decreases after shock loading. This indicates the point defects created before shock (through implantation in this case) were recompactd upon shock.

3.4.4 Conclusions on PAS and Shock Loading of He Implanted Ti

PAS can detect clear differences from varying He implantation dose and from shock loading materials. This allows for rapid turnaround, non-destructive quantification of defects to supplement TEM and AFM investigations of He bubble structures and swelling. The DE-VEPAS and VEPALS results correlated well with our previous results, with the PAS-quantified defect structures following the damage and swelling profiles observed by TEM, AFM, and SRIM. VEPALS enabled the measurement of monovacancies to clusters containing >50 vacancies. The majority of these length scales were not resolvable by TEM, and thus PALS studies can be used to support the understanding of how He bubble structure formation is tied to vacancy structures. An additional condition of combined He implantation and shock loading showed the implantation-induced defects recompactd upon shock, resulting in a decreased vacancy concentration. Additional shock loading and PAS studies are needed to understand this further and to support the growing number of reported MD simulations on this topic.

Chapter 4

High Energy Ion Implantation

As mentioned in Section 2.6, difficulties arise when comparing material properties across length scales. Chapter 3 presented extensive microstructural characterization and small-scale mechanical testing of low energy (25-60 keV) shallow (100's of nm) He ion-beam implantations, which are essential for understanding the underlying physics of He effects. This is primarily a methods development chapter on high energy (10's of MeV) bulk-scale (100's of μm) ion implantations and property evaluations, which are needed to further understand how materials perform in nuclear applications. HT-9 is used throughout this chapter because macroscopic data exists for HT-9 and it is a candidate material for advanced reactors.

In this chapter, recent high energy ion implantation efforts at the Lawrence Berkeley National Laboratory (LBL) 88-Inch Cyclotron are discussed. First, the motivation for high energy ion implantation at the 88-Inch Cyclotron and an overview of relevant size effects studies are introduced. Then, a preliminary irradiation and materials testing study at the 88-Inch Cyclotron is detailed. Lastly, the design and simulation of an ion beam degrader, which would enable high energy He implantation at the 88-Inch Cyclotron, is presented.

4.1 Background and Motivation

Radiation damage can significantly change the mechanical properties of materials. The reliability of materials in nuclear environments is an outstanding concern, prompting efforts to develop new “radiation tolerant” materials (such as ferritic/martensitic steels like HT-9) or enhance the confidence in existing ones. The fidelity and reliability of mechanical testing is similarly of interest, given the rising popularity of smaller length scale testing [47, 86].

Traditionally, reactors or accelerators are used to irradiate materials for performance testing [87, 88, 89, 90, 91, 92, 93, 94]. Both approaches benefit from smaller material testing techniques. Small scale testing produces a smaller volume of radioactive-material and requires a shorter irradiation time to achieve a desired number of displacements per atom (dpa), leading to faster testing throughput, reduced radiation safety concerns, and facilitating sample testing with widely available low-energy accelerators. Limited space in

irradiation facilities and the rapidly growing availability of new alloys also motivate small scale testing [47]. Today, many small-scale testing techniques, such as nanoindentation, microcompression, microtensile, and microbend testing, have been adapted for nuclear applications. However, a significant amount of research is still needed to correlate small-scale testing with bulk properties [95].

In the literature, sample size dependencies on mechanical properties have been characterized as either intrinsic (microstructural related) or extrinsic (dimension related) [96]. In polycrystalline materials, the grain size serves as an internal length scale which is well-known to influence strength by means of the Hall-Petch effect [97, 98]. Test geometry, such as tensile test sample gauge thicknesses or width, serves as another length scale impacting the measured strength [99, 100].

Figure 4.1, adapted from Hosemann et al., presents observed size effects for unirradiated materials and hypothesized size effects for irradiated materials [101]. For the unirradiated materials, when test geometry sizes are significantly large, they capture enough grains to represent “bulk” material properties. As the test geometry size decreases, there is a competition between surface grain relaxation and interior grain strengthening. Depending on the gauge length width-to-thickness aspect ratio, surface grain relaxation may take over, resulting in a “dip” in material strength [97, 98, 99, 100, 102]. As the sample geometry continues to decrease in size, there is a competition between the dislocation-motion and dislocation-source mechanisms. As a result, the strength increases due to the dislocation-source mechanism dominating. This length scale is referred to as the quasi-static crystal regime [47, 103]. The strength will continue to increase inversely with sample size, potentially approaching the theoretical strength where no dislocation is present or can be created [102, 103].

The dotted curve in Figure 4.1 represents the theoretical size effects of irradiated materials. Due to the small size and large number of radiation-induced point defects, these defects serve as a small internal length scale. Therefore, radiation defects may suppress size effects. However, once the irradiated sample size becomes small compared to the length scales represented by grains or radiation damage, the behavior will return to that of the unirradiated material, with the strength approaching the theoretical strength [103, 104]. The theoretical size effects of irradiated materials represented in Figure 4.1 only considers displacement damage. He bubbles have shown different behavior. Nano-compression, bending, and tensile testing, such as those described in Section 2.6.2., have shown that He-implanted nanostructures enhance ductility, which is in contrast to He embrittlement observed in bulk He-containing materials [34, 35, 48, 53, 54].

There is a wealth of activity examining size effects in the nano-microscale (nm to 10s of μm), which is limited to single crystal, ultra-fine grain, and non-homogenized properties [35, 47, 53, 96, 103, 104, 107, 108, 109, 105, 106]. Limited experimental data exists at the micro-mesoscales needed to investigate size effects beyond the nano-microscale and support multi-scale modeling [99, 100, 110]. Concurrent size effect studies at UC Berkeley have produced experimental data for SS-J geometry tensile samples for a variety of nuclear materials [111]. The SS-J geometry is shown in Figure 4.2. A variety of sample thicknesses in the micro-mesoscale (30–750 μm thickness) were tested in efforts to bridge length-scale gaps. Size

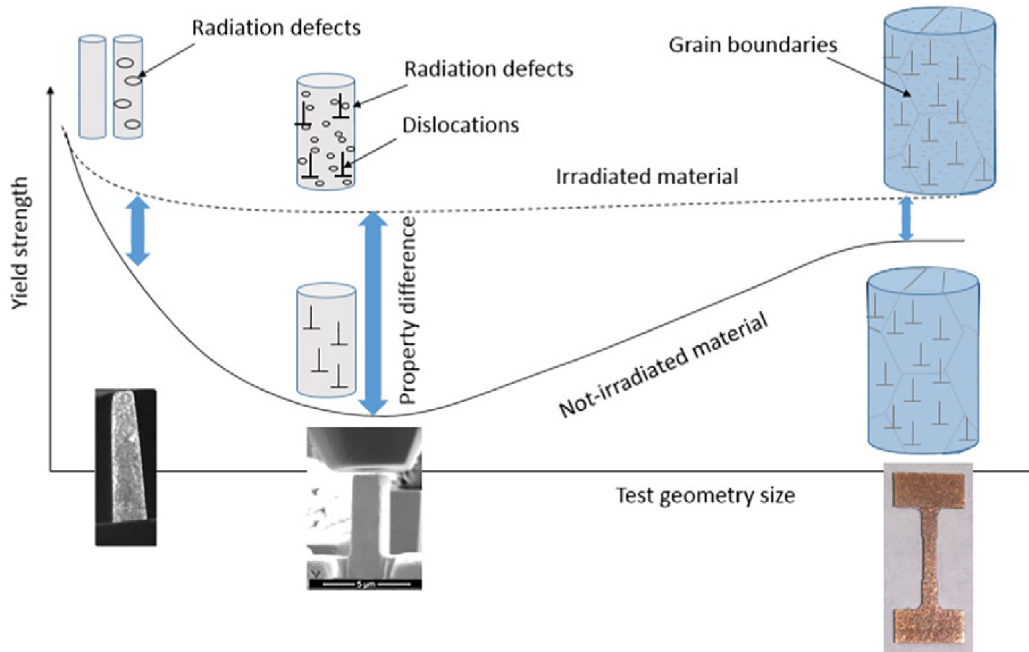


Figure 4.1: Proposed size effects of irradiated and not-irradiated polycrystalline materials, adapted with permission from [47]. For not-irradiated materials, bulk-scale properties are captured when there are a significant number of grains. A dip in strength is observed when the sample geometry is such that surface grain relaxation dominates. At the smallest sample sizes, the strength approaches the theoretical strength. For irradiated materials, it is proposed that displacement damage creates a new internal length scale, therefore diminishing size effects, although the smallest samples will also approach the theoretical strength. The proposed curve for irradiated materials only considers displacement damage, while He effects may behave differently. Copyright 2018 Elsevier.

effects were observed for the thinnest samples, and it was determined that at least $100\ \mu\text{m}$ thick samples were needed for reliable testing in the Kamrath & Weiss Tensile Module (KW) at UC Berkeley.

This brings about the need for high energy ion implantation for size-effect studies with irradiated samples. In this work, HT-9 is considered for initial high energy ion implantation studies, because it is a candidate nuclear material with a large tensile database, both in literature and in the UC Berkeley small scale tensile testing studies.

He ion beam implantations are widely performed to understand the effects of irradiation damage on nuclear structural materials. Yet, the volume of material that can be investigated is often limited by the maximum energies of accelerator facilities. Most studies are performed at tandem accelerators with a 3 MeV maximum energy [112]. Shown in Figure 4.3(a), 3 MeV He corresponds to a peak beam penetration depth of about $4.25\ \mu\text{m}$ in HT-9 steel. However, the aforementioned UC Berkeley studies revealed that $100\ \mu\text{m}$ is the thickness of SS-J geometry samples that can reliably be measured in a uniaxial tensile test [111]. This corresponds to at least 23 MeV He in HT-9, as shown in Figure 4.3(b).

The 88-Inch Cyclotron shows promise for future macroscale materials testing, offering a

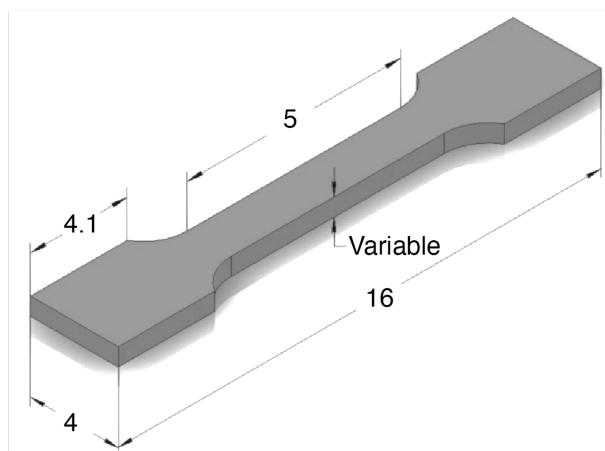


Figure 4.2: Standard dimensions for SS-J tensile samples. In the size effects studies described here, the sample thicknesses were varied. 100 μm was found to be the thickness of samples needed for reliable testing with the KW at UC Berkeley.

broad range of heavy and light ions ($Z \leq 92$), high energies (up to 70 MeV deuterons and 140 MeV ^4He) necessary to penetrate through macroscale samples, and high currents (10's of μA) for achieving at least 1 dpa in several days of irradiation time. Section 4.2 describes a quick-turnaround material testing capability using the Cyclotron and bench-top tensile testing of irradiated samples, contributes to the growing ferritic/martensitic steels (F/M) steel property database, and provides insight into irradiation damage effects and small-scale testing limitations. Section 4.3 details the development of a tool that can uniformly implant materials with He for subsequent bulk-scale materials testing, such as tensile or shock loading experiments.

4.2 Preliminary Study at the 88-Inch Cyclotron

This preliminary study demonstrated rapid-turnaround materials testing capabilities at the LBL 88-Inch Cyclotron, and informed design decisions for the ion beam degrader system described in Section 4.3 [113, 114]. This work also established a Standard Operating Procedure (SOP) for radioactive sample tensile testing at UC Berkeley, which is reproduced in Appendix A.

In this study, SS-J tensile geometries with different thicknesses were irradiated with high-energy deuterons and subsequently tested. The thickness range of this study, combined with concurrent size effect studies, was selected to bridge the experimental length-scale gap and make use of the irradiation depths possible with the 88-Inch Cyclotron at Berkeley [89]. HT-9, a ferritic/martensitic (F/M) steel, was used since it a candidate material for advanced nuclear reactors with an extensive tensile testing database [88, 91, 111]. In F/M steels, low temperature (≤ 300 °C) radiation-induced displacement damage has been known to cause

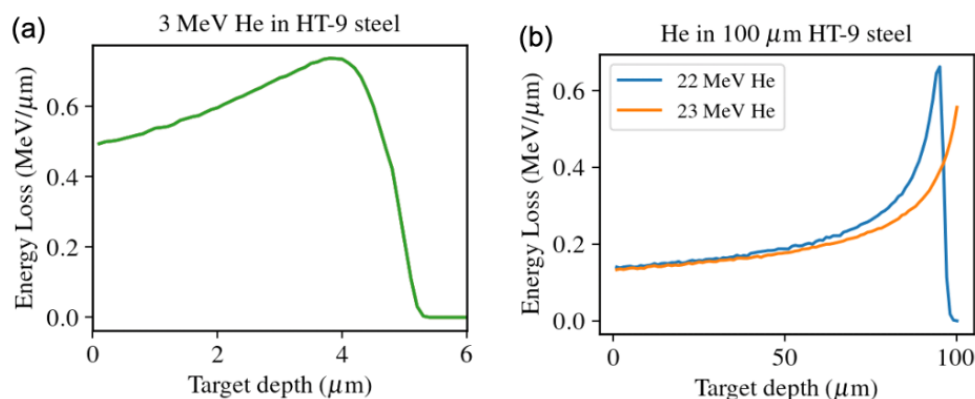


Figure 4.3: Range comparison of (a) 3 MeV and (b) 22 and 23 MeV He in HT-9 steel, assuming constant theoretical density of HT-9 and calculated using SRIM-2013. The 3 MeV He is stopped in the first few μm , while 22 MeV is stopped in 100 μm HT-9, and 23 MeV penetrates through 100 μm HT-9.

hardening which is characterized by an increase in yield and ultimate tensile strength and a decrease in uniform elongation (ductility) [87, 88, 89, 90, 91, 92, 93]. The results from this study revealed irradiation hardening characterized by the tensile properties and black dot irradiation defects. Additionally, a comprehensive look at low temperature irradiations of high-Cr F/M steels is presented and our results show agreement with the available data.

4.2.1 Methods for the Preliminary High Energy Ion Implantation Study at the 88-Inch Cyclotron

HT-9 SS-J tensile specimens were prepared from heat # V1608621 produced by Metalwerks with a composition of Fe 12.2Cr-1.1Mo-0.51 W-0.57Ni-0.30 V-0.21C-0.29Si-0.32Mn (in wt%). The stock HT-9 was heat treated at 1040 °C for 30 min, AC (air-cooled) and subsequent 760 °C for 1 hr, AC. After the heat treatment, the stock was cut into a bar with SS-J outer dimensions using wire electrical discharge machining (EDM). The outside of the SS-J bar was polished to remove an oxide scale. A Struers Accutom-50 with a SiC blade was used to slice individual tensile specimens from the larger SS-J bar. Subsequently, the tensile samples were polished down to thickness using SiC abrasive sheets up to 1200/P4000 grit, and optically inspected to ensure a clean and defect-free surface. The thickness of each sample was measured at each shoulder and gauge length using a micrometer with ± 1 μm tolerance.

4.2.1.1 Deuteron Irradiation

The deuteron irradiation was carried out at the Lawrence Berkeley National Laboratory's 88-Inch Cyclotron. During the 5.3-day irradiation, the current fluctuated from 9 μA to 1

μA , with a weighted average current of about $3.9 \mu\text{A}$, corresponding to about 3×10^{18} ions. The deuterons were incident on a target stack with 4 tensile specimens, as depicted in Figure 4.4 [115]. Due to the high energies used, there were concerns with the sample clamping configuration providing good thermal contact for efficient sample cooling. Thus, two different sample clamping configurations (side-by-side and back-to-back) were used to assess the effectiveness of each and set a precedent for future experimental configurations. The $202 \mu\text{m}$ and $91 \mu\text{m}$ thin samples were stacked on top of each other and clamped between two 1.45 mm thick sheets of Be metal. The remaining two samples, each $40 \mu\text{m}$ thin, were placed side-by-side and clamped between one of the 1.45 mm sheets of Be and the Al beam stop. The sample temperature was not monitored during the irradiation. However, the samples were placed in good thermal contact with a continuous flow low conductivity water cooling plate, and previous 5-day high powered irradiations with this configuration had a steady state sample temperature under $60 \text{ }^\circ\text{C}$ [116].

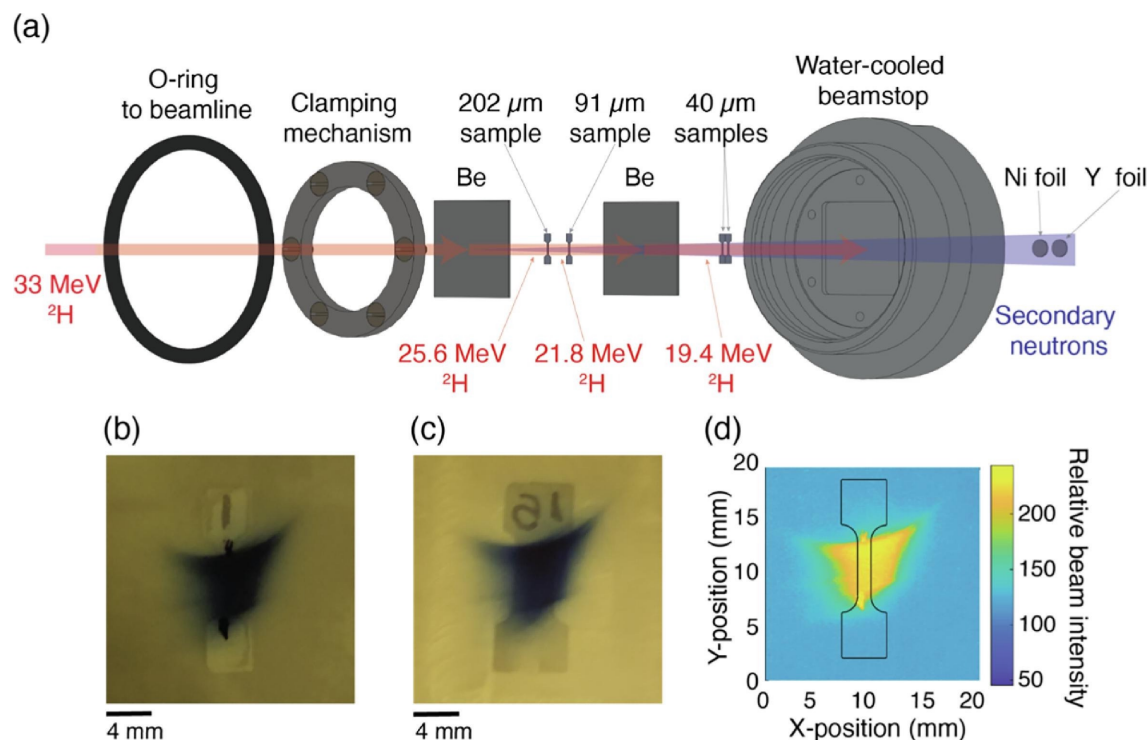


Figure 4.4: Experimental setup of the 5.3 day HT-9 SS-J deuteron irradiation at the 88-inch Cyclotron. (a) Exploded view of the target setup. The 33 MeV deuterons (^2H) were attenuated by the Be and HT-9 layers, and the deuteron breakup on the Be produced secondary neutrons which were monitored with Ni and Y foils. (b) GAFChromic film showing the spatial beam profile on the 202 and $91 \mu\text{m}$ sample stack. (c) GAFChromic film showing the spatial beam profile on the $40 \mu\text{m}$ samples. (d) GAFChromic film measurement result with an overlay of the SS-J geometry. As shown in (b)–(d), the beam spot was about 0.38 cm^2 and centred on the SS-J gauge region so the grippers were not irradiated.

In addition to the deuteron beam, secondary neutrons were produced from the $\text{Be}(d,n)$ reaction. To measure the neutron fluence and energy, 1 cm diameter by 1 mm thick Ni and

Y neutron monitor foils were placed in a 0.5-inch diameter blind hole in the back of the beam stop. Following the experiment, the neutron monitor foils were counted on an ORTEC GMX Series (model GMX-50220-S) High-Purity Germanium (HPGe) detector, and calibrated with 1 μ Ci Ba-133, Cs-137 and Eu-152 sources from Eckert Ziegler, traceable to NIST. Using the $^{58}\text{Ni}(n,2n)^{57}\text{Ni}$, $^{58}\text{Ni}(n,p)^{58}\text{Co}$, $^{89}\text{Y}(n,2n)^{88}\text{Y}$, and $^{89}\text{Y}(n,3n)^{87}\text{Y}$ monitor reactions and cross sections from the IRDFF-II Library, the secondary neutron fluence incident on the samples was calculated to be $(2.83 \pm 0.19) \times 10^{17}$ neutrons/cm², with an average neutron energy of 11.87 MeV [117].

The spatial profile of the deuteron beam entering the target stack was imaged with Radiochromic film (GAFchromic EBT3). Figure 4.4(b)–(d) shows the location and shape of the beam, with the SS-J geometries included for scale. The beam spot size was approximately 0.38 cm² and centred on the gauge regions to avoid irradiating the sample grippers. The 33 MeV deuteron beam was degraded by the layers of Be and HT-9 samples in the target stack. Energy loss calculations were performed by using a cumulative trapezoidal integration of the stopping curves produced by SRIM-2013 with 40 eV displacement energy, resulting in a 25.6 MeV, 21.8 MeV, and 19.4 MeV beam incident on the 202 μ m, 91 μ m, and 40 μ m samples, respectively [95]. Consequently, all the samples, save for the two side-by-side 40 μ m samples, were expected to receive energy-dependent doses. The deuteron dose in each sample was calculated using the SRIM-2013 code and method described in Section 2.1. Figure 4.5 shows the calculated dpa as a function of depth for the samples. The average SRIM-calculated dpa in the 202 μ m, 91 μ m, and 40 μ m samples was 0.18, 0.2, and 0.22, respectfully. It should be noted that the additional secondary neutron fluence contributed to the observed sample radioactivity and increased dpa relative to that calculated using SRIM.

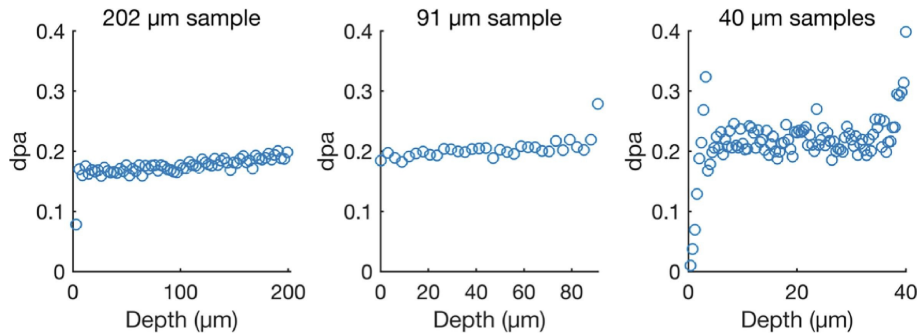


Figure 4.5: Dpa as a function of depth into the HT-9 samples, calculated from SRIM-2013 code. The average dpa was 0.18, 0.2, and 0.22 for the 202 μ m, 91 μ m, and 40 μ m samples, respectively.

Approximately 5 months following the irradiation, activation product activities in the tensile samples were measured through gamma spectroscopy [115]. To avoid saturating the HPGe detector, the samples were placed in a lead pig approximately 2 m from the detector’s front face. All tensile samples were counted together, and the resulting spectrum is shown in Figure 4.6. The overwhelming majority of the produced activity was due to ^{56}Co

(approximately 98.6 mCi), which masked other expected spectral lines, such as those from ^{58}Co and ^{60}Co . ^{56}Co has a half-life of 77.236 ± 0.026 days [118], permitting an estimate of the activity at the end of irradiation of 394.4 mCi of ^{56}Co .

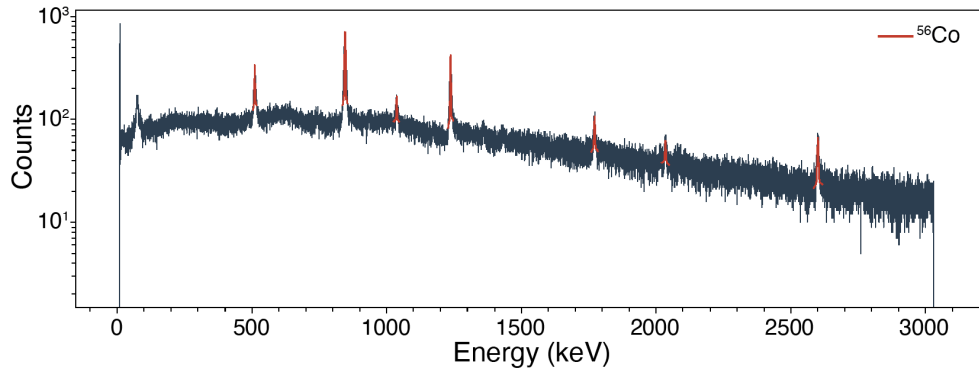


Figure 4.6: Gamma spectrum from all four HT-9 SS-J samples measured 5 months following the 33 MeV deuteron irradiation. The samples were counted in a lead pig 2 m away from the front of the HPGe detector. The majority of the measured radioactivity was from ^{56}Co , whose photopeaks are indicated in red.

From the bulk Fe content of HT-9 steel, ^{56}Co is produced from $^{56}\text{Fe}(d,2n)$ (threshold: 7.8 MeV), $^{57}\text{Fe}(d,3n)$ (threshold: 15.7 MeV), and a small amount via $^{58}\text{Fe}(d,4n)$ (threshold: 26 MeV) [119]. ^{56}Co can also be made via $^{58}\text{Ni}(d,a)^{56}\text{Co}$ (no threshold), $^{60}\text{Ni}(d,a2n)$ (threshold: 14.3 MeV) and $^{61}\text{Ni}(d,a3n)$ (threshold: 22.4 MeV). In addition, rather than emitting an alpha particle, each of those Ni(d,ax) channels can instead emit combinations of two protons and two neutrons (at slightly higher energies), further boosting yields.

The samples were received at UC Berkeley for tensile testing approximately 8 months following the irradiation, to allow time for the Co activities to decay to a safe level for handling. The on-contact dose rate of each sample was measured using a calibrated ion chamber at the time of tensile testing. For the 202 μm , 91 μm , and two 40 μm samples, the on-contact dose rates at time of tensile testing were approximately 2 R/hr, 1 R/hr, 7 mR/hr, and 2 mR/hr, respectively. These dose rates made it acceptable to perform the tensile testing on a shielded benchtop.

4.2.1.2 Tensile Testing

With guidance from the UC Berkeley Environmental Health and Safety (EH&S) Radiation Safety team, a SOP for tensile testing irradiated samples were created and formally approved by the campus (see Appendix A). Tensile testing of both unirradiated and irradiated samples was carried out using a Kammrath & Weiss Tensile Module (KW) with a 500 N load cell and engineering strain rate of 3×10^{-3} /s (15 $\mu\text{m}/\text{sec}$ stroke rate). Samples >600 μm thick required use of a 5 kN load cell. All samples were pulled until failure. An optical camera was employed to record a video of the samples during tensile testing, with the added ability to perform digital image correlation as needed. The original gauge thickness measured before

testing was used for calculating the stress/strain curves and the machine compliance was subtracted from the load/displacement curves. These curves were used to determine 0.5% offset yield strength (YS), ultimate tensile strength (UTS), and reduced uniform elongation (UE). The UE is calculated by subtracting the elastic portion of the strain at UTS, whereas total uniform elongation would include this portion.

4.2.1.3 Post-Irradiation and Tensile Testing Electron Microscopy

After irradiation and tensile testing, the failure surface of each sample was characterized by Scanning Electron Microscopy (SEM) using a FEI Quanta 3D Field Emission Gun (FEG). Then, the 40 μm sample with an on-contact dose rate of 7 mR/hr was taken as the representative sample for additional microstructure characterization. TEM lamella was produced from the irradiated gauge section, reasonably far from the fracture site, using a Thermo Scientific Scios 2 DualBeam focused ion beam system. The final lamella thickness after Ga ion beam thinning was approximately 108 nm. For the irradiated microstructure characterization, TEM images were acquired using a FEI ThemIS 60–300 STEM/TEM.

4.2.2 Results on the Preliminary High Energy Ion Implantation Study at the 88-Inch Cyclotron

Unirradiated HT-9 SS-J samples with gauge thicknesses ranging from 24–752 μm were used as controls for comparison of combined geometric and radiation effects on tensile properties. The irradiated and unirradiated HT-9 SS-J samples came from the exact same batch and heat treatment. Table 4.1 provides the irradiated and unirradiated samples' gauge thicknesses, YS, UTS, and UE, as well as the irradiated samples' dpa and on-contact dose rates.

The change in tensile properties are presented by stress-strain curves shown in the left-hand column of Figure 4.7. Except for the 202 μm sample, which showed an increase in YS of approximately 15%, the average increase in YS after irradiation is approximately 35%. The difference in the 202 μm sample could have been due to premature fracture observed at the sample shoulder during the tensile testing. For all samples, compared to the unirradiated HT-9, the irradiated HT-9 undergoes significantly less strain hardening before fracture. A significant (approximately 75%) loss of ductility is observed with irradiation. It should be noted that since the irradiation was primarily due to deuterons, hydrogen embrittlement needs to be considered. However, given that the ion beam does not stop in the samples, hydrogen is highly mobile in metals, and the prolonged irradiation time, we would suggest that it the hydrogen is not a major concern during this irradiation. Ductility loss can be explained by radiation-induced displacement damage which clusters into cavities and loops. This displacement damage impedes dislocation motion during plastic deformation, thereby impacting YS and decreasing plasticity. A decrease in plasticity is expected to increase with dose, but eventually will saturate when defect overlapping becomes dominant, which is often reported to be around 10 dpa for high-Cr F/M steels such as HT-9 [86, 88, 90, 120]

SRIM average dose (dpa)	On contact dose rate 8 mo after irradiation	Gauge thickness (μm)	Yield Strength (MPa)	UTS (MPa)	UE
0.18	2 R/hr	202	658.99	758.66	0.02
0.2	1 R/hr	91	797.53	875.11	0.03
0.22	7 mR/hr	40	732.39	893.89	0.03
0.22	2 mR/hr	40	783.06	896.03	0.01
0	-	29	505.96	672.41	0.03
0	-	42	516.39	678.64	0.03
0	-	44	395.78	614.48	0.06
0	-	45.5	435.77	557.30	0.03
0	-	63	545.90	773.51	0.07
0	-	64.5	484.16	619.86	0.03
0	-	90	486.65	704.76	0.08
0	-	122.5	484.54	638.85	0.07
0	-	131	514.36	703.00	0.06
0	-	187	577.25	763.33	0.08
0	-	189.5	576.39	766.48	0.07
0	-	202	581.95	775.47	0.08
0	-	217	512.77	688.92	0.10
0	-	250	599.11	787.01	0.09
0	-	274	549.10	724.71	0.09
0	-	285.5	590.31	776.27	0.09
0	-	411	584.41	766.90	0.09
0	-	416	575.89	757.79	0.09
0	-	448	593.50	784.21	0.09
0	-	497	598.27	779.49	0.09
0	-	508	591.43	768.41	0.09
0	-	606	529.92	723.08	0.10
0	-	617	540.61	737.75	0.10
0	-	687	545.99	744.45	0.10
0	-	691	551.71	743.67	0.10
0	-	753	554.11	747.54	0.09

Table 4.1: Summary of parameters and properties for irradiated and not-irradiated SS-J geometry HT-9 tensile samples tested at UC Berkeley [111, 113]

Respective SEM micrographs of the failure surface for each irradiated sample is shown to the right of each stress-strain curve in 4.7. For all samples, the failure surface appears to be indicative of an intermediate ductile/brittle fracture mechanism. That is, the failure surfaces do not consist of entirely “dimpled” ductile type failure or “faceted” brittle type failure. HT-9 has a BCC crystal structure and therefore no close-packed planes to allow for easy dislocation migration under mechanical deformation. BCC slip systems must be thermally activated, in what is known as the ductile-brittle transition temperature (DBTT). Although the DBTT of unirradiated HT-9 is below room temperature, radiation-induced upshifts in DBTT have been reported, meaning brittle failure is apparent at higher temperatures than it would be before irradiation, due to radiation hardening and/or radiation-induced segregation (RIS) of impurities to grain boundaries [88, 90]. It is possible the moderate dose in this experiment has not shifted the DBTT enough, hence the appearance of an intermediate mode failure. Further, it should be noted that sample geometry effects on the failure mode are not decoupled from irradiation effects in this experiment.

To investigate the defect structure, the 40 μm thick, 7 mR/hr sample was characterized by TEM. Figure 4.8 was produced using a two-beam condition, and shows the sample is heavily decorated with black dot irradiation defects. This is expected based on previous neutron irradiations of HT-9, which show black dot defects at a small threshold dose, and resolvable loops beginning around 1 dpa [121, 122]. An attempt was made to analyze the black dot defects, as demonstrated in Figure 4.8(b)-(c), however, due to the low resolution, there is a significant error in quantifying the defects. 4.8(c) represents a high estimate of the defect size and number, while 4.8(d) represents a low estimate. As a result, the average major diameter of the black dots were approximately 6 ± 2 nm, and the number density is estimated $1.6 \times 10^{14} \pm 10^{14} \text{ m}^{-2}$.

Figure 4.9 shows the obtained YS, UTS, and UE as a function of gauge thickness for unirradiated and the deuteron-irradiated samples. For the unirradiated (0 dpa) HT-9, the YS appears to remain relatively constant (~ 575 MPa) at thicknesses down to about 200 μm . Below 200 μm , the unirradiated YS values begin to decrease with a slope of approximately 0.9 MPa/ μm . A similar trend is observed for the unirradiated UTS, with the UTS relatively constant (~ 750 MPa) then decreasing with a slope of about 1 MPa/ μm below 200 μm . The unirradiated UE is also relatively constant (~ 0.09) then decreases with respect to gauge thicknesses below 200 μm , though when compared to that seen for YS and UTS, the dip is more significant. Around 50 μm , a $\sim 70\%$ reduction in UE compared to bulk thickness is observed. The four irradiated samples with gauge thicknesses of 202, 91, and 40 μm exhibited a YS and UTS generally higher than that of the bulk (>200 μm) unirradiated values, UE generally lower than all unirradiated values, and these irradiated tensile properties did not increase with decreasing sample gauge thickness.

The small specimen preparation and tensile testing procedures used here are very repeatable. However, there is clear variance within the data, especially at thinner thicknesses. This variance may be due to limitations of the SS-J sample geometry at thicknesses much thinner than the design. Additionally, while thickness errors were calculated and plotted, the errors themselves are not comprehensive, and thickness variations on the order of ± 5 μm

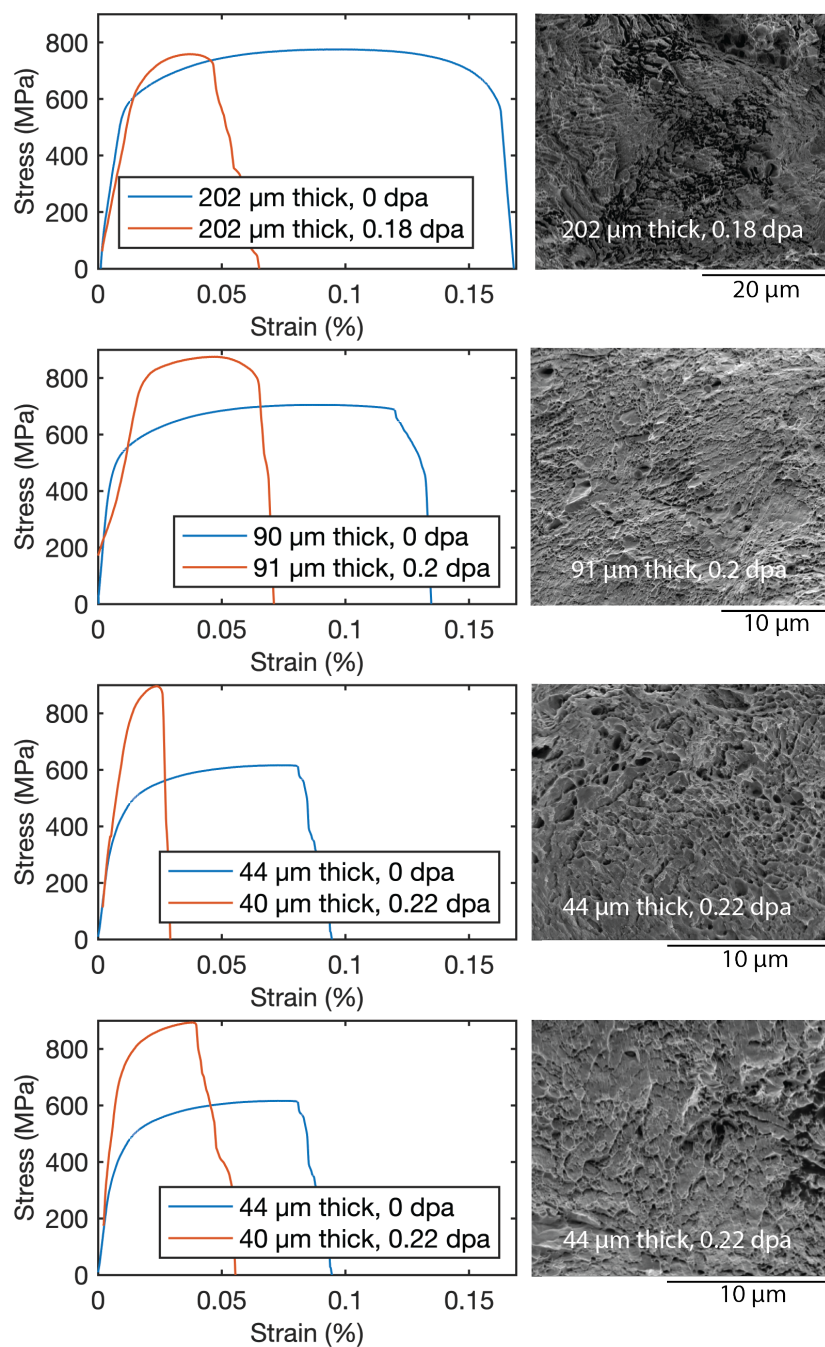


Figure 4.7: Effect of 0.18, 0.2, and 0.22 dpa deuteron irradiation on the stress strain curve production of 202 μm, 90 μm, and 40 μm thick HT-9 SS-J tensile samples, respectively. An increase in YS and reduction in ductility is observed, indicating radiation hardening. Corresponding SEM images of the failure surfaces for are shown on the right, showing an intermediate ductile/brittle failure mechanism.

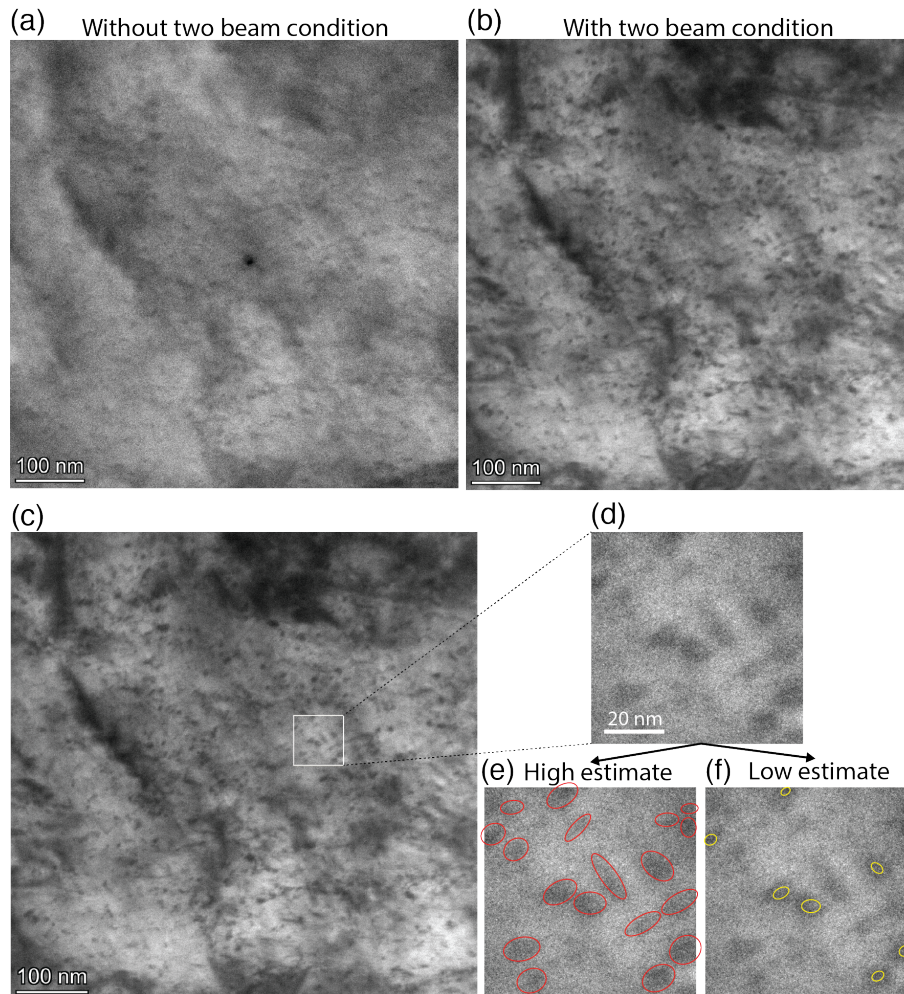


Figure 4.8: TEM investigation of the 40 μm thick, 7 mR/hr sample. The TEM lamella was taken from the irradiated gauge section and far from the tensile fracture site. (a)-(b) A comparison of the same region without two beam and with two beam conditions, Black dot irradiation defects are revealed by the two beam condition. (c) Annotated version of (b), used in (d)-(f) to exemplify the method used to quantify the black dot defects. (d) Magnified area, annotated in (e),(f) as an example of a high and low estimate for the black dot radiation defect size and number.

may be increasingly significant with decreasing sample thickness. For the irradiated data, there are additional unaccounted for errors within the dpa calculations themselves, given the assumptions provided in the methods above and the differences in measured on-contact dose rates. Reference [111] is recommended for a more comprehensive explanation of scatter within the unirradiated data.

The dependencies of some tensile properties such as YS on sample thickness and aspect ratio have previously been reported [99, 100]. So long as the aspect ratio is not too extreme, the critical sample thickness can be attributed to sample microstructure; generally, about 10 grain diameters across the thickness is desired for reliable F/M steel tensile testing [122].

Moreover, it is known that the presence of radiation defects yields a smaller critical thickness, or in other words, suppressed microstructural size effects [99, 100, 101, 123]. Radiation defects not only increase the strength of polycrystalline materials, but also the presence of many radiation defects and their small size have been shown to create a small internal length scale in materials [101, 123]. Furthermore, Kohno et al. observed that JFMS (9% Cr) F/M steel size effects were still apparent with light neutron irradiation on the order of mdpa but were diminished after neutron irradiation on the order of 10's of dpa [99].

Looking at the unirradiated SS-J geometry HT-9 studies, it would appear the critical thickness is 200 μm , however the lath size of F/M steels is typically 1-2 μm [111]. This yields roughly 14 laths across the thickness of our thinnest (29 μm) unirradiated samples, implying there should be no thickness effects observed. Thus, the observed changes in unirradiated tensile properties with respect to thickness may help us separate microstructural size effects from sample geometry effects. Although the irradiated data is too limited to make a definitive conclusion, it is possible the irradiation effects on the tensile properties are not sensitive to the sample geometry effects.

4.2.3 Discussion on the Preliminary High Energy Ion Implantation Study at the 88-Inch Cyclotron

Despite the limited test matrix in this experiment, it is useful to compare the results to previous data in the literature. Since many high-Cr (9–12% Cr) F/M steels have common features and have been studied alongside HT-9, they will be referred to in this discussion.

F/M steels are candidate in-core structural materials for future nuclear reactors, where it is estimated that the operating temperature ranges from 280-650 $^{\circ}\text{C}$ and light irradiation only occurs at the beginning of the operation lifetime [120]. The HT-9 data available in the irradiation temperature range of 373–427 $^{\circ}\text{C}$ showed that the impact of irradiation on tensile properties diminished at temperatures above 400 $^{\circ}\text{C}$, but there may be enhanced softening characterized by a decrease in YS due to radiation enhanced diffusion [120].

F/M steels are also envisioned for out-of-core applications, where the temperatures and irradiation fluence may be much less than in-core conditions. A concern for nuclear applications of high-Cr F/M steels has been previously identified to be the low-temperature (≤ 300 $^{\circ}\text{C}$) embrittlement resulting from radiation hardening [88, 120]. The irradiation-induced up-shift in DBTT is particularly concerning for nuclear structural materials, where catastrophic failure is not an option, because it can lead to brittle fracture instead of the preferred ductile (“leaking before breaking”) fracture mechanism [124].

Due to the primarily in-core applications for HT-9, little data is available for low temperature irradiations and nearly no data is available < 1 dpa. Comprehensive low-temperature (≤ 300 $^{\circ}\text{C}$) irradiation and room temperature tensile tests ΔYS and % decrease in UE results are shown in Figure 4.10 for a variety of high-Cr F/M steels, alongside results from the low-temperature irradiation experiment in this study. The % decrease in UE is calculated as follows:

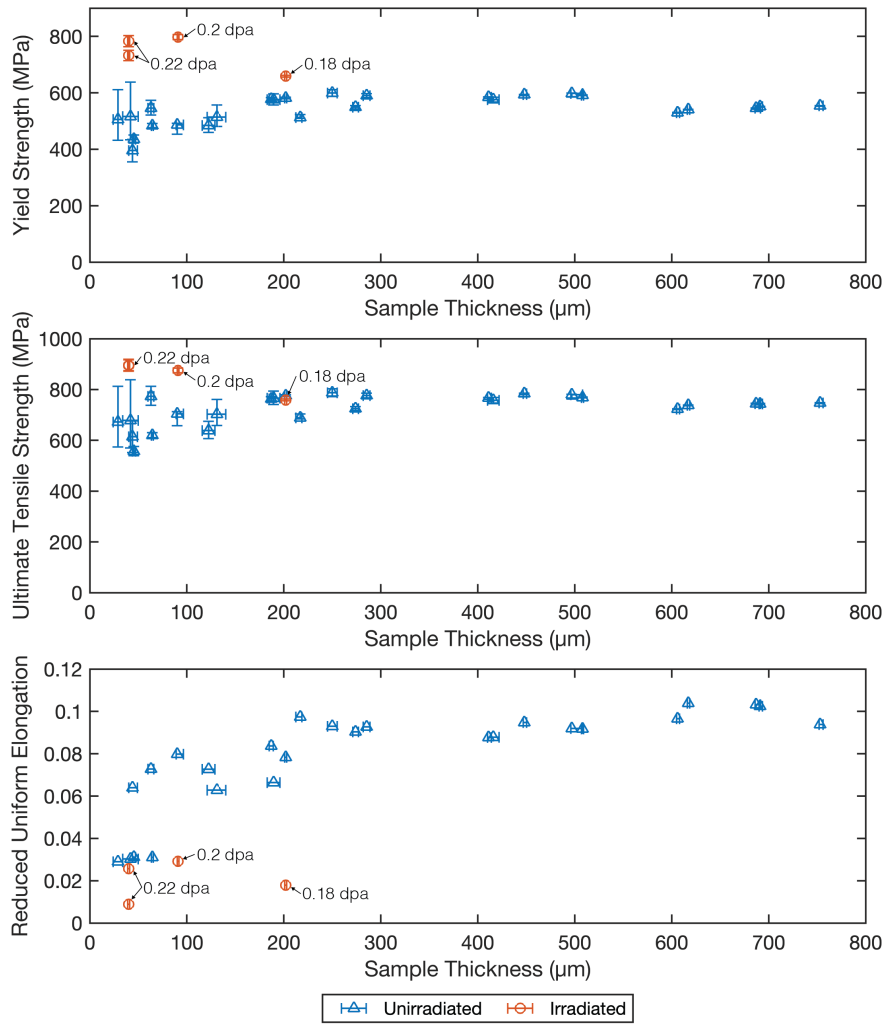


Figure 4.9: Effects of 0.18–0.22 dpa deuteron irradiation on thickness dependence of YS, UTS, and UE in HT-9. Unirradiated data is adapted from Dong et al. [111]. A dip is observed below approximately 200 μm in all material properties for the unirradiated samples. The irradiated samples appear to show an increased YS and UTS and decreased UE compared to the unirradiated bulk (>200 μm) properties.

$$\% \text{ decrease in } UE = \frac{UE(0 \text{ dpa}) - UE(x \text{ dpa})}{UE(0 \text{ dpa})} \quad (4.1)$$

Where $UE(0 \text{ dpa})$ is the reported UE at 0 dpa and $UE(x \text{ dpa})$ is the reported UE at a specific dpa. The data in Figure 4.10 is comprised from a variety of different materials and test parameters described in Table 4.2.

A general trend is apparent in the ΔYS and % decrease in UE data. Radiation hardening, which is accompanied by an increase in YS and a decrease in UE, begins at the lowest reported

Sample	Radiation source	Geometry/ thickness (μm)	Irradiation temperature ($^{\circ}\text{C}$)	Reference
HT-9	88-Inch Cyclotron (deuterons)	SS-J/40-202	60	
HT-9	HFIR	SS-3/760	300	[89]
9Cr-1MoVNB	HFIR	SS-3/760	60-100	[90]
9Cr-1MoVNB	LANSCE	SS-3/760	60-164	[90]
9Cr-1MoVNB-2Ni	HFIR	SS-3/760	60-100	[90]
9Cr-2VW-Ta	HFIR	SS-3/760	60-100	[90]
9Cr-2VW-Ta	LANSCE	SS-3/760	60-164	[90]
9Cr-2WV	HFIR	SS-3/760	60-100	[90]
9Cr-3WV	HFIR	SS-3/760	60-100	[90]
A533B	HFIR	SS-3/760	60-100	[90]
OPTIMAX A	PIREX (protons)	Not specified	27-47	[91]
F82H	LANSCE	250-750	30-100	[92]
OPTIMAX A	LANSCE	250-750	30-100	[92]
12 Cr-1 MoVW (91354)	HFIR	760	50	[126]
12 Cr-1 XAA-3587	HFIR	760	50	[126]
12 Cr-1 XAA-3588	HFIR	760	50	[126]
12 Cr-1 XAA-3589	HFIR	760	50	[126]
12 Cr-1 XAA-3592	HFIR	760	50	[126]
9Cr-1MoVNB	HFIR	760	50	[125]
9Cr-1MoVNB-2Ni	HFIR	760	50	[125]
12Cr-1MoVW	HFIR	760	50	[125]
12Cr-1MoVW 91354	HFIR	760	50	[125]
12Cr-1MoVW-1Ni 3588	HFIR	760	50	[125]
12Cr-1MoVW-1Ni 3589	HFIR	760	50	[125]

Table 4.2: Experimental parameters and references used for the construction of Figure 4.10. Irradiations took place at the 88-Inch Cyclotron, Fast Flux Test Reactor (FFTF), Los Alamos Neutron Science Center (LANSCE) spallation source, Proton Irradiation Experiment (PIREX) accelerator, and the Experimental Breeder Reactor II (EBR-II). All tensile testing was conducted at room temperature.

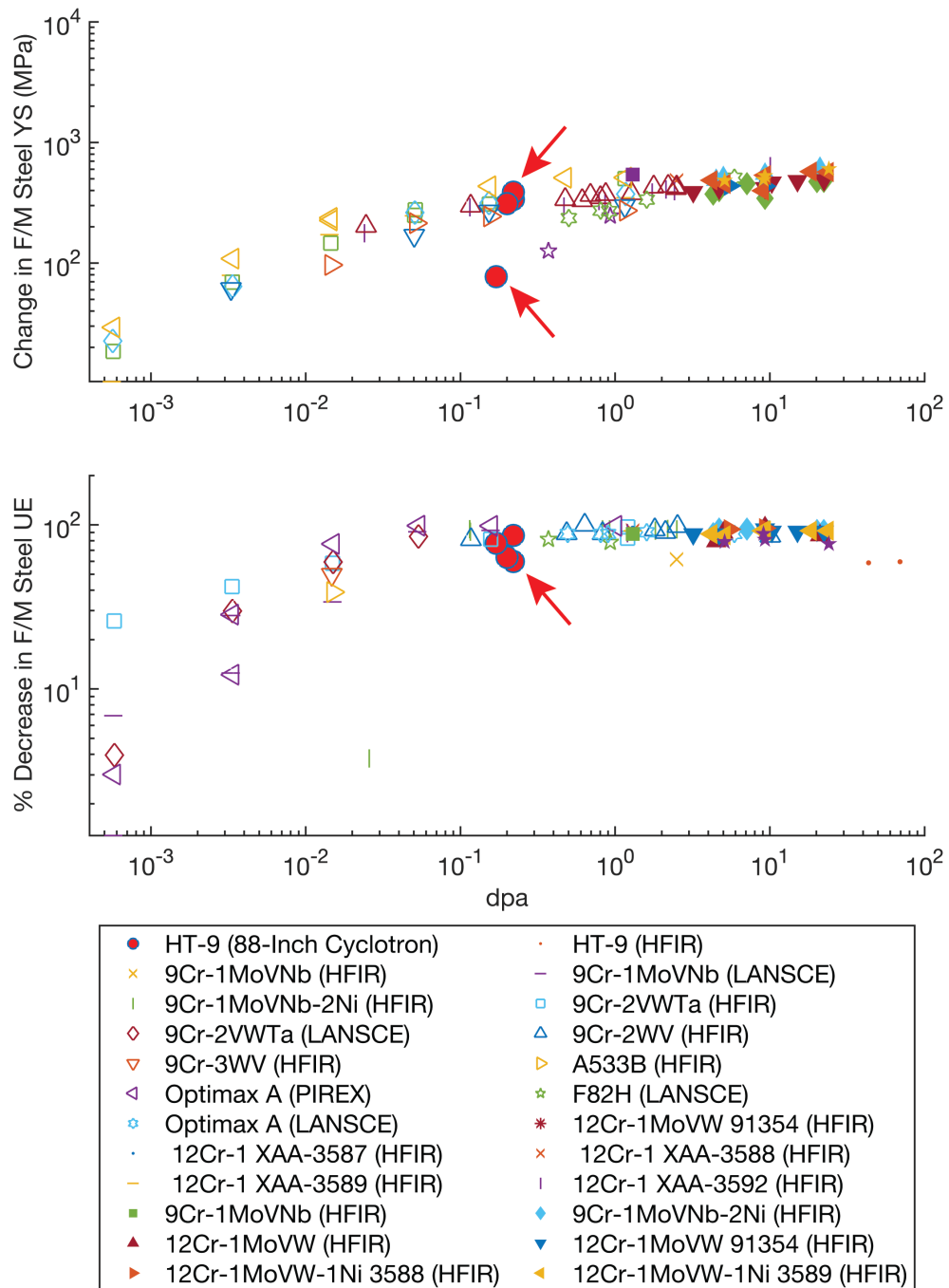


Figure 4.10: Change in high-Cr ($\geq 9\%$ Cr) F/M steel YS (ΔYS) and % decrease in UE with respect to dose after various low temperature (≥ 300 °C) irradiations. The data from this study is indicated by the arrows and fits well within the larger body of data obtained in previous works [89, 90, 91, 92, 125, 126].

doses of 0.0005 dpa and increases sharply until about 0.05 dpa [90], after which hardening continues to steadily increase until saturating around 10 dpa.

The barrier hardening theory was used to explore the radiation-induced increase in yield strength observed in this experiment, assuming the black dot defects are small dislocation loops:

$$\Delta YS = \Delta\sigma_{loop} = M\alpha\mu b\sqrt{Nd} \quad (4.2)$$

Where $\Delta\sigma_{loop}$ is the hardening contribution from dislocation loops (black dots), M is the Taylor factor, α is the barrier strength, μ is the shear modulus, b is the magnitude of the Burgers vector, N and d are number density and size of dislocations.

Here, the values for constants M , α , and b will be adopted from previous barrier hardening analysis on HT-9, where $M = 3.06$, $\alpha = 0.5$, $\mu = 82$ GPa and $b = 0.249$ nm [122]. From the TEM analysis, Nd was estimated as $1.6 \times 10^{14} \pm 10^{14}$ m⁻². As a result, ΔYS estimated by the barrier hardening model is 371 ± 142 MPa, while ΔYS measured for this sample was about 336 MPa. Moreover, ΔYS measured for all samples in other experiments, which were irradiated to similar doses, ranged from 77-387 MPa. Thus, the dislocation density estimates and subsequent barrier hardening calculation is within most of the measured ΔYS , especially for the lower bound of the error.

Farrell and Byun previously used models based on barrier hardening theory to describe some of the other body of data shown in Figure 4.10, revealing limitations of the model [90]. Farrell and Byun postulated the prominent change in the slope of the general trend around 0.05 dpa coupled with high necking strains indicates a change from the barrier hardening deformation mechanism to dislocation channel deformation [90]. Being our results fall in this slope transition region of the general trend, it is possible that barrier hardening may also be competing with dislocation channeling in our application, hence the lower bound of the dislocation quantification error generally being a better estimation of the ΔYS . However, no search for dislocation channels by TEM was made in this work.

The HT-9 data from this study fits well within the larger body of high-Cr F/M steel data, thereby providing merit for the 0.18–0.22 dpa irradiation and small-scale mechanical testing presented here. This study provides insight on the tensile properties of HT-9 as a function of gauge thickness and dpa. Previously, HT-9 tensile samples have been irradiated in reactors for long durations (e.g. 18 months [94]) and required hot cells for post-irradiation analysis and mechanical testing [87, 94]. The use of the 88-Inch Cyclotron alongside miniature SS-J tensile samples can supplement these neutron irradiations by achieving a desired dpa using deuterons. The small tensile sample size and ability to shape the ion beam to the tensile sample gauge length yields less irradiated volume and therefore less radioactive material. This method has potential for rapid turnaround experiments on irradiated tensile sample mechanical testing on a variety of materials and using a variety of ions. However, it is worth noting that dpa achieved in an accelerator (10–30 days) may have a different mechanism than dpa achieved in a reactor, (2–6 months) as the dose rate is known to play an important factor in defect cluster size and number density [127, 128].

4.2.4 Conclusions on the Preliminary High Energy Ion Implantation Study at the 88-Inch Cyclotron

In this work we utilize the LBNL 88-Inch Cyclotron to irradiate SS-J geometry tensile test specimens with 19-25 MeV deuterons. We also present an approach to quantify tensile properties as a function of gauge thickness, bringing about the potential to bridge length scale gaps. It was found that the low-temperature (<60 °C), low-dose (0.18–0.22 dpa) irradiation caused radiation hardening with an increase the YS of approximately 15–35% and decrease in ductility of about 75%, which is in good agreement with previous low-temperature high-Cr F/M steel experiments. An intermediate ductile/brittle failure mode was observed for all samples. As a result of the irradiation, black dot defects on the order of 6 ± 2 nm and $1.6 \times 10^{14} \pm 10^{14}$ m⁻² were observed, with the lower error bound yielding most reasonable Δ YS approximations by barrier hardening theory. Additionally, sample geometry effects on tensile properties were observed around 200 μ m gauge thickness for unirradiated samples. Future work should be conducted to confirm if these geometric effects are diminished by the 0.18–0.22 dpa irradiation. We have shown that the Cyclotron, coupled with benchtop tensile testing of radioactive samples, enables rapid-turnaround mechanical testing of nuclear structural materials.

4.3 Properties of a Helium Ion Beam Degradation System for the 88-Inch Cyclotron

The deuteron irradiation experiment described in Section 4.2 above successfully demonstrated the use of the 88-Inch Cyclotron to rapidly irradiate materials at the mesoscale for subsequent testing at UC Berkeley. Accordingly, we have designed additional beam instrumentation that would allow for uniform He implantation in mesoscale materials while monitoring and regulating sample temperature in-situ. Details of this novel ion beam degradation system are presented in this chapter. First, an overview of the design objectives are presented. Next, the design selection process is described, and the final system design is detailed. Then, the degrader controls system is specified. Lastly, future work is discussed.

4.3.1 Degradation System Design Criteria

The aim of the degrader is to stop He ions uniformly throughout the 100 μ m thick HT-9 SS-J geometry tensile test sample. Due to the stopping range profile of a monoenergetic beam of He ions, a degrader is needed to produce many discrete energy steps to implant He throughout the sample volume. The degrader should allow for the Bragg peaks of the stopping curves overlap throughout the sample depth, thereby resulting in “uniform” He implantation, as demonstrated in Figure 4.11.

23 MeV He is required to penetrate through 100 μ m of HT-9. For the Cyclotron facility, a maximum current of 20 μ A is assumed. Additionally, at least 0.5 at% He should be

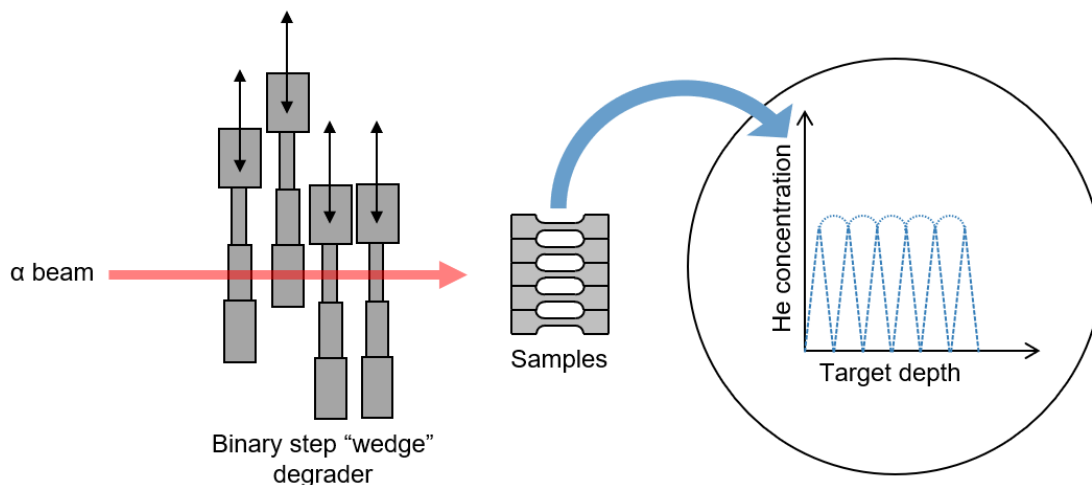


Figure 4.11: Conceptual overview of the He ion beam (α -beam) degrader. The monoenergetic ion beam passes through the degrader system, which results in a range of beam energies. The energy range of ions after passing through the degrader allows them to be implanted throughout the sample volume. For uniform implantation, the Bragg peaks should overlap throughout the sample depth.

achievable throughout the sample volume. Given these parameters, a significant amount of energy (100's of Watts) in the form of heat will be dissipated into the in-beam components. Thus, the in-beam components, including the ion beam degrader, should be water-cooled. The HT-9 samples should be sufficiently cooled to prevent heating over 300 °C to prevent annealing of radiation defects. The materials selection of in-beam components also consider radionuclide production.

For statistics purposes, multiple SS-J tensile test samples should be implanted in a single beam run. As shown in Figure 4.12(a), the minimum beam spot size required to implant 5 SS-J samples at once is $20 \times 5 \text{ mm}^2$. This dimension only considers the minimum beam spot required to implant the gauge length of SS-J samples. This is desired to promote fracture in the gauge length rather than the tensile sample shoulder or grippers. Additionally, the degrader system size is constrained to fit inside a $21.5 \times 28 \times 28 \text{ cm}^3$ beam box that is typical for beamline experiments at the 88-Inch Cyclotron. An image of a beam box is shown in Figure 4.12(b). Also, the degrader system must operate under 10^{-6} vacuum as a single unit with the beamline. Other important considerations include design simplicity and cost. In summary, the ion beam degrader must:

1. Produce a sufficient number of discrete energy steps for homogeneous implantation;
2. Provide sufficient (water) cooling for in-beam components and tensile samples;
3. Consider radionuclide production in the degrader components;
4. Implant 5 samples at once; $20 \times 5 \text{ mm}^2$ beam spot size;
5. Be compact; fit in a $21.5 \times 28 \times 28 \text{ cm}^3$ beam box;
6. Be vacuum compatible.

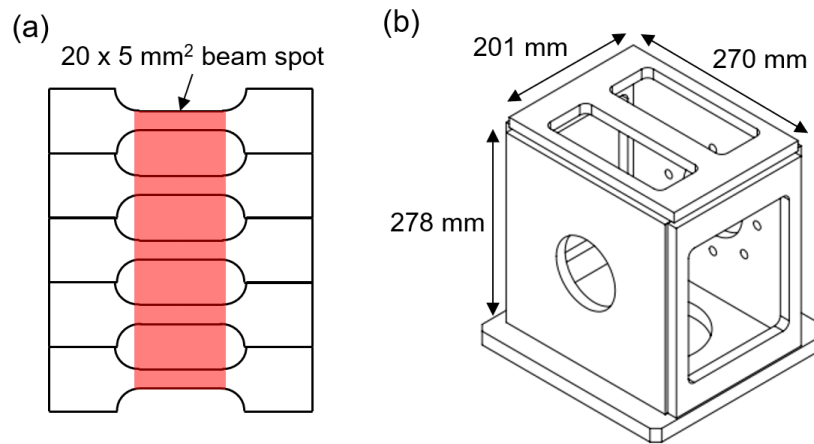


Figure 4.12: Details of size parameters influencing the degrader design. (a) The minimum beamspace size to implant the gauge lengths of 5 SS-J geometry tensile samples is $20 \times 5 \text{ mm}^2$. (b) The degrader is constrained to a $21.5 \times 28 \times 28 \text{ cm}^3$ Cyclotron beam box. Vacuum-sealed flanges may be coupled to the beam box to increase this space.

4.3.2 Degrader Design Selection

To meet the criteria described in section 4.3.1 above, there are two primary elements of the degrader design selection process: (1) mechanical design selection and (2) materials design selection. These elements were considered in parallel during the design selection process, and are discussed separately below.

4.3.2.1 Mechanical Design Selection

Several degrader designs were considered, the first being a novel “stippled target” degrader. This design was intended to be a stationary target that could simply be placed at the front of the beamstop target stack used in the preliminary experiment described in Section 4.2. and shown in Figure 4.4. At this point in the design process, the ideal stippled target material was determined to be Si or SiC (see Section 4.3.2.2. below for details).

The premise of the stippled target degrader, shown in Figure 4.13, is to use angular trenches, such that where there is a maximum volume of material, the ions do not penetrate as far, and are stopped at the front of the sample. Conversely, where there is a minimum volume of material, the ions penetrate further, and are stopped at the back of the sample. SRIM-2013 simulations showed the ions stopped at the back of the sample had the least radial straggling. To implant He laterally throughout the sample, the stippled target geometry was designed with the trench opening equivalent to the minimum straggling radius. Table 4.3 and corresponding Figure 4.13(c) provide the stippled target trench geometries, determined using SRIM simulations, for a variety of target configurations.

It should be noted that while the stippled target design may produce a number of discrete He energy steps, this design concept presented as-is would not provide uniform He implantation throughout the sample volume. One idea to avoid He concentration bands was to have the stippled target mechanically pivoting in front of the samples. However, this idea was not pursued.

The primary reason the stippled target design did not move forward was due to machinability of the trenches. Machining studies were conducted on SiC using a femtosecond laser. Initial studies, not at the scale required, were conducted to investigate the feasibility of this technique. Due to material redeposition, the resulting trenches did not reach the depths programmed in the laser microfabrication software. Subsequent studies varying the gas type and pressure revealed that Ni gas most effectively prevented SiC redeposition in comparison to Ar + 3% O or He gas, and increasing gas pressure had diminishing returns. Additionally, longer cutting speeds during machining and ultrasonic cleaning in an ethanol bath after machining was found to improve the trench quality. Despite these improvements, it was not possible to machine trenches with the required geometry. Alternative machining methods including photolithography-etching were considered but not pursued.

SiC min (μm)	SiC max (μm)	Be (μm)	HT9 (μm)	He ion beam energy (MeV)	Straggling radius of SiC max (μm)	Design angle (deg)
1000	2150	500	300	85	367.5	9.7
500	1300	500	300	65	251.25	11
300	550	0	100	35	54.1	5.6
300	1200	0	300	55	187.5	8.9
300	525	1000	100	60	203	21.1
300	1225	1000	300	75	315	14.4

Table 4.3: Stippled target design parameters for a variety of target stacking configurations. The parameters are described visually in Figure 4.13(c). The He ion beam energy and straggling radius was determined by SRIM-2013 simulation.

Several reported degrader designs were also considered, including a rotating wheel, sliding wedges and plates, and a binary degrader, as shown in Figure 4.14 [129]. In addition, two other novel degrader designs were considered: a binary step-wedge degrader and a cassette

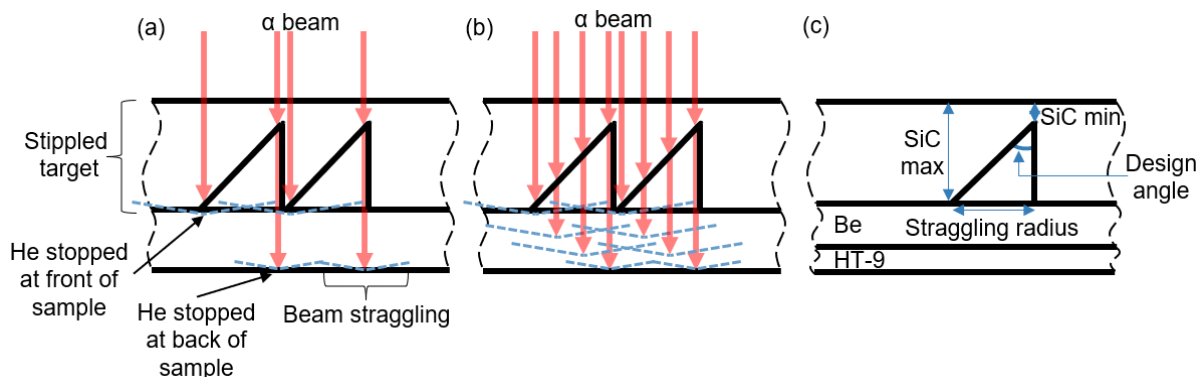


Figure 4.13: Conceptual overview of the stippled target degrader. (a) Represents the beam passing through the region of the stippled target with most material and with the least material. The beam passing through the most stippled target material will be stopped at the front of the sample and have more beam straggling. The beam passing through the least stippled target material will be stopped at the back of the sample and have the least beam straggling. The smallest beam straggling radius determined the spacing of the stippled target trenches. (b) Represents how the He beam profiles have some overlap throughout the sample depth. Yet, the stippled target design proposed would result in concentration bands of He. Additional design changes are necessary for uniform He implantation in the sample. (c) Description of stippled target parameters described in Table 4.3.

degrader. In the binary step-wedge concept, which was shown in Figure 4.11, each step is a different thickness, and each wedge moves linearly. When the wedges are aligned, they produce an overall thickness for energy degradation. The cassette degrader concept is similar to that of the plates with “binary” thickness shown in Figure 4.14, except the plates would be in a frame with cooling on three sides, and instead of moving horizontally (left-right) into the beam, they would move vertically (up-down) into the beam.

A design matrix was produced in order to inform the mechanical design decision. This is shown in Table 4.4 for the modulator wheel, wedge, step-wedge, and cassette degrader designs. Although the wheel degrader had been implemented before [130, 131], it was found to produce too few discrete energy steps, be too large, and be complex to cool. For example, the maximum size modulator wheel that could fit in the required beam box is 13 cm in diameter. Considering a $20 \times 5 \text{ mm}^2$ beam spot size, a 13 cm diameter wheel could only provide 16 energy steps. One way to increase the number of energy steps is to have modulator wheels in parallel. It would require 13 parallel wheels to provide >206 discrete energy steps (206 is the number of energy steps the selected design provides). Alternatively, a single modulator wheel providing 206 energy steps would have to be 1.6 m diameter. Thus, the modulator wheel was an unfavorable design choice from a number of energy steps and a degrader size perspective. Moreover, removing the heat from the edge of the rotating wheel(s) in vacuum is non-trivial. The wedge design was also presumed to be difficult to cool in vacuum, and lacked flexibility in comparison to designs with interchangeable degrader filters. The cassette design would provide for efficient cooling and experimental flexibility, but the novelty and complexity of the cassette design would require significant effort to implement.

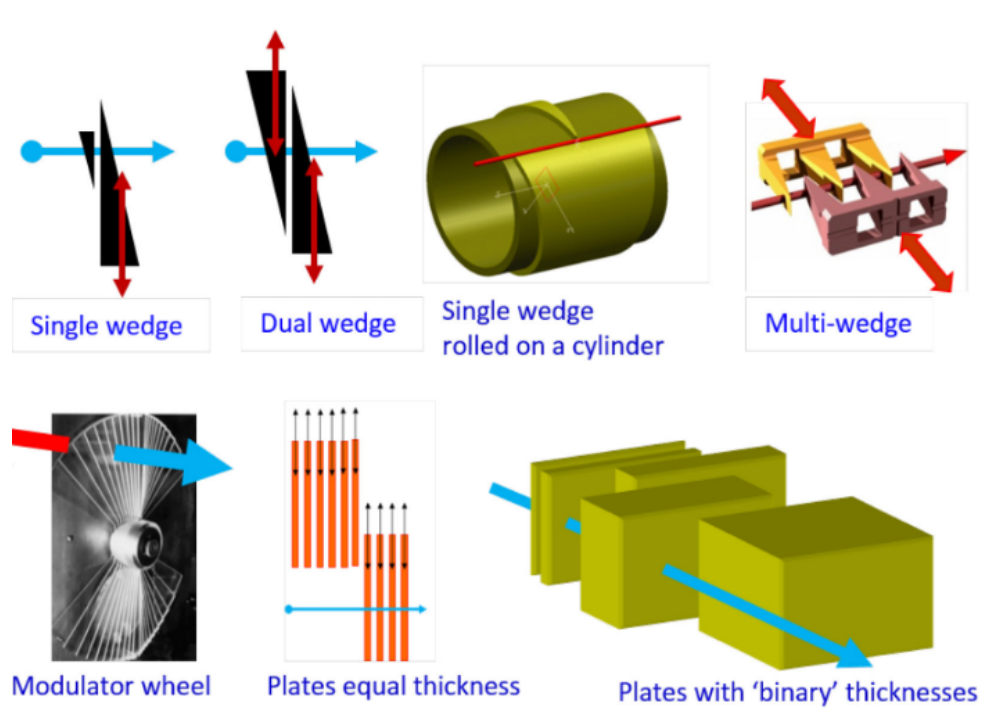


Figure 4.14: Some of the possible degrader designs from literature that were considered, reproduced with permission from [129] under the Creative Commons copyright license CC BY-NC-SA 4.0.

Of the degrader designs considered, the novel binary step-wedge was selected. The binary step-wedge degrader was found to be the most space, cost, and heat transfer efficient for our application. As shown in Figure 4.15, the binary step wedge degrader meets the size constraints, with (a) accommodating a beamspot size of $20 \times 5 \text{ mm}^2$ for implanting 5 samples at once and (b) a footprint of $15 \times 11 \times 13 \text{ cm}^3$ allowing it to fit in the beam box. Moreover, the degrader filters can each be cooled on 2-3 sides and loosely held to account for thermal expansion. The degrader filters can also be easily changed in this design, enabling a variety of implantation campaigns.

The initial binary step-wedge degrader design concept considered filters diced from 4 different wafer thicknesses, which was more cost efficient than purchasing 12-16 Si/SiC filters in different thicknesses. An optimization code determined that wafer thicknesses of 38, 40, 46, and 53 μm provided the maximum amount of linear combinations. The degrader filter arrangement is shown in Figure 4.16(a). The thickest filters are moved to the edge, to allow for cooling on three sides, since they are the filters absorbing the most energy. Figure 4.16(b) shows the hundreds of discrete energy steps this degrader design with the filter arrangement can provide. The linear region in 4.16(b) is in 1 μm steps. For implanting the 100 μm thin HT-9, only 206 of these combinations are needed, and can be selected within the linear (150-413 μm) range. A few of the stopping curves in HT-9 for these filter thicknesses are shown in Figure 4.16(c). 29 MeV He is used because that is the maximum energy required

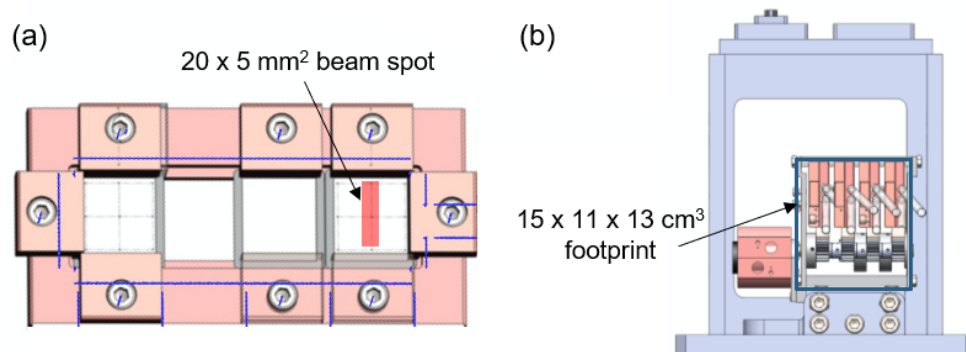


Figure 4.15: The binary step-wedge degrader meets the size constraints. (a) Top-down view of a degrader wedge, which holds up to 4 filters. The filters are large enough for the 20 × 5 mm² beam spot. (b) The degrader step-wedge assembly and motors have a footprint of 15 × 11 × 13 cm², which is small enough to fit in the standard LBNL beam-box.

to penetrate the minimum degrader filter thickness of 150 μm Si and the back of the HT-9. Only every ~50 μm Si is plotted in Figure 4.16(c), however, if every 1 μm step were plotted, there would be significant overlap of the Bragg peaks.

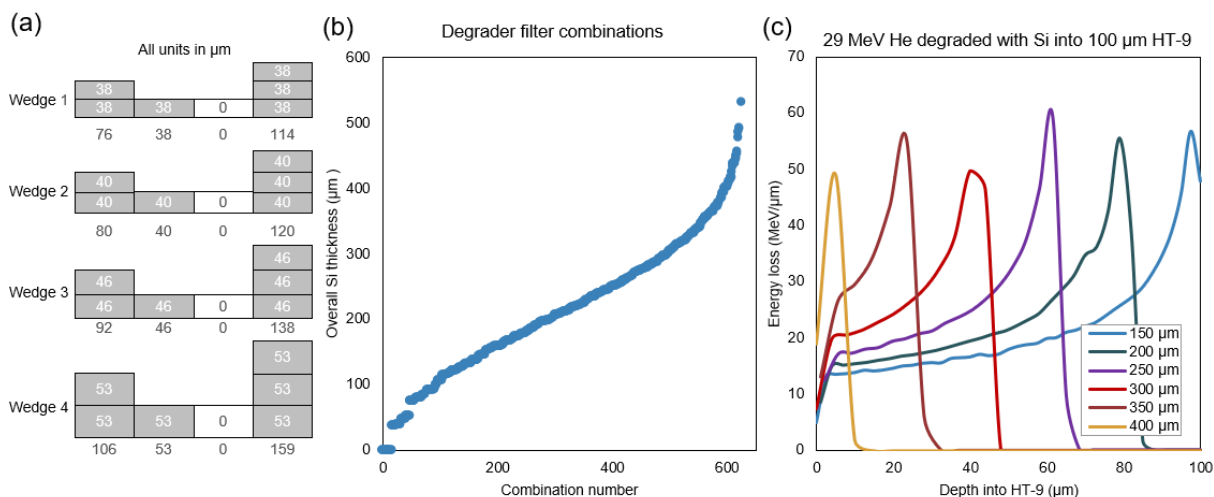


Figure 4.16: The binary step-wedge degrader design provides 625 of discrete energy steps. For cost efficiency, the number of filter thicknesses was minimized. An optimization code was ran, determining that by stacking filters to create an overall thickness, as shown in (a), 38, 40, 46, and 53 μm thick filters can provide the most linear combinations for energy steps. (b) The number of combinations (energy steps) that can be made with the wedges show in (a). The most linear region is 1-2 μm steps. (c) From the degrader filter combinations shown in (b), the most linear region (starting at 150 μm overall Si thickness) is used. It was determined that 29 MeV He and a range of 150 to 413 μm Si is needed for implanting 100 μm HT-9. This region contains 206 combinations and therefore provides 206 energy steps. Of these 206 energy steps, the Bragg curves of only 6 (every ~50 μm) were calculated using SRIM and are plotted here. Since the actual steps are 1-2 μm, there would be a significant amount of overlap if all of the steps were plotted.

4.3.2.2 Materials Design Selection

The evaluation of potential degrader filter materials was another important component of the design selection. A design matrix was also used for the material selection and is shown in Table 4.5. The filter material should not produce long-lived radionuclides which may restrict beam cave access and/or sample retrieval for an extended period of time. Also, the material should be low density, because the higher the material density, the higher the He energy that would be required, and therefore the more thermal energy that would be dissipated into the in-beam components. Moreover, the material should have high thermal conductivity, in order to have efficient heat transfer. A low coefficient of thermal expansion is also desired, because the filters would be clamped in place and significant thermal expansion could lead to material failure. Additionally, a high melting temperature was needed such that the filters would not melt under the 100's of Watts of beam energy. It was also important to assess the availability to machine thin (10's of μm) filters, since larger thicknesses would also require higher beam energy and therefore more heat dissipated into the system. An additional concern in the material selection was the cost. It must be noted that properties such as the thermal conductivity were taken from reported bulk properties, while the thin-film properties might vary significantly.

Based on this material selection criteria, Si was selected for the degrader filters. One of the primary reasons for selecting Si is the use of wafer manufacturing to fabricate the Si filters. The filter size needed is $20 \times 30 \text{ mm}^2$. 7 of these filters can be produced on a single 4-inch wafer, allowing for 1 spare filter per wafer. The 4 wafers were polished to the 4 different thicknesses (38, 40, 46, and 53 μm) determined by the aforementioned optimization code, and then diced to the desired dimensions. One major concern with thin Si of these geometries is breakage, especially when removing the die (filters) from the wafer dicing tape. Thus, the specification to the manufacturer required the die to be removed from the dicing tape.

	Wheel		Wedge		Step-wedge		Cassette	
	Pros	Cons	Pros	Cons	Pros	Cons	Pros	Cons
Concept and Cooling	Rather simple	1 side cooling	Simplest	2 sides cooling	Simple	2-3 sides cooling Can add wedges, but would need more wafers	3 sides cooling	Complicated
Improve cooling	Speed up (to a limit)	Heat transfer	Add more wedges	Need more wafers	Optimize software		Cu to cold Cu	Individual filter cooling is complicated
Engineering	Done before	Big space needed	Done before	Medium space	New - easy assembly maintenance	Medium space	Small space	Novel
Water system	More speed - less heat	Coolant rotates - complicated	More wedges - less heat	Coolant to each wedge	More wedges - less heat Can use 4 individual steps	Coolant to each wedge	Coolant to cassette box	Coolant by conduction
Filters	16 individual steps	No overlaps - gap	Constant step change	Needs two wedges			4 steps	Smart controller needed
Stresses	Less stresses	1 side cooling	Medium stresses	If breaks, need to replace all	No stresses	Single wafer can be replaced	No stresses	Brazing development
Moving mechanism	Rotate by motor		Mechanical arrangement	Some complication	Mechanical arrangement	Some complication	Durable	Complicated mechanism
Si/SiC filter manufacturing costs	1 wafer/thickness Total of 16 \$325/ea \$5,200/total	16 wafers in different thickness	1 wafer for each wedge Total of 4	Angle polish	38 μm thin Need 4 wafers 7 di per wafer \$3,100/total		38 μm thin Need 4 wafers 7 di per wafer \$3,100/total	

Table 4.4: Mechanical design matrix for the wheel, wedge, step-wide, and cassette degrader designs. The following were taken into consideration: the ability to cool the degrader filters; the simplicity of the physical design and water system; the number of different thickness filters needed; the mechanical stresses on the filters due to how they would be held and thermal expansion; the mechanical mechanism for movement; and the filter production costs. The green/red indicates pros/cons that were heavily weighted. As a result, the step-wedge degrader design was pursued.

	Radionuclide production*	Low ρ (g/cm ³)	High k (W/mK)	Low α (10 ⁻⁶ m/m°C)	High T _m (°C)	Machinability/thin foils availability	Cost
Ti	V-48 (t _{1/2} = 16 d) ~16 MeV Sc-46 ~35 MeV Cr-51 ~7 MeV	OK (4.5)	N (17)	Y (8.64)	Y (1,668)	Difficult to machine, can find ≥2 μm thin foil	\$1,147/foil
Cu	Zn-65 cxn relevant ~16 MeV Co-58 ~44 MeV Co-57 ~60 MeV	N (8.96)	Y (385)	N (17.6)	Y (1,085)	Difficult to machine, can find 38 μm thin foil	\$151/foil
Al	Na-22 cxn relevant ~70 MeV	Y (2.7)	Y (205)	N (~23)	N (660)	Easy to machine, can find nanofoils via CVD	\$90/foil
Be	Be-7 ~20 mb @ 85 MeV	Y(1.85)	Y (200)	OK (12)	Y (1,287)	Can only machine at a specialty shop, Can find ≥5 μm thin foil	\$2,132/foil
W	-	N (19.3)	Y (173)	Y (4.5)	Y (3,422)	Difficult to machine, can find 50 μm thin foil	\$52/foil
SiC	Be-7 25 mb @ 55 MeV C-14 27 mb @ 27 MeV Be-10 cxn relevant 55 MeV	Y (3.21)	Y	Y (2.77)	Y (2,730)	Difficult to machine, can use MEMS techniques, can find 38 μm thin foils	\$110/foil
Si	-	Y (2.3)	Y (149)	Y (5.04)	Y (1,414)	Difficult to machine, can use MEMS techniques, can find 38 μm thin foils (and thinner with frame)	\$67/foil
Graphite	Be-7 ~25 mb @ 55 MeV C-14 ~27 mb @ 27 MeV Be-10 cxn relevant ~55 MeV	Y (2.26)	Y	Y (4-8)		Y	-

Table 4.5: Design matrix for the filter material selection. *Radionuclide production data was found using JANIS [132]. Only nuclides with half-lives (t_{1/2}) longer than a couple of days are listed. Up to 85 MeV α's were considered. The filter material should have a relatively low density (ρ), high thermal conductivity (k), and high melting temperature T_m. "Y" refers to yes, and "N" refers to no. It should be noted that these properties are for bulk and may not translate to thin film properties. Additional considerations include the ability to machine the material and the ability to find commercially available thin foils. Suppliers were identified and an initial cost comparison was conducted. Boxes highlighted in red indicated negative weighting factors. Graphite is in red because the carbon will diffuse into our samples, so this material cannot be used. As a result of this weighting matrix, Si and SiC were determined to be the ideal filter materials.

4.3.3 Degradation System Design

A schematic of the complete degrader system design assembly is shown in Figure 4.17. There are three primary sub-assemblies in overall system: the collimator, binary degrader, and beam stop. The degrader beam box is connected in-line with the cyclotron beamline. The ion beam will first be incident on the collimator before being degraded and finally implanted in the samples.

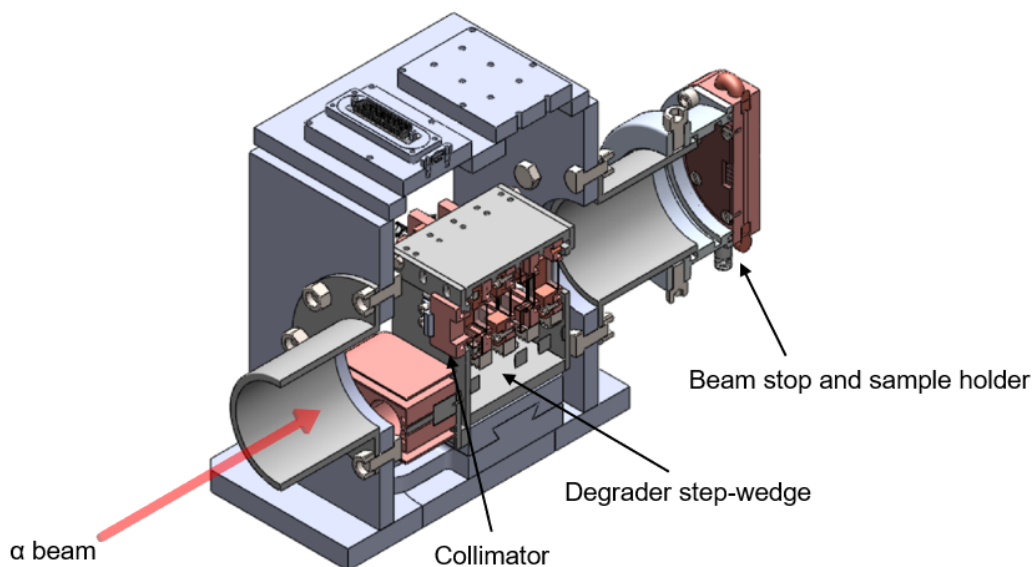


Figure 4.17: Overview of the complete degrader assembly. The degrader box is connected to the cyclotron beamline and the entire system is under vacuum. The α (He ion) beam is first incident on the collimator, where it is flattened and shaped. Then, the beam is degraded, resulting in a range of energies for implantation in the samples. The samples are held in the beam stop and sample holder assembly, which is connected to the degrader box with a flange.

The collimator is used in front of the degrader system to ensure a flat and diffuse beam with the desired spot size is incident on the degrader filters. The collimator is made out of OFHC (oxygen-free, high-conductivity) Cu, and contains a water cooling channel, as shown in Figure 4.18. The collimator also has ports for thermocouple instrumentation to measure its heating during operation. Additionally, the collimator is easily interchangeable since it is clamped onto the front of the degrader box with screws. It is desirable to be able to change the collimator in order to support a variety of experimental configurations. Currently, the collimator opening is designed for implanting 5 SS-J samples. However, if less samples are implanted, then the beam spot size can be decreased, which will increase the current per sample, and therefore decrease the time needed to achieve a certain atom percent (at%) of He in the samples. Figure 4.19 shows the irradiation time to achieve various concentrations of He in HT-9 depending on the beam current and beam spot size (collimator configuration).

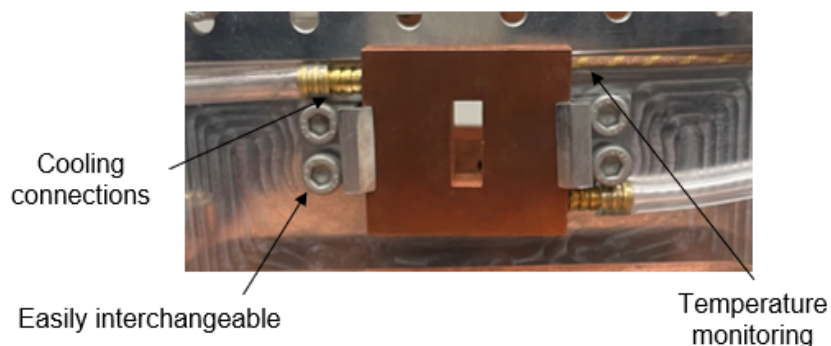


Figure 4.18: Image of the collimator assembly on the front of the degrader box (not the beam box). The collimator is made out of OFHC Cu for effective heat transfer. A water cooling channel runs through the collimator, with an inlet and outlet connection. The collimator is instrumented with a thermocouple to monitor its temperature. Additionally, the collimator can easily be changed to adjust the beam geometry.

The step-wedge sub-assembly is shown in Figure 4.20(a)-(d). The degrader filters are attached with OFHC Cu holders and spring washers to a moment. Since there is a slight gap between the thin filters and the Cu holders, Cu foil is used to help keep the filters in place and in good thermal contact. The degrader wedges are made out of OFHC Cu and contain a water cooling channel throughout the entire frame, as shown in Figure 4.20(a),(b). The filters are held somewhat loosely in order to account for thermal expansion, and the thickest filters (stacked with 2-3 foils) are held on the outer slots in order to allow for cooling on 3 sides and thus remove heat more efficiently. The wedges and filters are instrumented with thermocouples, to monitor the filter temperature during operation and ensure they are effectively cooled.

To perform the linear wedge movement, each wedge is housed on an individual steel rack and driving pinion, and connected to an individual DC brush motor. Zero microswitches are used for each wedge to prevent drifting of the linear movement. Since the motors are to be used in-vacuum, a water-cooled jacket was made out of pure OFHC Cu, shown in Figure 4.20(c). The motors cooling jacket is instrumented with thermocouples to monitor and prevent overheating, at which point the motor function would significantly decline.

The beamstop and sample holder sub-assembly is shown in Figure 4.21. A short tube connects the beam stop sub-assembly to the beam box. The samples are clamped with OFHC Cu. The clamp doubles as a mask, which covers the sample shoulders and grippers in order to promote the desired tensile failure in the gauge length. Additionally, the Cu mask opening is angled, in order to prevent a shadowing effect on the samples. The beamstop contains water cooling channels and thermocouple instrumentation for monitoring the sample temperature and water temperature.

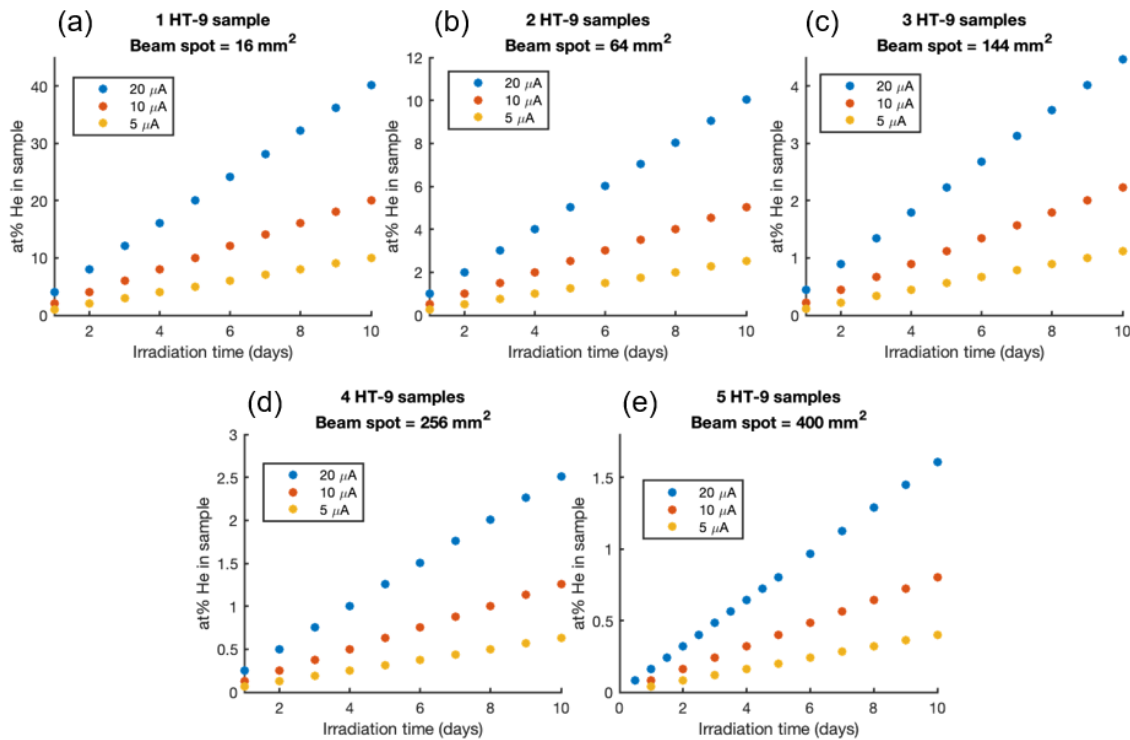


Figure 4.19: Time to achieve at% He in a single SS-J sample. The experimental configurations considered at (a) 1, (b) 2, (c) 3, (d) 4, and (e) 5 HT-9 SS-J sample(s), as well as incident beam currents of 5, 10, and 20 μA . These graphs show that when the number of samples, in the implantation decrease, we can decrease the beam spot size. This increases the beam current incident on each sample, and therefore decreases the time required to achieve a specific at% He. The interchangeability of the collimator can accommodate different beam spot sizes and thus different beam time requirements. Additionally, the graphs also show the time to achieve an at% He decreases with increasing cyclotron beam current.

4.3.4 Uniformly-Distributed System Energy Balance

The main safety concern of the degrader system is one of the in-beam components approaching a temperature limit. Simulations were conducted and code was developed to estimate how much power (W) is deposited in each component. The temperature was not calculated, and power radiated out of the system was not considered. First, SRIM-2013 was used to calculate the energy loss, dE/dx , in the first component in the beamline. Then, python was used to integrate under the dE/dx curve to calculate the energy stopped in the component. A cumulative trapezoidal integration method was used for this step. The result of the integration is how many MeV was stopped in the component, and this value was used to inform the SRIM simulation for the next component. That is, subtracting the “MeV in” from the “MeV stopped” gives “MeV out.” The “MeV out” will be the “MeV in” for the next component in line. To calculate the thermal power in W absorbed by each component, the energy stopped in MeV is multiplied by the beam current incident on each component. There are unaccounted for errors in rounding the MeV and in the integration approximation.

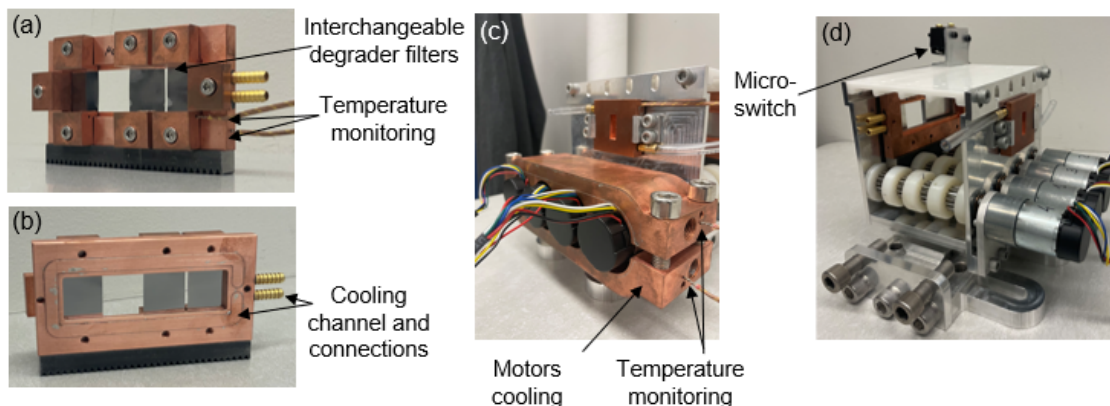


Figure 4.20: Detail of the degrader step-wedge sub assembly. (a) One of the step wedges assembled with filters. The step-wedge is made out of OFHC Cu. The filters are loosely held to allow for thermal expansion. The filters are also easily interchangeable for experimental flexibility. The “worst-case” wedge, being the wedge with the thickest filters, is instrumented with two thermocouples to measure both the thickest filter and the wedge base temperature. (b) There is a cooling channel that runs through the entire wedge and barbed inlet/outlet connections. (c) Since the motors are used in vacuum, it is imperative that they are cooled. A motors water-cooling jacket was made out of OFHC Cu. The motor cooling jacket is thermocouple instrumented. (d) One of the degrader wedges and zero microswitches, along with the full motors and driving shafts and pinions. Also shown is a custom x-y stage to position this degrader box in line with the beam.

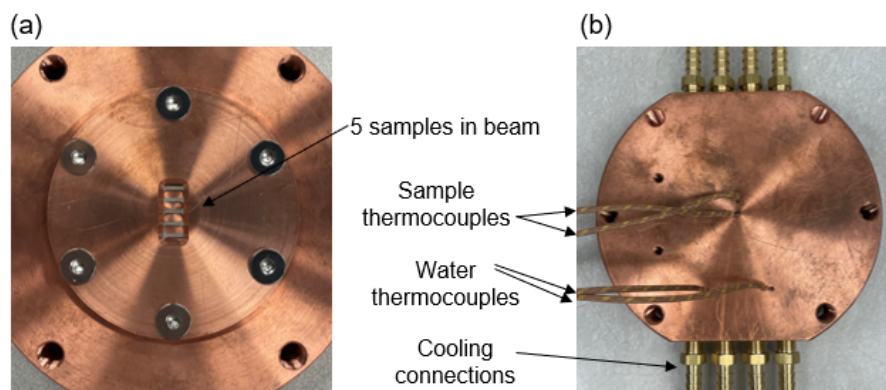


Figure 4.21: (a) Front and (b) back view of the beam stop assembly, which is made out of OFHC Cu. (a) 5 SS-J samples clamped in place. The clamping mechanism also performs as a mask. The opening is tapered to prevent shadowing. (b) The beamstop has water cooling channels throughout and is instrumented with thermocouples for monitoring the sample and water temperatures.

Table 4.6 shows the energy (MeV) and power (W) absorbed by each component, for the thinnest filter (150 μm) case. Meanwhile, Table 4.6 shows the energy (MeV) and power (W) absorbed by each component, for the thickest filter (413 μm) case. Both cases considered the highest incident beam current of 20 μA and an initial beam energy of 29 MeV, and thus an incoming beam power of 580 W. The beam current varies based on the component geometry. The collimator will always absorb a significant amount of beam. In the thin filter

	Energy in (MeV)	Current in (μ A)	Energy stopped (MeV)	Energy out (MeV)	Power Stopped (W)
Cu collimator	29.0	12.2	29.0	0.0	353.8
150 μ m Si	29.0	8.0	6.4	22.6	51.6
HT-9 Sample	22.6	1.20	21.0	1.6	25.2
Beamstop					149.4

Table 4.6: Energy balance for the thinnest degrader filter (150 μ m) configuration, assuming 29 MeV He and 20 μ A current into the system. The majority of the thermal power is dissipated in the collimator and the beamstop.

	Energy in (MeV)	Current in (μ A)	Energy stopped (MeV)	Energy out (MeV)	Power Stopped (W)
Cu collimator	29.0	12.2	29.0	0.0	353.8
413 μ m Si	29.0	8.0	27.8	1.2	222.2
HT-9 Sample	1.2	1.20	0.8	0.4	1.0
Beamstop					3.0

Table 4.7: Energy balance for the thickest degrader filter (413 μ m) configuration, assuming 29 MeV He and 20 μ A current into the system. The majority of the thermal power is dissipated in the collimator and the filter.

case, the beamstop will absorb a significant amount of thermal power as well. This is due to streaming of the beam in the areas where the samples do not cover, and due to this initial experiment being designed to slightly “overshoot” the HT-9 sample, and thus some beam will come through the back of the sample. For the thick filter case, the filter absorbs a significant amount of thermal power, and the power absorbed in the beamstop is only through the gaps where the samples do not cover the beamstop.

The degrader system energy balance reinforces the premise that the degrader system components will absorb a significant amount of thermal energy. This demonstrates the importance of ensuring all the components are efficiently water-cooled, have good thermal conductivity and a high melting temperatures, are instrumented with thermocouples, and that the controls system enforces effective temperature limits.

4.3.5 Degradar Controls

Connection and controls are important aspects of the degrader design and implementation. The controls software user interface was developed using LabVIEW. The system microcontroller is programmed using Arduino to control various hardware components based on the serial port input from LabVIEW. The degrader controls system serves 4 overall functions, which will be described in more detail in the following sections:

1. Control the motors movement according to an input table;
2. Safety control (provide an emergency shutdown response);
3. Record experiment parameters;
4. Run a graphical user interface (GUI).

4.3.5.1 Motors Control

To achieve 100's of discrete implantation energy steps, we use 4 wedges (water cooled filters holder), each installed with 4 thicknesses of filters. The wedges are linearly moving in sequence. The software controls the movement of the 4 individual wedges in front of the beam. Each wedge has an individual motor with an encoder and can assume 4 possible linear positions. The linear movements to these positions is precise, with a tolerance of 2 mm (10%). The software can set zero by the microswitch at one end of each rail.

It is desirable to turn the beam off between degrader positions. This prevents streaming through gaps, and prevents a non-discrete energy step. The beam chopper can turn the beam completely off within μs . The beam on and off function is initiated by a 5 V and 0 V TTL signal, respectively. The movements should be at the maximum speed and dwell time for beam off (e.g. 0.1 to 0.5 sec).

The controls software reads through a table of positions for each wedge, and translates it to motor movements. The table is simply uploaded through the LabVIEW GUI. An optimization code was written for the position table, such that no filter is in the beam twice in a row. This allows for maximum cooling of the filters. A copy of the position table is shown in Appendix B. The positions are numbered 0, 1, 2, and 3. The table line order is kept such that once it has gone through the entire table, it jumps to the top of the table and starts reading it again without delay.

4.3.5.2 Safety

The degrader system is instrumented with thermocouples and flow meters, which are logged by the controls software. The controls system has built-in safety features. The system will emergency stop if any of the following occurs: any temperature reads above the limits, the flow meter is not within the limits, the motor stalls for more than the time limit, and/or the zero microswitch does not respond where it should. In some cases, there is more than a single limit. For instance, low water flow might cause heating, while high water flow indicates a hose break and water leak. Some limits are only for alert but not a showstopper.

Table 4.8 provides a full list of safety and operational inputs and outputs (I/Os) for the degrader system, including individual limits. In case of reaching one of the limits, the degrader system will shut down, which stops the motors, turns the beam off, and stops the water via a solenoid valve. A GUI alarm will also arise so users may know that an emergency shutdown situation has arisen. Additionally, details of the emergency shutdown are written to the output log file.

Category	Input	Output	Limit	Comments
Safety	Sample thermocouple 1 (below)	Data collection trigger Beam on/off Alarm	300 °C	Low threshold for alarm: 200 °C
Safety	Sample thermocouple 2 (beside)	Data collection trigger Beam on/off Alarm	300 °C	Low threshold for alarm: 200 °C
	Beam stop inlet water thermocouple			For the records only
Safety	Beam stop outlet water thermocouple	Data collection trigger Beam on/off Alarm	60 °C	Low threshold for alarm: 30 °C
Safety	Wedge thermocouple 1 (base)	Data collection trigger Beam on/off Alarm	60 °C	Low threshold for alarm: 30 °C
Safety	Wedge thermocouple 2 (holder)	Data collection trigger Beam on/off Alarm	60 °C	Low threshold for alarm: 30 °C
Safety	Motor thermocouple 1	Data collection trigger Beam on/off Alarm	100 °C	Low threshold for alarm: 50 °C
Safety	Motor thermocouple 2	Data collection trigger Beam on/off Alarm	100 °C	Low threshold for alarm: 50 °C
Operational	Micro switch 1 (wedge 1)	Zero		First filter at position
Operational	Micro switch 2 (wedge 2)	Zero		First filter at position
Operational	Micro switch 3 (wedge 3)	Zero		First filter at position
Operational	Micro switch 4 (wedge 4)	Zero		First filter at position
Operational/safety	Encoder 1	Controls motor 1 position	2 sec	In case of 2 sec stall - shut down
Operational/safety	Encoder 2	Controls motor 2 position	2 sec	In case of 2 sec stall - shut down
Operational/safety	Encoder 3	Controls motor 3 position	2 sec	In case of 2 sec stall - shut down
Operational/safety	Encoder 4	Controls motor 4 position	2 sec	In case of 2 sec stall - shut down
Safety	Flow meter 1 (wedge system)	Data collection trigger Beam on/off Alarm Water shut down	5LPM > FR > 10	Low = overheat High = water leak
Safety	Flow meter 2 (motors system)	Data collection trigger Beam on/off Alarm	5LPM > FR > 10	Low = overheat High = water leak

Table 4.8: Complete list of inputs and outputs of the software, as well as corresponding limits warranting a warning alarm and/or emergency shutdown.

4.3.5.3 Experiment Parameters

The LabVIEW software writes the data to a delimited file so the experimental parameters are recorded. It is important that details of the experiment be written to a file for post-experiment analysis. The log file is also accessible in real time, so that it can be checked during the experiment.

4.3.5.4 Graphical User Interface

A live view of the experiment parameters is displayed via a GUI. The GUI includes a motors on/off button, alarm on/off button, and a motors emergency stop button. Additionally, it should display all thermocouple readouts, water flow rate meter readouts, and motor positions, so that the temperatures, cooling water, and motors can be readily monitored.

4.3.6 Conclusions and Future Work on the Degradation

A novel He ion beam degrader has been designed for future nuclear materials experiments at the 88-Inch Cyclotron. This degrader enables uniform He implantation in up to 5 SS-J geometry HT-9 tensile test specimens in a single beam run. The degrader configuration takes a monoenergetic beam and produces 100's of discrete energy steps, providing a homogeneous He distribution throughout the implanted material. The system has four water loops to sufficiently cool the collimator, degrader, motors, and samples. Additionally, component temperatures and water flow rates are monitored.

An initial safety review of the design was completed with LBL. For the subsequent review, an ex-situ heating experiment should be performed. In such an experiment, the collimator, "worst case" (thickest) degrader filter, and the beam stop should be heated while cooling systems operate and temperature response is measured. This should accompany a thermal numerical simulation. Upon this experimental validation of the simulation, the code should be ran with a "worst case" high beam energy and current scenario. This will help ensure the degrader filters do not overheat and the HT-9 samples do not go above the defined temperature limits. The thermal experiment and simulations should be presented to LBL in a follow-on safety review.

Once the degrader system is ready to be used in-beam, an experiment should be conducted to validate the degrader's ability to uniformly implant materials. Instead of a single layer of 100 μm thin HT-9, this should use a stack of thin (20 of μm) HT-9 foils. After 29 MeV He implantation with the degrader system running, the dose rate of each individual foil shall be measured. If the dose rates of each foil are the same, it can be presumed the implantation was uniform throughout the foil stack. Alternatively, a TEM investigation of each foil may be conducted, allowing for verification of uniform implantation by quantifying the radiation defects.

Chapter 5

Summary and Future Work

Current and future nuclear technologies present a number of materials research challenges. This thesis addresses He degradation in materials and sample size limitations in materials research irradiation campaigns. In nuclear technologies, He largely occurs from high energy (n, α) reactions and α -decay. He is insoluble in solids, and precipitates into bubbles. At high doses, He bubbles agglomerate, eventually leading to surface blistering. In small volume materials, He-induced swelling, hardening, and enhanced ductility has been previously reported. Meanwhile, He embrittlement and spall strength reduction has been reported in large-volume materials.

Surface effects resulting from low-energy (25-60 keV) He implantation in Ti and Cu were investigated. In Ti(0001), a HIM with a nm-size beam was used to rapidly produce local He implantations. AFM, nanoindentation, and TEM characterization revealed a linear increase in surface swelling with respect to dose, an inverse relationship between He dose and hardening, and inter-bubble fracture as the mechanism for surface blistering in Ti(0001). Additionally, the presence of He bubbles was observed to enhance “pop-in” behavior during nanoindentation. In order to definitively investigate if the He bubbles enhance dislocation nucleation in Ti(0001), in-situ TEM indentations should be performed in the future.

Comparative HIM implantation and blister indentation studies on Cu(100), Ti(10 $\bar{1}$ 0), and Ti(0001) showed Cu(100) blisters behaved elastically under loading (to a limit). The bubble structures associated with blistering in Cu(100) were large (\sim 287 nm diameter) and faceted. In contrast, He-induced blisters in Ti(10 $\bar{1}$ 0) and Ti(0001) deformed plastically under loading. Additionally, the bubble structures associated with Ti blistering were small (\sim 1 nm) and formed nanocracks leading to the inter-bubble fracture blistering mechanism. A blister in Ti(10 $\bar{1}$ 0) was indented until catastrophic failure. During this in-situ indentation, a blister adjacent to the indented one also failed, and a crack grew from the adjacent blister into the sample. A follow-on experiment is needed with a single blister in cross section in order to investigate its response to loading and verify whether crack growth is observed from the indented blister. Moreover, these investigations revealed a need for improved He blistering models as the bubble structures associated with blistering were found to be largely material-dependent.

PAS was used to supplement the TEM and swelling results for near-surface implantations. Broad beam, 60 keV He implantations for PAS were carried out at the LANL Ion Beam Materials Laboratory. Using PAS, we were able to quantify the increase in vacancy concentration and at increasing depths into the sample with respect to He implantation dose in cp-Ti, thereby validating the swelling and TEM results. An additional sample condition revealed that shock loading decreased the vacancy concentration in a sample containing He bubbles. Continued PAS analysis is needed to quantify the vacancy concentration with respect to dose across different materials and crystal structures such as Cu. Additional PAS work is also needed to further quantify the influence of shock loading on vacancy concentration in not-implanted and pre-implanted materials.

The majority of ion implantation campaigns use low energy implantations, such as those described in the beginning half of this thesis. The latter half of this thesis focuses on high energy ion implantation, which is less widely available. We intend to establish a new implantation capability which highlights the use of the LBL 88-Inch Cyclotron for materials studies. An initial high energy ion implantation campaign was conducted using high energy (19-25 of MeV) deuterons to irradiate HT-9 tensile test specimens at the LBL 88-Inch Cyclotron. The tensile test results revealed radiation hardening and agreed well with literature data. The development of an ion beam degrader for bulk-scale He implantation campaigns at the 88-Inch Cyclotron is also detailed. This tool will help fill significant gaps that currently exist in extrapolating small-volume properties to bulk-scale. Continued efforts are needed to validate the ability of this instrument to uniformly implant bulk-scale samples.

This work provides insight into fundamental nuclear materials science challenges of He degradation and sample size effects. For the future validation of nuclear structural materials, additional in-service conditions such as temperature, corrosion, time, and mechanical stresses, as well as accurate radiation dose and dose rates, should be implemented into ion implantation campaigns.

Chapter 6

Appendix A

In this appendix, the SOP for Tensile Testing of Radioactive Steels is presented. This SOP was developed and approved in order safely complete the high energy ion implantation and tensile testing work described in Chapter 4. The procedures were reviewed by members of the UC Berkeley EHS Staff as well as members of the Nuclear Materials Laboratory, and were approved on June 10, 2019.

Standard Operating Procedure

Read the EH&S Standard Operating Procedures Fact Sheet before filling out this form. Print out the completed form and keep a readily accessible hard copy in the lab (also keeping an electronic copy is highly recommended).

Date: **2019-06-10**

SOP Title: **Tensile Testing of Radioactive Steels [Activated Steel Isotopes]**

RUA Number: **6241**

Principal Investigator: **Peter Hosemann**

Room and Building: **Etcheverry Hall 1140**

Lab Phone Number: **510-642-1984**

Section 1 – Process

The machines and materials involved in this process are as follows:

- Tensile-compression module
- Sample grippers
- Designated sample spacers
- Designated sample screws and plate
- Sample catch plate

This SOP covers how to safely perform tensile testing on radioactive steel samples. An ion chamber should be present when first handling samples to have an idea of the dose rate associated with each. The beta window can be opened, but care should be taken to avoid contaminating the ion chamber. Whenever a source has exposure rates above 5 mR/hr, a “Caution: Radiation Area” sign must be posted. The Nuclear Engineering Safety Coordination can assist with locating a calibrated ion chamber and Caution Sign.

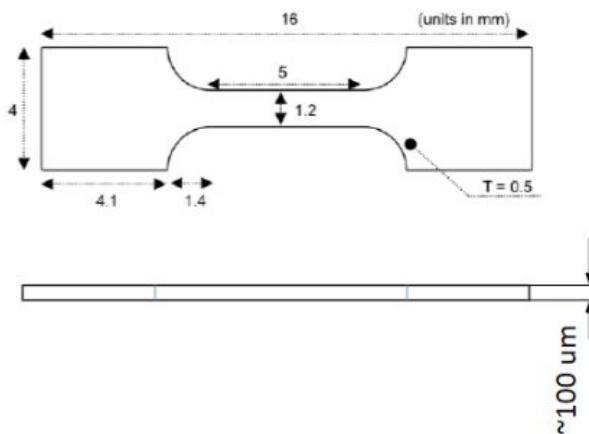

Procedure for thickness measurement

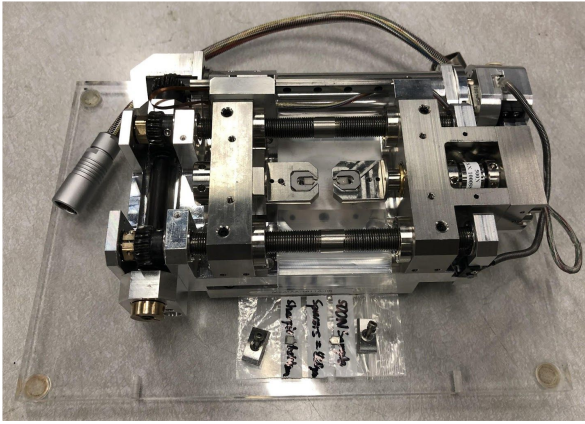
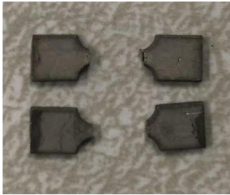

1. Transfer samples in their leaded holders from lead cave, safe, or leaded source drawers to area near the thickness gauge. They shall be placed in such a lead shielded location, and such that they are not near any other workspaces or immediately adjacent to the workspace for this process.
2. Remove one stainless steel sample from its leaded holder. Only one sample should be removed at any given time.

3. Using tweezers, place sample in the thickness gauge. Measure the thickness of three different regions of the sample.
4. Return the sample to its leaded holder, and then to the lead shielded location.
5. Perform a self-survey and then meter survey the materials involved in the thickness measurement process.

Procedure for tensile testing

1. Change the load cell if needed. Change the tensile module grippers to the designated grippers for tensile testing of radioactive steels. Ensure the load cell and grippers are rigid and aligned. For samples less than 300 μm thick, place bottom spacers in grippers. Place the sample catch plate under the tensile test area.
2. Open experimental software and enter desired parameters. Position camera over test area.
3. Transfer samples in their leaded holders from lead cave, safe, or leaded source drawers to area near the tensile test module. They shall be placed in such a lead shielded location, and such that they are not near any other workspaces or immediately adjacent to the workspace for this process.
4. Remove one stainless steel sample from its leaded holder. Only one sample should be removed at any given time.
5. Using tweezers, place sample in the tensile test grippers. For samples less than 300 μm thick, top with additional spacers. Tighten sample in place with the designated sample screws and plate.
6. Perform tensile test. If the sample fractures, stop the test and follow the protocol outlined in Section 3 - Potential Hazards. If the sample does not fracture, move the grippers back to their original position.
7. Remove sample screw plate and spacer. Remove sample from the grippers and return to storage.
8. Clean up work station and fume hood following proper radioactive work protocols.
9. Perform a self-survey and then meter survey the machines and materials involved in the tensile test process.

<p>Images of equipment used can be found below.</p>	
<p>Sample drawing with dimensions</p>	
<p>Thickness gauge</p>	

<p>Tensile-compression module</p>	
<p>Sample spacers</p>	
<p>Sample screws and set plates</p>	

Section 2 – Hazardous Chemicals

No hazardous chemicals are expected as part of this procedure.

Section 3 – Potential Hazards

Sample fracture

If the sample fractures, there is potential for high localized dose from these fragments if they were to be embedded in the skin. For this reason it is important to ensure that surveys are performed.

A cover will be placed over the system during the test, to prevent any fractured pieces from leaving the work area. A catch plate will be placed under the system, to collect any possible sample pieces.

After a sample fractures, the catch plate and local area will be surveyed. Any pieces that are large enough to be collected will be removed. A thorough survey of the test area will determine if any smaller pieces are still present. These small pieces will be removed with a paper towel dampened with deionized water.

Radiation exposure

Primary hazards associated with samples will be radiation dose. This work involves handling small irradiated samples. Most often these are steel alloys that will have a mixed isotopic makeup of beta and gamma emitting nuclides. Half-lives associated with these isotopes are generally medium to long lived (order of days to a few years) with the total activity of all the samples being approximately on the order of 30 mCi. The exposure rate of all the samples together taken as a point source theoretically could be as high as 200+ rem/hr on contact.

Handling only one sample at a time, using tweezers to place the sample, and avoiding direct contact with the sample will greatly reduce the exposure rate. Additionally, users shall be well-trained on the procedure using non-radioactive samples, so that the time spent around the samples is minimized, which will also greatly reduce the overall dose.

Using a high exposure rate scenario – 15 mCi of ^{56}Co – the approximate dose rates (beta and gamma) associated with this work would be:

- 15 mCi at 1 cm = 250 rem/hr*
- 15 mCi at 6 cm (tweezers) = 7.5 rem/hr*
- 5 minutes handling 15 mCi at 6 cm \approx 625 mrem*

The samples handled under this SOP will have a lower overall activity than the high exposure rate scenario above, because the scenario accounts for the activity of more than 2 samples combined, and in reality each sample will be handled individually. ^{56}Co is a positron emitter and therefore has a significant dose rate from annihilation gamma rays with energies of 511 keV.

If new materials are used in future work, it is important to look at each sample on a case-by-case basis to consider the isotopes involved. Each sample will be verified to have a lower dose rate than the above high exposure scenario using the Irradiated Sample Worksheet (#RD-58). If the sample has a higher dose rate, then this SOP must be modified to take further dose precautions.

*Based on RD-58 calculator using combined gamma dose and beta skin dose

Section 4 – Approvals Required

All Users must go through radiation safety training, be listed on the lab RUA, and be issued dosimetry. The first time **any** researcher performs this procedure, Radiation Safety must be present to help ensure doses are kept As Low As Reasonably Achievable (ALARA).

New users will be trained in this procedure by experienced personnel. Given the potentially significant doses associated with this procedure, Radiation Safety personnel must be present when any new user performs this procedure for the first time.

Section 5 – Designated Area

The samples will be removed from either the source drawers to the left of the fume hood or lead-shielded containers in the fume hood in the northwest corner off 1140 Etcheverry Hall. This fume hood has been previously designated for radioactive-work.

Section 6 – Special Handling Procedures and Storage Requirements

While being used, samples will be handled with tweezers and other tools to avoid directly grabbing them.

While not being used, the samples will be stored in the source drawers or leaded containers. The leaded containers will then be stored either a lockable lead cave along the north wall of 1140 or in a lockable, leaded safe in the northeast corner of 1140.

Dosimetry – TLD finger ring for both hands and whole body badge – is required for all work under this SOP

Section 7 – Personal Protective Equipment

- A clean, full-length, long sleeved lab coat
- Safety glasses
- Disposable gloves
- Clothing that fully covers the legs
- Close-toed shoes
- Dosimetry – all dosimetry should be stored away from sources of radiation

Section 8 – Engineering/Ventilation Controls

Lead shielding will be placed around the work area to limit radiation exposure to users.

An ion chamber will be available to determine ambient exposure levels while sources are present.

Section 9 – Spill and Accident Procedures

Radiation Safety will be present and provide instruction in the following situations:

- A radioactive material spill
- Skin contamination
- Ingestion of radioactive material
- Unexpected personnel exposure
- Airborne radioactivity
- Loss or theft of radioactive materials

In the event of contamination after a tensile test:

- Stop work and avoid spreading contamination.
- Contact EH&S Radiation Safety on how to proceed.

In the event of skin contamination:

- Remove contaminated clothing and wash the contaminated skin area gently with mild soap and lukewarm water (never hot water!) Do not abrade the skin with rough scrubbing or excessive washing, and do not use solvents. Follow all instructions from Radiation Safety.

If the spill is significant, the RSO will help plan/coordinate the cleanup.

Section 10 – Waste Disposal

Dry Waste: Collect the dry waste in double clear plastic bags. Be sure to use strong plastic bags that won't rip. Label the waste container with a caution radioactive materials label and indicate the radionuclide. Due to the potential high activity in the waste, a shielded waste container should be utilized to minimize radiation levels in the area. If the waste is reading more than 2 mR/hr on contact. Once your waste bag is full, log onto RSIS to initiate its disposal and to print out the waste label and affix it to your waste container. You should request an "EH&S pick-up" from RSIS for the disposal of your waste. Leave the waste inside of the shielded container/in shielded location until it gets picked up by EH&S.

This work will not generate any mixed waste nor liquid waste.

Samples that are not useful will be transferred to Radiation Safety for removal from campus.

Section 11 - Decontamination

Clearly label contaminated equipment until it has been decontaminated.

Surface of contamination can be cleaned with paper towels and a decontamination solution. Start by wetting a paper towel with your decontamination solution and, working from the outer edge of the contaminated area, wipe the surface inward toward the center of the contaminated area. Discard the towels into a radioactive waste container after each pass. Do not re-use the paper towels or wipe the contaminated area in a circular fashion. Repeat this until the paper towels are no longer picking up removable contamination. This process should pick up small solid metal pieces that are unable to be removed by tweezers, but care must be taken to ensure these micro-shards are deposited in the waste. Frequent surveys after experimental work until the equipment is found to be at background levels will ensure that no radioactive material is unaccounted for.

Chapter 7

Appendix B

The ion beam degrader wedge position table is given in this appendix. There are four wedges. Each wedge has four different filter thicknesses, and thus four different possible positions. In the table, the positions are numbered 0, 1, 2, and 3. The table (without headings) is uploaded as a .csv file in the degrader controls software, which reads each line and moves the wedges to the calibrated position accordingly. After the specified dwell time on each position, the software automatically reads the next line. Once it reaches the end of the table, it begins reading from the beginning without delay. The table is optimized such that no position occurs twice in a row, therefore providing maximum cooling between positions.

Table 7.1: Ion beam degrader wedge position table. There are 165 combinations presented, which allow for 165 levels of degradation.

Wedge 1	Wedge 2	Wedge 3	Wedge 4
0	0	2	3
1	1	3	2
0	2	1	3
3	0	0	2
2	3	3	0
3	1	0	1
1	2	2	2
0	3	3	0
2	2	1	3
0	3	2	1
2	1	3	2
3	2	0	3
2	1	2	2
1	3	3	0
2	0	1	2
0	2	2	3
1	1	1	2
2	3	3	1
1	1	0	3
0	3	1	2
3	1	3	1
1	3	0	3
3	1	2	1
0	3	0	2
1	0	1	3
0	2	3	1
2	1	1	3
0	3	2	0
3	0	0	3
1	2	2	1
2	1	0	2
3	0	1	1
1	3	2	2
3	0	1	3
1	1	3	1
3	0	2	0

1	3	1	2
2	1	0	3
3	3	1	1
0	2	3	2
2	1	2	1
1	2	3	2
3	3	2	1
0	1	1	3
2	3	2	1
3	0	3	0
1	3	1	3
3	1	3	2
2	2	2	1
0	1	3	3
2	3	1	0
0	2	0	3
3	0	1	2
2	3	0	3
3	1	1	2
1	2	3	0
0	3	0	3
3	2	1	2
1	0	2	3
2	2	1	0
0	3	3	1
3	2	2	0
1	3	3	1
2	0	0	3
3	3	1	2
2	0	3	1
0	1	2	3
2	2	1	1
1	1	2	2
0	0	3	3
2	3	1	1
0	1	2	2
2	2	3	0
3	3	0	3
2	1	2	0

1	0	3	3
3	3	0	0
2	0	1	3
3	2	0	1
0	0	3	2
1	2	0	3
0	3	3	2
1	1	2	3
3	2	3	1
1	3	1	0
3	0	2	3
0	2	1	2
1	1	2	1
3	2	3	0
1	3	0	1
0	2	3	3
2	3	0	2
3	2	1	3
1	3	0	2
2	1	1	1
1	0	3	2
2	1	2	3
3	3	1	0
2	0	2	1
1	1	3	0
3	2	2	1
2	1	3	0
3	3	0	1
2	0	2	2
1	1	1	3
2	2	0	1
0	0	1	3
1	2	3	1
3	0	2	2
0	3	1	1
3	1	3	0
0	2	2	1
3	3	3	0
1	2	1	3

2	3	2	2
3	1	1	3
2	2	2	0
0	1	3	1
2	3	2	0
1	2	0	2
3	1	2	0
1	2	1	2
2	1	3	1
1	3	2	0
2	0	3	3
3	2	0	2
1	0	3	1
3	1	2	2
0	2	3	0
3	1	0	3
2	2	1	2
0	3	2	3
2	2	3	2
3	1	1	1
1	2	2	3
2	0	3	0
1	3	2	1
0	1	3	2
2	0	2	3
3	1	0	2
1	2	2	0
2	1	1	2
3	3	2	0
2	2	0	3
3	0	2	1
2	3	1	2
1	1	3	3
0	2	2	2
3	1	1	0
2	2	2	2
0	3	1	3
3	2	2	2
2	3	0	1

3	0	3	2
1	2	1	1
3	3	0	2
2	2	3	1
1	0	2	2
3	2	1	0
2	0	3	2
3	2	1	1
0	3	2	2
3	0	3	1
2	2	0	2
1	3	1	1

Bibliography

- [1] Sally Benson. *Launching A Transformative Decade of Climate Action*. 2022. URL: <https://www.whitehouse.gov/ostp/news-updates/2022/09/20/launching-a-transformative-decade-of-climate-action/>.
- [2] Eric Larson et al. “Net-Zero America: Potential Pathways, Infrastructure, and Impacts Report”. In: *Princeton University* (2020), pp. 1–345.
- [3] *We Need A Mix*. Tech. rep. Third Way, 2016. URL: <https://www.thirdway.org/e-binder/we-need-a-mix>.
- [4] *The Ultimate Fast Facts Guide To Nuclear Energy*. Tech. rep. U.S. Department of Energy, Office of Nuclear Energy, 2019, p. 9. DOI: DOE/NE-0150. URL: <https://www.energy.gov/sites/prod/files/2019/01/f58/Ulimate%20Fast%20Facts%20Guide-PRINT.pdf>.
- [5] *U.S. nuclear capacity and generation expected to decline as existing generators retire*. Tech. rep. U.S. Energy Information Institution, 2017. URL: <https://www.eia.gov/todayinenergy/detail.php?id=31192>.
- [6] *Annual Energy Outlook 2022*. Tech. rep. U.S. Energy Information Administration, 2022. URL: https://www.eia.gov/outlooks/aeo/pdf/AEO2022_Narrative.pdf.
- [7] *Civil Nuclear Credit Program*. Tech. rep. U.S. Department of Energy, Grid Deployment Office, 2022. URL: <https://www.energy.gov/gdo/civil-nuclear-credit-program>.
- [8] *What’s the Lifespan for a Nuclear Reactor? Much Longer Than You Might Think*. Tech. rep. U.S. Department of Energy, Office of Nuclear Energy, 2020. URL: <https://www.energy.gov/ne/articles/whats-lifespan-nuclear-reactor-much-longer-you-might-think>.
- [9] *Advanced Reactor Demonstration Projects*. Tech. rep. U.S. Department of Energy, Office of Clean Energy Demonstrations. URL: <https://www.energy.gov/oced/advanced-reactor-demonstration-projects>.
- [10] Alan Ahn and Todd Allen. *2022 Advanced Nuclear Map: Charting a Breakout Year*. Tech. rep. Third Way, 2022. URL: <https://www.thirdway.org/graphic/2022-advanced-nuclear-map-charting-a-breakout-year>.

- [11] J D Lawson. “Some Criteria for a Power Producing Thermonuclear Reactor”. In: *Proceedings of the Physical Society. Section B* 70.1 (Jan. 1957), pp. 6–10. ISSN: 0370-1301. DOI: 10.1088/0370-1301/70/1/303. URL: <https://iopscience.iop.org/article/10.1088/0370-1301/70/1/303>.
- [12] H. Abu-Shawareb et al. “Lawson Criterion for Ignition Exceeded in an Inertial Fusion Experiment”. In: *Physical Review Letters* 129.7 (Aug. 2022), p. 075001. ISSN: 0031-9007. DOI: 10.1103/PhysRevLett.129.075001. URL: <https://link.aps.org/doi/10.1103/PhysRevLett.129.075001>.
- [13] *DOE Announces Cost-Shared Award for First-Ever Domestic Production of HALEU for Advanced Nuclear Reactors*. Tech. rep. U.S. Department of Energy, 2022. URL: <https://www.energy.gov/articles/doe-announces-cost-shared-award-first-ever-domestic-production-haleu-advanced-nuclear>.
- [14] Todd Allen et al. “Materials challenges for nuclear systems”. In: *Materials Today* 13.12 (Dec. 2010), pp. 14–23. ISSN: 13697021. DOI: 10.1016/S1369-7021(10)70220-0. URL: <https://linkinghub.elsevier.com/retrieve/pii/S1369702110702200>.
- [15] G.S. Was et al. “Materials for future nuclear energy systems”. In: *Journal of Nuclear Materials* 527 (Dec. 2019), p. 151837. ISSN: 00223115. DOI: 10.1016/j.jnucmat.2019.151837. URL: <https://linkinghub.elsevier.com/retrieve/pii/S0022311519312334>.
- [16] Declan Butler. “Nuclear power’s new dawn”. In: *Nature* 429.6989 (May 2004), pp. 238–240. ISSN: 0028-0836. DOI: 10.1038/429238a. URL: <http://www.nature.com/articles/429238a>.
- [17] Gary Was. *Fundamentals of Radiation Materials Science*. New York: Springer-Verlag Berlin Heidelberg, 2007. ISBN: 978-3-540-49471-3.
- [18] S. J. Zinkle and G. S. Was. “Materials challenges in nuclear energy”. In: *Acta Materialia* 61.3 (2013), pp. 735–758. ISSN: 13596454. DOI: 10.1016/j.actamat.2012.11.004. URL: <http://dx.doi.org/10.1016/j.actamat.2012.11.004>.
- [19] International Atomic Energy Agency. “Structural Materials for Liquid Metal Cooled Fast Reactor Fuel Assemblies — Operational Behaviour STI/PUB/1548”. In: *IAEA Nuclear Energy Series* (2012), p. 103.
- [20] G H Kinchin and R S Pease. “The Displacement of Atoms in Solids by Radiation”. In: *Reports on Progress in Physics* 18.1 (Jan. 1955), p. 301. ISSN: 00344885. DOI: 10.1088/0034-4885/18/1/301. URL: <https://iopscience.iop.org/article/10.1088/0034-4885/18/1/301>.
- [21] H. Ullmaier and H. Trinkaus. “Helium in Metals: Effect on Mechanical Properties”. In: *Materials Science Forum* 97-99 (1992), pp. 451–472. DOI: 10.4028/www.scientific.net/msf.97-99.451.
- [22] H. Bolt et al. “Plasma facing and high heat flux materials - Needs for ITER and beyond”. In: *Journal of Nuclear Materials* 307-311.1 SUPPL. (2002), pp. 43–52. ISSN: 00223115. DOI: 10.1016/S0022-3115(02)01175-3.

- [23] World Nuclear Association. *Fast Neutron Reactors*. 2021. URL: <https://world-nuclear.org/information-library/current-and-future-generation/fast-neutron-reactors.aspx>.
- [24] Saeed A Alameri and Ahmed K Alkaabi. “1 - Fundamentals of nuclear reactors”. In: *Nuclear Reactor Technology Development and Utilization*. Ed. by Salah Ud-Din Khan and Alexander Nakhabov. Woodhead Publishing Series in Energy. Woodhead Publishing, 2020, pp. 27–60. ISBN: 978-0-12-818483-7. DOI: <https://doi.org/10.1016/B978-0-12-818483-7.00001-9>. URL: <https://www.sciencedirect.com/science/article/pii/B9780128184837000019>.
- [25] Lawrence Livermore National Laboratory. *Plutonium Aging*. Tech. rep. May. 2007, pp. 12–20.
- [26] J. S. Fraser and G. A. Bartholomew. “Spallation Neutron Sources.” In: *Neutron Sources for Basic Phys and Appl* (1983), pp. 217–235. DOI: 10.1142/9789814417204{_}0012.
- [27] Syed Naeem Ahmed. “1 - Properties and sources of radiation”. In: *Physics and Engineering of Radiation Detection (Second Edition)*. Ed. by Syed Naeem Ahmed. Second Edi. Elsevier, 2015, pp. 1–64. ISBN: 978-0-12-801363-2. DOI: <https://doi.org/10.1016/B978-0-12-801363-2.00001-2>. URL: <https://www.sciencedirect.com/science/article/pii/B9780128013632000012>.
- [28] B. M. Oliver et al. “Helium and hydrogen generation in pure metals irradiated with high-energy protons and spallation neutrons in LANSCE”. In: *Journal of Nuclear Materials* 307-311.2 SUPPL. (2002), pp. 1471–1477. ISSN: 00223115. DOI: 10.1016/S0022-3115(02)01295-3.
- [29] H. Ullmaier and F. Carsughi. “Radiation damage problems in high power spallation neutron sources”. In: *Nuclear Inst. and Methods in Physics Research, B* 101.4 (1995), pp. 406–421. ISSN: 0168583X. DOI: 10.1016/0168-583X(95)00590-0.
- [30] M. Grotenhuis, A.E. McArthy, and A.D. Rossin. *EXPERIMENTAL BREEDER REACTOR-II (EBR-II) SHIELD DESIGN*. Tech. rep. Argonne, IL (United States): Argonne National Laboratory (ANL), Sept. 1962. DOI: 10.2172/4781423. URL: <http://www.osti.gov/servlets/purl/4781423/>.
- [31] T.A. Gabriel, B.L. Bishop, and F.W. Wiffen. *Calculated irradiation response of materials using fission reactor (HFIR, ORR, and EBR-II) neutron spectra*. Tech. rep. Oak Ridge, TN (United States): Oak Ridge National Laboratory (ORNL), Aug. 1979. DOI: 10.2172/5968308. URL: <http://www.osti.gov/servlets/purl/5968308/>.
- [32] Peter Hosemann. “Studying radiation damage in structural materials by using ion accelerators”. In: *Reviews of Accelerator Science and Technology: Accelerator Applications in Industry and the Environment* 4 (2012), pp. 161–182. ISSN: 1793-6268. DOI: 10.1142/S1793626811000513.

- [33] Caitlin A. Taylor et al. “Using In Situ TEM Helium Implantation and Annealing to Study Cavity Nucleation and Growth”. In: *Jom* 72.5 (2020), pp. 2032–2041. ISSN: 15431851. DOI: 10.1007/s11837-020-04117-4. URL: <https://doi.org/10.1007/s11837-020-04117-4>.
- [34] H. Ullmaier. “Review Paper the Influence of Helium on the Bulk Properties of Fusion Reactor”. In: *Nuclear Fusion* 24 (1984), pp. 1039–83.
- [35] Shi Hao Li, Jing Ting Li, and Wei Zhong Han. “Radiation-induced helium bubbles in metals”. In: *Materials* 12.7 (2019). ISSN: 19961944. DOI: 10.3390/ma12071036.
- [36] Hongxian Xie et al. “A new loop-punching mechanism for helium bubble growth in tungsten”. In: *Acta Materialia* 141 (2017), pp. 10–17. ISSN: 13596454. DOI: 10.1016/j.actamat.2017.09.005.
- [37] H. Trinkaus. “Energetics and Formation Kinetics of Helium Bubbles in Metals.” In: *Radiation effects* 78.1-4 (1983), pp. 189–211. ISSN: 00337579. DOI: 10.1080/00337578308207371.
- [38] J. H. Evans. “An interbubble fracture mechanism of blister formation on helium-irradiated metals”. In: *Journal of Nuclear Materials* 68.2 (1977), pp. 129–140. ISSN: 00223115. DOI: 10.1016/0022-3115(77)90232-X.
- [39] H. Trinkaus and B. N. Singh. “Helium accumulation in metals during irradiation - Where do we stand?” In: *Journal of Nuclear Materials* 323.2-3 (2003), pp. 229–242. ISSN: 00223115. DOI: 10.1016/j.jnucmat.2003.09.001.
- [40] J. H. Evans. “A mechanism of surface blistering on metals irradiated with helium ions”. In: *Journal of Nuclear Materials* 61.1 (1976), pp. 1–7. ISSN: 00223115. DOI: 10.1016/0022-3115(76)90092-1.
- [41] E. P. EerNisse and S. T. Picraux. “Role of integrated lateral stress in surface deformation of He-implanted surfaces”. In: *Journal of Applied Physics* 48.1 (1977), pp. 9–17. ISSN: 00218979. DOI: 10.1063/1.323332.
- [42] P. B. Johnson, R. W. Thomson, and Karen Reader. “TEM and SEM studies of radiation blistering in helium-implanted copper”. In: *Journal of Nuclear Materials* 273.2 (1999), pp. 117–129. ISSN: 00223115. DOI: 10.1016/S0022-3115(99)00046-X.
- [43] Y. Yang et al. “Irradiation damage investigation of helium implanted polycrystalline copper”. In: *Journal of Nuclear Materials* 512 (2018), pp. 137–143. ISSN: 00223115. DOI: 10.1016/j.jnucmat.2018.09.022. URL: <https://doi.org/10.1016/j.jnucmat.2018.09.022>.
- [44] Frances I. Allen, Peter Hosemann, and Mehdi Balooch. “Key mechanistic features of swelling and blistering of helium-ion-irradiated tungsten”. In: *Scripta Materialia* 178.100 (2020), pp. 256–260. ISSN: 13596462. DOI: 10.1016/j.scriptamat.2019.11.039.

- [45] Frances I. Allen. “A review of defect engineering, ion implantation, and nanofabrication using the helium ion microscope”. In: *Beilstein Journal of Nanotechnology* 12 (2021), pp. 633–664. ISSN: 21904286. DOI: 10.3762/BJNANO.12.52.
- [46] P. Hosemann et al. “Quantifying residual stress in Helium implanted surfaces and its implication for blistering.” In: (2021).
- [47] Peter Hosemann. “Small-scale mechanical testing on nuclear materials: bridging the experimental length-scale gap”. In: *Scripta Materialia* 143 (2018), pp. 161–168. ISSN: 13596462. DOI: 10.1016/j.scriptamat.2017.04.026. URL: <https://doi.org/10.1016/j.scriptamat.2017.04.026>.
- [48] S.H. Goods. “The influence of tritium exposure and helium build-in on the properties of OFHC copper”. In: *Scripta Metallurgica* 20.4 (Apr. 1986), pp. 565–569. ISSN: 00369748. DOI: 10.1016/0036-9748(86)90255-3.
- [49] George R. Caskey, David E. Rawl, and David A. Mezzanotte. “Helium embrittlement of stainless steels at ambient temperature”. In: *Scripta Metallurgica* 16.8 (Aug. 1982), pp. 969–972. ISSN: 00369748. DOI: 10.1016/0036-9748(82)90135-1.
- [50] Benny Glam et al. “Dynamic fracture and spall in aluminum with helium bubbles”. In: *International Journal of Fracture* 163.1-2 (2010), pp. 217–224. ISSN: 03769429. DOI: 10.1007/s10704-009-9437-1.
- [51] Ting Ting Zhou et al. “Spall damage in single crystal Al with helium bubbles under decaying shock loading via molecular dynamics study”. In: *Computational Materials Science* 162. January (2019), pp. 255–267. ISSN: 09270256. DOI: 10.1016/j.commatsci.2019.02.019. URL: <https://doi.org/10.1016/j.commatsci.2019.02.019>.
- [52] Ming Shuai Ding et al. “Nanobubble fragmentation and bubble-free-channel shear localization in helium-irradiated submicron-sized copper”. In: *Physical Review Letters* 117.21 (2016), pp. 1–5. ISSN: 10797114. DOI: 10.1103/PhysRevLett.117.215501.
- [53] Si Mian Liu, Shi Hao Li, and Wei Zhong Han. “Revealing the Dynamics of Helium Bubbles Using In Situ Techniques”. In: *Jom* 72.6 (2020), pp. 2352–2362. ISSN: 15431851. DOI: 10.1007/s11837-020-04157-w. URL: <https://doi.org/10.1007/s11837-020-04157-w>.
- [54] Ming Shuai Ding et al. “Radiation-Induced Helium Nanobubbles Enhance Ductility in Submicron-Sized Single-Crystalline Copper”. In: *Nano Letters* 16.7 (2016), pp. 4118–4124. ISSN: 15306992. DOI: 10.1021/acs.nanolett.6b00864.
- [55] R. M. Flanagan et al. “Molecular dynamics simulations of ejecta formation in helium-implanted copper”. In: *Scripta Materialia* 178 (2020), pp. 114–118. ISSN: 13596462. DOI: 10.1016/j.scriptamat.2019.11.005.
- [56] Saryu Fensin et al. “The role of helium on ejecta production in copper”. In: *Materials* 13.6 (2020), pp. 1–11. ISSN: 19961944. DOI: 10.3390/ma13061270.

- [57] Peter Hosemann et al. “Helium Implantation Studies Utilizing the HIM. Turning a Bug into a Feature”. In: *Microscopy and Microanalysis* 26.Suppl 2 (2020), pp. 1–3. ISSN: 1431-9276. DOI: 10.1017/s1431927620015810.
- [58] Arey BW, Shutthanandan V., and Jiang W. “Helium Ion Microscopy versus Scanning Electron Microscopy”. In: *Microscopy and Microanalysis*, 2010.
- [59] Richard Livengood et al. “Subsurface damage from helium ions as a function of dose, beam energy, and dose rate”. In: *Journal of Vacuum Science & Technology B: Microelectronics and Nanometer Structures* 27.6 (2009), p. 3244. ISSN: 10711023. DOI: 10.1116/1.3237101.
- [60] M. V. Ambat et al. “Localized Helium Implantation in SiCf/SiCm Composites Comparing Fiber and Matrix Swelling”. In: *Jom* 72.1 (2020), pp. 170–175. ISSN: 15431851. DOI: 10.1007/s11837-019-03869-y.
- [61] Zhang Jie Wang et al. “Mechanical behavior of copper containing a gas-bubble superlattice”. In: *Acta Materialia* 121 (2016), pp. 78–84. ISSN: 13596454. DOI: 10.1016/j.actamat.2016.08.085. URL: <http://dx.doi.org/10.1016/j.actamat.2016.08.085>.
- [62] Mehdi Balooch et al. *Mechanical and Structural Transformation of Tungsten Implanted with He Ions*. Tech. rep.
- [63] Peter Hosemann et al. “Helium Implantation Studies Utilizing the HIM. Turning a Bug into a Feature”. In: *Microscopy and Microanalysis* 26.S2 (2020), pp. 782–783. ISSN: 1431-9276. DOI: 10.1017/s1431927620015810.
- [64] S. J. Fensin et al. “Effect of grain boundary structure on plastic deformation during shock compression using molecular dynamics”. In: *Modelling and Simulation in Materials Science and Engineering* 21.1 (2013). ISSN: 09650393. DOI: 10.1088/0965-0393/21/1/015011.
- [65] Maik Butterling. *Positron Annihilation Spectroscopy at the HZDR*. URL: <https://www.hzdr.de/db/Cms?pNid=no&pOid=38378>.
- [66] G. Amarendra et al. “Nucleation and growth of helium bubbles in nickel studied by positron-annihilation spectroscopy”. In: *Physical Review B* 45.18 (1992), pp. 10231–10241. ISSN: 01631829. DOI: 10.1103/PhysRevB.45.10231.
- [67] V. S. Subrahmanyam, P. M.G. Nambissan, and P. Sen. “Helium bubbles in tungsten studied by positron annihilation”. In: *Solid State Communications* 89.6 (1994), pp. 523–527. ISSN: 00381098. DOI: 10.1016/0038-1098(94)90749-8.
- [68] PerkinElmer Inc. “Dynamic Mechanical Analysis (DMA) - A Beginner’s Guide”. In: *Introduction to DMA* (2008), pp. 1–23. URL: https://www.perkinelmer.com/CMSResources/Images/44-74546GDE_IntroductionToDMA.pdf.
- [69] M Loretto. *Defect Analysis in Electron Microscopy*. Wiley, 1975. ISBN: 0412137607.

- [70] G. B. Viswanathan et al. “Direct observations and analyses of dislocation substructures in the α phase of an α/β Ti-alloy formed by nanoindentation”. In: *Acta Materialia* 53.19 (2005), pp. 5101–5115. ISSN: 13596454. DOI: 10.1016/j.actamat.2005.07.030.
- [71] Jordan S. Weaver and Surya R. Kalidindi. “Mechanical characterization of Ti-6Al-4V titanium alloy at multiple length scales using spherical indentation stress-strain measurements”. In: *Materials and Design* 111 (2016), pp. 463–472. ISSN: 18734197. DOI: 10.1016/j.matdes.2016.09.016. URL: <http://dx.doi.org/10.1016/j.matdes.2016.09.016>.
- [72] Fabian Pöhl. “Pop-in behavior and elastic-to-plastic transition of polycrystalline pure iron during sharp nanoindentation”. In: *Scientific Reports* 9.1 (2019), pp. 1–12. ISSN: 20452322. DOI: 10.1038/s41598-019-51644-5.
- [73] Claudio Zambaldi et al. “Orientation informed nanoindentation of α -titanium: Indentation pileup in hexagonal metals deforming by prismatic slip”. In: *Journal of Materials Research* 27.1 (2012), pp. 356–367. ISSN: 08842914. DOI: 10.1557/jmr.2011.334.
- [74] Wei Li, Kevin G. Field, and Dane Morgan. “Automated defect analysis in electron microscopic images”. In: *npj Computational Materials* 4.1 (Dec. 2018). ISSN: 20573960. DOI: 10.1038/s41524-018-0093-8.
- [75] J. H. Evans. “THE ROLE OF IMPLANTED GAS AND LATERAL STRESS IN BLISTER FORMATION MECHANISMS”. In: *Journal of Nuclear Materials* 76 & 77 (1978), pp. 228–234.
- [76] G. T. Gray. “Influence of Shock-Wave Deformation on the Structure/Property Behavior of Materials”. In: *High-Pressure Shock Compression of Solids* (1993), pp. 187–215. DOI: 10.1007/978-1-4612-0911-9{_}6.
- [77] M. O. Liedke et al. “Open volume defects and magnetic phase transition in Fe₆₀Al₄₀ transition metal aluminide”. In: *Journal of Applied Physics* 117.16 (Apr. 2015), p. 163908. ISSN: 0021-8979. DOI: 10.1063/1.4919014.
- [78] Wolfgang Anwand et al. “Design and Construction of a Slow Positron Beam for Solid and Surface Investigations”. In: *Defect and Diffusion Forum* 331 (Sept. 2012), pp. 25–40. ISSN: 1662-9507. DOI: 10.4028/www.scientific.net/DDF.331.25.
- [79] M. Clement et al. “Analysis of positron beam data by the combined use of the shape and wing-parameters”. In: *Journal of Applied Physics* 79.12 (June 1996), pp. 9029–9036. ISSN: 0021-8979. DOI: 10.1063/1.362635.
- [80] Andreas Wagner et al. “Positron annihilation lifetime and Doppler broadening spectroscopy at the ELBE facility”. In: 2018, p. 040003. DOI: 10.1063/1.5040215. URL: <http://aip.scitation.org/doi/abs/10.1063/1.5040215>.

- [81] E. Hirschmann et al. “A new system for real-time data acquisition and pulse parameterization for digital positron annihilation lifetime spectrometers with high repetition rates”. In: *Journal of Instrumentation* 16.08 (Aug. 2021), P08001. ISSN: 1748-0221. DOI: 10.1088/1748-0221/16/08/P08001. URL: <https://iopscience.iop.org/article/10.1088/1748-0221/16/08/P08001>.
- [82] J. V. Olsen et al. “PALSfit: A new program for the evaluation of positron lifetime spectra”. In: *physica status solidi c* 4.10 (Sept. 2007), pp. 4004–4006. ISSN: 1862-6351. DOI: 10.1002/pssc.200675868. URL: <https://onlinelibrary.wiley.com/doi/10.1002/pssc.200675868>.
- [83] F.A. Selim. “Positron annihilation spectroscopy of defects in nuclear and irradiated materials- a review”. In: *Materials Characterization* 174 (Apr. 2021), p. 110952. ISSN: 10445803. DOI: 10.1016/j.matchar.2021.110952. URL: <https://linkinghub.elsevier.com/retrieve/pii/S1044580321000826>.
- [84] J. Čížek et al. “Vacancy clusters in ultra fine grained metals prepared by severe plastic deformation”. In: *Journal of Physics: Conference Series* 443.1 (2013). ISSN: 17426596. DOI: 10.1088/1742-6596/443/1/012008.
- [85] Ken Wada and Toshio Hyodo. “A simple shape-free model for pore-size estimation with positron annihilation lifetime spectroscopy”. In: *Journal of Physics: Conference Series* 443.1 (2013). ISSN: 17426596. DOI: 10.1088/1742-6596/443/1/012003.
- [86] Tanvi Ajantiwalay et al. “Investigation of hardening mechanisms and size effects in proton-irradiated HT-9 steels”. In: *Journal of Nuclear Materials* 548 (2021), p. 152866. ISSN: 00223115. DOI: 10.1016/j.jnucmat.2021.152866. URL: <https://doi.org/10.1016/j.jnucmat.2021.152866>.
- [87] Stuart A. Maloy et al. “The effects of fast reactor irradiation conditions on the tensile properties of two ferritic/martensitic steels”. In: *Journal of Nuclear Materials* 356.1-3 (2006), pp. 62–69. ISSN: 00223115. DOI: 10.1016/j.jnucmat.2006.05.024.
- [88] Yiren Chen. “Irradiation effects of HT-9 martensitic steel”. In: *Nuclear Engineering and Technology* 45.3 (2013), pp. 311–322. ISSN: 2234358X. DOI: 10.5516/NET.07.2013.706. URL: <http://dx.doi.org/10.5516/NET.07.2013.706>.
- [89] A. F. Rowcliffe et al. “Fracture toughness and tensile behavior of ferritic-martensitic steels irradiated at low temperatures”. In: *Journal of Nuclear Materials* 258-263.PART 2 B (1998), pp. 1275–1279. ISSN: 00223115. DOI: 10.1016/S0022-3115(98)00163-9.
- [90] K. Farrell and T. S. Byun. “Tensile properties of ferritic/martensitic steels irradiated in HFIR, and comparison with spallation irradiation data”. In: *Journal of Nuclear Materials* 318.SUPPL (2003), pp. 274–282. ISSN: 00223115. DOI: 10.1016/S0022-3115(03)00102-8.

- [91] N. Baluc et al. “Mechanical properties and microstructure of the OPTIMAX series of low activation ferritic-martensitic steels”. In: *Journal of Nuclear Materials* 283-287.PART I (2000), pp. 731–735. ISSN: 00223115. DOI: 10.1016/S0022-3115(00)00282-8.
- [92] Y. Dai et al. “Mechanical properties and microstructure in low-activation martensitic steels F82H and Optimax after 800-MeV proton irradiation”. In: *Journal of Nuclear Materials* 283.287 (2000), pp. 513–517. ISSN: 00223115. DOI: 10.1016/S0022-3115(00)00267-1.
- [93] R L Klueh and J M Vitek. “Postirradiation tensile behavior of Nickel-dopes ferritic Steels”. In: *Journal of Nuclear Materials* 150 (1987), pp. 272–280. DOI: [https://doi.org/10.1016/0022-3115\(87\)90004-3](https://doi.org/10.1016/0022-3115(87)90004-3).
- [94] P. Hosemann et al. “Large and Small Scale Materials Testing of HT-9 Irradiated in the STIP Irradiation Program”. In: *Experimental Mechanics* 51.7 (2011), pp. 1095–1102. ISSN: 00144851. DOI: 10.1007/s11340-010-9419-2.
- [95] J. F. Ziegler, J. P. Biersack, and M.D. Ziegler. *The Stopping and Range of Ions in Matter*. 7th ed. Chester, MD: SRIM Co., 2008. ISBN: 0-9654207-1-X.
- [96] Julia R. Greer and Jeff Th M. De Hosson. “Plasticity in small-sized metallic systems: Intrinsic versus extrinsic size effect”. In: *Progress in Materials Science* 56.6 (2011), pp. 654–724. ISSN: 00796425. DOI: 10.1016/j.pmatsci.2011.01.005. URL: <http://dx.doi.org/10.1016/j.pmatsci.2011.01.005>.
- [97] X. X. Chen and A. H.W. Ngan. “Specimen size and grain size effects on tensile strength of Ag microwires”. In: *Scripta Materialia* 64.8 (2011), pp. 717–720. ISSN: 13596462. DOI: 10.1016/j.scriptamat.2010.12.031. URL: <http://dx.doi.org/10.1016/j.scriptamat.2010.12.031>.
- [98] B. Yang et al. “Yield stress influenced by the ratio of wire diameter to grain size - A competition between the effects of specimen microstructure and dimension in micro-sized polycrystalline copper wires”. In: *Philosophical Magazine* 92.25-27 (2012), pp. 3243–3256. ISSN: 14786435. DOI: 10.1080/14786435.2012.693215.
- [99] Yutaka Kohno et al. “Specimen size effects on the tensile properties of JPCA and JFMS”. In: *Journal of Nuclear Materials* 283-287.PART II (2000), pp. 1014–1017. ISSN: 00223115. DOI: 10.1016/S0022-3115(00)00245-2.
- [100] A. Kohyama, K. Hamada, and H. Matsui. “Specimen size effects on tensile properties of neutron-irradiated steels”. In: *Journal of Nuclear Materials* 179-181.PART 1 (1991), pp. 417–420. ISSN: 00223115. DOI: 10.1016/0022-3115(91)90113-L.
- [101] P. Hosemann, C. Shin, and D. Kiener. “Small scale mechanical testing of irradiated materials”. In: *Journal of Materials Research* 30.9 (2015), pp. 1231–1245. ISSN: 20445326. DOI: 10.1557/jmr.2015.26.

- [102] C. Y. Dai et al. “Understanding scale-dependent yield stress of metals at micrometre scales”. In: *Philosophical Magazine Letters* 93.9 (2013), pp. 531–540. ISSN: 09500839. DOI: 10.1080/09500839.2013.816447.
- [103] P. Hosemann, C. Shin, and D. Kiener. “Small scale mechanical testing of irradiated materials”. In: *Journal of Materials Research* 30.9 (2015), pp. 1231–1245. ISSN: 20445326. DOI: 10.1557/jmr.2015.26.
- [104] D Kiener et al. “Europe PMC Funders Group In situ nano-compression testing of irradiated copper”. In: 10.8 (2012), pp. 608–613. DOI: 10.1038/nmat3055. In.
- [105] D.S. Gianola and C. Eberl. “Micro- and Nanoscale Tensile testing of Materials”. In: *JOM* 61.3 (2009), pp. 24–35. URL: www.tms.org/jom.html.
- [106] H. Tang, K.W. Schwarz, and H.D. Espinosa. “Dislocation escape-related size effects in single-crystal micropillars under uniaxial compression”. In: *Acta Materialia* 55.5 (Mar. 2007), pp. 1607–1616. ISSN: 13596454. DOI: 10.1016/j.actamat.2006.10.021.
- [107] Gerhard Dehm. “Miniaturized single-crystalline fcc metals deformed in tension: New insights in size-dependent plasticity”. In: *Progress in Materials Science* 54.6 (Aug. 2009), pp. 664–688. ISSN: 00796425. DOI: 10.1016/j.pmatsci.2009.03.005.
- [108] R. Dou and B. Derby. “A universal scaling law for the strength of metal micropillars and nanowires”. In: *Scripta Materialia* 61.5 (Sept. 2009), pp. 524–527. ISSN: 13596462. DOI: 10.1016/j.scriptamat.2009.05.012.
- [109] Daniel Kiener et al. “Prospects of Using Small Scale Testing to Examine Different Deformation Mechanisms in Nanoscale Single Crystals—A Case Study in Mg”. In: *Crystals* 11.1 (Jan. 2021), p. 61. ISSN: 2073-4352. DOI: 10.3390/cryst11010061.
- [110] Kundan Kumar et al. “Use of Miniature Tensile Specimen for Measurement of Mechanical Properties”. In: *Procedia Engineering* 86 (2014), pp. 899–909. ISSN: 18777058. DOI: 10.1016/j.proeng.2014.11.112.
- [111] A Dong et al. “Micro-Mesoscale Mechanical Testing of 304SS, HT-9, and CuCrZr, Unpublished Manuscript”. In: (2022).
- [112] Peter Hosemann. “Studying Radiation Damage in Structural Materials by Using Ion Accelerators”. In: *Reviews of Accelerator Science and Technology* 04.01 (Jan. 2011), pp. 161–182. ISSN: 1793-6268. DOI: 10.1142/S1793626811000513.
- [113] Sarah Stevenson et al. “The effects of high energy deuteron ion beam irradiation on the tensile behavior of HT-9”. In: *Nuclear Instruments and Methods in Physics Research Section B: Beam Interactions with Materials and Atoms* 531 (Nov. 2022), pp. 65–73. ISSN: 0168583X. DOI: 10.1016/j.nimb.2022.09.001.
- [114] Sarah Stevenson et al. “Properties of a helium ion beam degrader for implanting SSJ2 tensile specimens at the LBL 88-inch cyclotron”. In: *Transactions of the American Nuclear Society*. Vol. 123. 1. American Nuclear Society, 2020, pp. 173–175. DOI: 10.13182/T123-33452.

- [115] Jonathan T. Morrell et al. “Measurement of $^{139}\text{La}(p,x)$ cross sections from 35–60 MeV by stacked-target activation”. In: *European Physical Journal A* 56.1 (2020). ISSN: 1434601X. DOI: 10.1140/epja/s10050-019-00010-0. URL: <https://doi.org/10.1140/epja/s10050-019-00010-0>.
- [116] J. R. Cooper et al. “Production of a ^{76}Kr radioactive ion beam using a batch mode method”. In: *Nuclear Instruments and Methods in Physics Research, Section A: Accelerators, Spectrometers, Detectors and Associated Equipment* 533.3 (2004), pp. 287–294. ISSN: 01689002. DOI: 10.1016/j.nima.2004.06.151.
- [117] A. Trkov et al. “IRDFF-II: A New Neutron Metrology Library”. In: *Nuclear Data Sheets* 163 (2020), pp. 1–108. ISSN: 00903752. DOI: 10.1016/j.nds.2019.12.001.
- [118] Huo Junde, Huo Su, and Yang Dong. “Nuclear Data Sheets for $A = 56$ ”. In: *Nuclear Data Sheets* 112.6 (2011), pp. 1513–1645. ISSN: 00903752. DOI: 10.1016/j.nds.2011.04.004. URL: <http://dx.doi.org/10.1016/j.nds.2011.04.004>.
- [119] Brookhaven National Laboratory, B Pritychenko, and A Sonzogni. *NNDC Q-value Calculator (Q-Calc)*. URL: <https://www.nndc.bnl.gov/qcalc>.
- [120] R. L. Klueh. “Elevated temperature ferritic and martensitic steels and their application to future nuclear reactors”. In: *International Materials Reviews* 50.5 (2005), pp. 287–310. ISSN: 09506608. DOI: 10.1179/174328005X41140.
- [121] Ce Zheng, Stuart Maloy, and Djamel Kaoumi. “Effect of dose on irradiation-induced loop density and Burgers vector in ion-irradiated ferritic/martensitic steel HT9”. In: *Philosophical Magazine* 98.26 (2018), pp. 2440–2456. ISSN: 14786443. DOI: 10.1080/14786435.2018.1490825. URL: <https://doi.org/10.1080/14786435.2018.1490825>.
- [122] Huan Yan et al. “Phase stability and microstructural evolution in neutron-irradiated ferritic-martensitic steel HT9”. In: *Journal of Nuclear Materials* 557 (2021), p. 153252. ISSN: 00223115. DOI: 10.1016/j.jnucmat.2021.153252. URL: <https://doi.org/10.1016/j.jnucmat.2021.153252>.
- [123] E. Azrt. “Size effects in materials due to microstructural and dimensional constraints: A comparative review”. In: *Acta Materialia* 46.16 (1998), pp. 5611–5626. ISSN: 09575820. DOI: [https://doi.org/10.1016/S1359-6454\(98\)00231-6](https://doi.org/10.1016/S1359-6454(98)00231-6).
- [124] Maximilien E. Launey and Robert O. Ritchie. “On the fracture toughness of advanced materials”. In: *Advanced Materials* 21.20 (2009), pp. 2103–2110. ISSN: 09359648. DOI: 10.1002/adma.200803322.
- [125] R. L. Klueh and J. M. Vitek. “Fluence and helium effects on the tensile properties of ferritic steels at low temperatures”. In: *Journal of Nuclear Materials* 161.1 (1989), pp. 13–23. ISSN: 00223115. DOI: 10.1016/0022-3115(89)90457-1.

- [126] R L Klueh, J M Vitek, and M L Grossbeck. “Effect of low-temperature irradiation with (n,α) Helium production on tensile properties of 12-Cr-1MoVW-type steels”. In: *Journal of Nuclear Materials* 103 & 104 (1981), pp. 887–892. DOI: [https://doi.org/10.1016/0022-3115\(82\)90712-7](https://doi.org/10.1016/0022-3115(82)90712-7).
- [127] Steven Jepeal, Lance Snead, and Zachary Hartwig. “Intermediate energy proton irradiation: rapid, high-fidelity materials testing for fusion and fission energy systems”. In: *eprint arXiv:2009.00048 [Preprint]* (2020). URL: <http://arxiv.org/abs/2009.00048>.
- [128] G. S. Was et al. “Emulation of reactor irradiation damage using ion beams”. In: *Scripta Materialia* 88 (2014), pp. 33–36. ISSN: 13596462. DOI: [10.1016/j.scriptamat.2014.06.003](https://doi.org/10.1016/j.scriptamat.2014.06.003). URL: <http://dx.doi.org/10.1016/j.scriptamat.2014.06.003>.
- [129] J. M. Schippers. “Beam-transport systems for particle therapy”. In: *CERN Yellow Reports: School Proceedings* 1.May (2017), pp. 241–252. ISSN: 2519805X. DOI: [10.23730/CYRSP-2017-001.241](https://doi.org/10.23730/CYRSP-2017-001.241).
- [130] Julie Constanzo et al. “Dosimetry and characterization of a 25-MeV proton beam line for preclinical radiobiology research”. In: *Medical Physics* 46.5 (2019), pp. 2356–2362. ISSN: 00942405. DOI: [10.1002/mp.13512](https://doi.org/10.1002/mp.13512).
- [131] Marcelo Roldán et al. “Ion Beam Experiments to Emulate Nuclear Fusion Environment on Structural Materials at CMAM”. In: *Ion Beam Techniques and Applications*. IntechOpen, June 2020. DOI: [10.5772/intechopen.87054](https://doi.org/10.5772/intechopen.87054).
- [132] N. Soppera, M. Bossant, and E. Dupont. “JANIS 4: An Improved Version of the NEA Java-based Nuclear Data Information System”. In: *Nuclear Data Sheets* 120 (June 2014), pp. 294–296. ISSN: 00903752. DOI: [10.1016/j.nds.2014.07.071](https://doi.org/10.1016/j.nds.2014.07.071).